A High-Resolution Polarizing Microscope for Cryogenic Imaging: Development and Application to Investigations on Twin Walls in $SrTiO_3$ and the Metal-Insulator Transition in V_2O_3

Dissertation
der Mathematisch-Naturwissenschaftlichen Fakultät
der Eberhard Karls Universität Tübingen
zur Erlangung des Grades eines
Doktors der Naturwissenschaften
(Dr. rer. nat.)

vorgelegt von
Matthias Michael Lange
aus Tübingen

Tübingen
2018

Gedruckt mit Genehmigung der Mathematisch-Naturwissenschaftlichen Fakultät der Eberhard Karls Universität Tübingen.

Tag der mündlichen Qualifikation:	20.07.2018
Dekan:	Prof. Dr. Wolfgang Rosenstiel
1. Berichterstatter:	Prof. Dr. Dieter Kölle
2. Berichterstatter:	Prof. Dr. Reinhold Kleiner
3. Berichterstatter:	Prof. Dr. Alejandro Silhanek

Abstract

The present work comprises the development and testing of a combined scanning laser- and widefield polarizing microscope and its application to research on the properties of two material systems that have received extensive attention over the past years: the two-dimensional electron-gas at the $LaAlO_3/SrTiO_3$ interface and the metal-insulator transition in the correlated oxide V_2O_3.

The microscope combines two imaging modes: a scanning polarizing microscope achieving a spatial resolution of $\sim 240\,\mathrm{nm}$ and a sensitivity for the orientation of the polarization of $5.0 \times 10^{-6}\,\mathrm{rad}/\sqrt{\mathrm{Hz}}$, and a widefield polarizing microscope providing a resolution of $\sim 480\,\mathrm{nm}$ and a sensitivity for the orientation of the polarization of $1.0 \times 10^{-4}\,\mathrm{rad}/\sqrt{\mathrm{Hz}}$. To enable low-temperature imaging, the sample is mounted on a ^{4}He continuous flow cryostat providing a temperature range between 4 K and 300 K. Electromagnets are used to apply magnetic fields with variable orientation and a maximum strength of up to 800 mT.

The scanning laser microscope offers an additional imaging mechanism. By locally perturbing the sample using the focused laser beam, and detecting the beam-induced voltage change across a current-biased sample, information on the local electric transport properties can be extracted. The instruments polarization-sensitive detectors enable the imaging of a wide variety of effects that affect the polarization of light, as for example magneto-optical effects and birefringence. Altogether, this makes the microscope a versatile tool that offers the possibility to image magnetic, structural, and electric features of a sample.

The microscope is applied to investigations on twin walls between ferroelastic domains in tetragonal $SrTiO_3$ and their effect on the transport properties of the two-dimensional electron gas at the interface between

$LaAlO_3$ and $SrTiO_3$. The influence of twin walls on the electric transport at the $LaAlO_3/SrTiO_3$ interface has been studied using low-temperature scanning electron microscopy, low-temperature scanning laser microscopy, and the widefield polarizing microscope. The findings of this study confirm the presence of twin walls at angles with respect to the crystallographic axes of the $SrTiO_3$ substrates that match the predictions obtained from the tiling rules of tetragonal domains. It is further shown that electric order within the twin walls can be induced by applying an electric field that exceeds a threshold field of $\sim 1.5\,\mathrm{kV/cm}$.

Furthermore, the low-temperature widefield polarizing microscope was applied to study the metal-insulator transition in V_2O_3. Within this study it was possible to confirm the presence of a phase separation into metallic and insulating domains at the metal-insulator transition. In addition the microscope was used to study the electrical breakdown of the insulating phase of V_2O_3. It was found that the breakdown occurs through the formation of metallic filaments and domains. Complementary numerical simulations confirmed that the metallic filaments are formed by self-reinforced current focusing due to Joule heating and the negative temperature coefficient of the resistivity.

Kurzfassung

Die vorliegende Arbeit behandelt die Entwicklung und Inbetriebnahme eines kombinierten Rasterlaser-Polarisations- und Weitfeld-Polarisationsmikroskops, sowie dessen Anwendung zur Untersuchung der Eigenschaften zweier Materialsysteme die im Zentrum aktueller Forschung stehen: das zweidimensionale Elektronengas an der Grenzfläche zwischen $LaAlO_3$ und $SrTiO_3$ und der Metall-Isolator Übergang in V_2O_3.

Das Mikroskop vereinigt zwei Abbildungsverfahren: ein Rasterlaser-Polarisationsmikroskop das eine räumliche Auflösung von $\sim 240\,\mathrm{nm}$, sowie eine Empfindlichkeit für die Ausrichtung der Polarisation von $5.0 \times 10^{-6}\,\mathrm{rad}/\sqrt{\mathrm{Hz}}$ erreicht und ein Weitfeld-Polarisationsmikroskop mit einer räumlichen Auflösung von $\sim 480\,\mathrm{nm}$ und einer Polarisationsempfindlichkeit von $1.0 \times 10^{-4}\,\mathrm{rad}/\sqrt{\mathrm{Hz}}$. Um Abbildungen bei tiefen Temperaturen zu ermöglichen befindet sich die Probe in einem ^{4}He-Durchfluss-Kryostaten, der es erlaubt die Probentemperatur zwischen $4\,\mathrm{K}$ und $300\,\mathrm{K}$ zu variieren. Mithilfe von Elektromagneten können Magnetfelder mit wählbarer Richtung und einer Feldstärke von bis zu $800\,\mathrm{mT}$ an der Probe angelegt werden.

Das Rasterlaser-Mikroskop bietet einen weiteren Abbildungsmechanismus. Durch lokale Beeinflussung der Probe mit dem fokussierten Laserstrahl ist es möglich, Informationen über die lokalen elektrischen Transporteigenschaften zu gewinnen, indem man die strahlinduzierte Spannungsänderung über einer, mit einem konstanten Strom beaufschlagten, Probe misst. Die polarisationsempfindlichen Detektoren des Mikroskops bieten die Möglichkeit eine breite Palette an Effekten, welche die Polarisation beeinflussen, abzubilden. Beispiele hierfür sind magnetooptische Effekte und Doppelbrechung. Insgesamt macht dies das Mikroskop zu einem vielseitigen Werkzeug, das die Abbildung von magnetischen, strukturellen und elektrischen Eigenschaften einer Probe ermöglicht.

Das Mikroskop wurde zur Untersuchung von Domänenwänden zwischen ferroelastischen Domänen in der tetragonalen Phase von $SrTiO_3$ und deren Einfluss auf die elektrischen Transporteigenschaften des zweidimensionalen Elektronengases an der Grenzfläche zwischen $LaAlO_3$ und $SrTiO_3$ eingesetzt. Die Untersuchung der Beeinflussung des elektrischen Transports an der $LaAlO_3/SrTiO_3$-Grenzfläche erfolgte mittels Tieftemperatur-Rasterelektronenmikroskopie, Tieftemperatur-Rasterlasermikroskopie und dem Weitfeld-Polarisationsmikroskop. Die Ergebnisse dieser Studie bestätigten das Auftreten von Domänenwänden unter Winkeln bezüglich der kristallographischen Achsen des $SrTiO_3$-Substrates, die mit den Voraussagen für tetragonale Domänen übereinstimmen. Des Weiteren wurde gezeigt, dass durch Anlegen eines elektrischen Feldes, welches einen Schwellwert von $\sim 1,5\,\mathrm{kV/cm}$ übersteigt, elektrische Ordnung innerhalb der Domänenwände erzeugt werden kann.

Darüber hinaus wurde das Tieftemperatur-Weitfeld-Polarisationsmikroskop eingesetzt, um den Metall-Isolator-Übergang in V_2O_3 zu untersuchen. Diese Studie bestätigte das Auftreten einer Phasentrennung in metallische und isolierende Domänen am Metall-Isolator-Übergang. Zudem wurde der elektrische Durchbruch in der isolierenden Phase von V_2O_3 mit dem Mikroskop untersucht. Es zeigte sich, dass der Durchbruch durch Bildung elektrisch leitender Filamente und Domänen auftritt. Ergänzende numerische Simulationen zeigten, dass sich die metallischen Filamente durch selbstverstärkte Strombündelung, aufgrund von Jouleschem Heizen und dem negativen Temperaturkoeffizienten des spezifischen Widerstands, bilden.

Contents

1 | Preface

As silicon-based electronics is approaching its physical limits, the exploration of alternative approaches towards data processing incorporating additional functionalities is of broad and current interest in the condensed-matter physics community. Functional oxides, exhibiting effects like ferromagnetism, ferroelasticity, ferroelectricity, multiferroicity, superconductivity, and metal-insulator transitions, are promising candidates in this regard, as domains of the respective order parameters could be used to store and retrieve data. The coupling of multiple order parameters could enable devices, like ultra-fast transistors and non-volatile memories that go beyond binary logic.

Knowledge about the spatial variation of correlations and emergent real-space patterns such as domains plays a key role in acquiring a fundamental understanding of the properties and functional characteristics of these materials, which underlines the importance of techniques that give access to the materials configuration at the micro- or nanoscale. Of particular interest is the response of these materials to external stimuli, as for example changes in magnetic field, electric field, temperature, or current through a device, revealing the functional characteristics that could be employed to implement novel devices.

Dedicated imaging techniques achieving excellent spatial resolution, as for example scanning SQUID microscopy, scanning single electron transistor microscopy, or piezoresponse force microscopy, have been developed that exhibit magnificent sensitivity to magnetic flux, electric charge, and ferroelectric order, respectively. Although operating at a lower spatial resolution, optical microscopy is of special significance in this context, as all of the above mentioned effects influence light-matter interaction. Consequently, optical microscopy is a versatile tool that is sensitive to a wide variety of effects. It is relatively non-invasive and immune to strong magnetic and

electric fields. Operating in the far field regime enables a good thermal decoupling of microscope and sample and offers the possibility to image a sample over a wide temperature range with sub-μm resolution.

The present work comprises the development of a high-resolution combined scanning laser- and widefield polarizing microscope that allows imaging of ferromagnetic, ferroelastic and ferroelectric domains, electric transport properties, and the sample's optical reflectivity. It offers the possibility to investigate samples in a temperature range from 4 K to 300 K and in magnetic fields up to 800 mT. Electrical connections allow for the application of electric current or voltage to the sample in order to perform electric transport measurements in-situ with optical imaging. The microscope is applied to investigations on two material systems that are in the focus of recent research: The first is twin walls between ferroelastic domains that form in the tetragonal phase of $SrTiO_3$ and their influence on the two-dimensional electron gas at the interface between the insulators $LaAlO_3$ and $SrTiO_3$. The second is the phase separation at the metal-insulator transition and the electrically driven insulator-metal transition in the correlated oxide V_2O_3.

This thesis is divided into six chapters. The second chapter gives a brief introduction to light-matter interaction with a focus on polarized light optics and discusses birefringence/bireflectance, magneto-optical effects, and the representation of polarization optics within the Jones calculus.

The third chapter describes the design of the polarizing microscope, discusses its performance and gives two examples demonstrating magneto-optical imaging of magnetic domains in barium hexaferrite and imaging of magnetic flux structures in a superconducting niobium film using a magneto-optical indicator film.

Imaging of twin walls between ferroelastic domains in $SrTiO_3$ by low-temperature scanning electron microscopy and polarized light microscopy is addressed in chapter 4. Due to their polarity, twin walls influence the two-dimensional electron gas at the interface of $LaAlO_3$ and $SrTiO_3$. By application of an electric field beyond a threshold of 1.5 kV/cm, twin walls can be created and an electric order of the dipole moments within a twin wall can be induced.

Chapter 5 examines the metal-insulator transition in V_2O_3. Optical imaging of the phase separation at the metal-insulator transition and the electrically driven insulator-metal transition is demonstrated. A comprehensive study of the breakdown of the insulating phase under the application

of electric current is given. Complementary numerical simulations confirm that the breakdown of the insulating phase is driven by Joule heating.

The thesis concludes with a summary and outlook that is given in the final chapter.

2 | Basics

This chapter gives a brief introduction to light-matter interaction with a focus on polarized light optics. It begins with a discussion of wave propagation in anisotropic media (Sec. 2.1) and the reflection and refraction at interfaces (Sec. 2.2). Following this, optical effects that influence the polarization of light in transmission and reflection are addressed: birefringence and bireflectance in Sec. 2.3, the magneto-optical Kerr effect and the Faraday effect in Sec. 2.4. Polarization optics and their description within the Jones calculus are presented in Sec. 2.5.

2.1 Optics of anisotropic media

2.1.1 The dielectric tensor

In isotropic media the displacement vector $\boldsymbol{D}$ is related to the electric field $\boldsymbol{E}$ by

$$\boldsymbol{D} = \epsilon_\mathrm{r}\epsilon_0\boldsymbol{E} \tag{2.1}$$

with the frequency dependent dielectric constant ϵ_r that describes the response of the material to electric fields, and the vacuum permittivity ϵ_0. Note that, for isotropic media, $\boldsymbol{D}$ and $\boldsymbol{E}$ are parallel. This is not necessarily the case in anisotropic media. Here, the relation of $\boldsymbol{D}$ and $\boldsymbol{E}$ is expressed by the dielectric tensor $\overline{\overline{\boldsymbol{\epsilon}}}_\mathbf{r}$, and is given by

$$\boldsymbol{D} = \epsilon_0\overline{\overline{\boldsymbol{\epsilon}}}_\mathbf{r}\boldsymbol{E} = \epsilon_0 \begin{pmatrix} \epsilon_{xx} & \epsilon_{xy} & \epsilon_{xz} \\ \epsilon_{yx} & \epsilon_{yy} & \epsilon_{yz} \\ \epsilon_{zx} & \epsilon_{zy} & \epsilon_{zz} \end{pmatrix} \boldsymbol{E} \ . \tag{2.2}$$

The dielectric tensor can be diagonalized by choosing an appropriate basis, the principal axes of the medium, and Eq. (2.2) can be written as

$$\boldsymbol{D} = \epsilon_0 \begin{pmatrix} \epsilon_x & 0 & 0 \\ 0 & \epsilon_y & 0 \\ 0 & 0 & \epsilon_z \end{pmatrix} \boldsymbol{E} \tag{2.3}$$

with the so-called principal dielectric constants ϵ_x, ϵ_y, and ϵ_z.

2.1.2 Wave propagation in anisotropic media

A plane wave propagating through an anisotropic medium can be described by

$$\boldsymbol{D} = \boldsymbol{D_0} \mathrm{e}^{\mathrm{i}(\omega t - \boldsymbol{k}\cdot\boldsymbol{r})} \tag{2.4}$$

with wave vector $\boldsymbol{k}$, phase velocity for a given wave vector direction in the medium $c = \omega/|\boldsymbol{k}|$ and a polarization that is defined by the vector $\boldsymbol{D_0}$. Classical electrodynamics is described by the Maxwell equations

$$\nabla \cdot \boldsymbol{D} = \rho \tag{2.5}$$
$$\nabla \cdot \boldsymbol{B} = 0 \tag{2.6}$$
$$\nabla \times \boldsymbol{E} = -\partial_t \boldsymbol{B} \tag{2.7}$$
$$\nabla \times \boldsymbol{H} = \boldsymbol{j} + \partial_t \boldsymbol{D} \ , \tag{2.8}$$

with the magnetic flux density $\boldsymbol{B}$, the magnetic field intensity $\boldsymbol{H}$, charge density ρ, current density $\boldsymbol{j}$ and the partial derivative with respect to time ∂_t. Evaluating the curl of Eq. (2.7), and inserting Eq. (2.8), under the assumption that free charges ($\rho = 0$) and currents ($\boldsymbol{j} = 0$) are absent, gives

$$\nabla \times (\nabla \times \boldsymbol{E}) = -\partial_t (\nabla \times \mu_0 \boldsymbol{H}) = -\mu_0 \partial_t^2 \boldsymbol{D} = -\mu_0 \partial_t^2 \left(\epsilon_0 \overline{\overline{\boldsymbol{\epsilon}}}_{\mathbf{r}} \boldsymbol{E}\right) \ , \tag{2.9}$$

which can be rewritten using the vector identity $\nabla \times (\nabla \times \boldsymbol{E}) = \nabla (\nabla \cdot \boldsymbol{E}) - \nabla^2 \boldsymbol{E}$ to

$$\nabla^2 \boldsymbol{E} - \nabla (\nabla \cdot \boldsymbol{E}) = \mu_0 \epsilon_0 \overline{\overline{\boldsymbol{\epsilon}}}_{\mathbf{r}} \partial_t^2 \boldsymbol{E} \ . \tag{2.10}$$

In the principal basis, the dielectric tensor is diagonal and it is possible to write the three components of this equation for $m \in \{x, y, z\}$ as

$$\partial_x^2 E_m + \partial_y^2 E_m + \partial_z^2 E_m - \partial_m (\partial_x E_x + \partial_y E_y + \partial_z E_z) = \epsilon_0 \mu_0 \epsilon_m \partial_t^2 E_m \ , \tag{2.11}$$

while the components of the plane wave (Eq. (2.4)) are given by

$$D_m = D_{0m} \mathrm{e}^{\mathrm{i}(\omega t - (k_x x + k_y y + k_z z))} \tag{2.12}$$

with the three components of the wave vector k_x, k_y, and k_z. Inserting this into Eq. (2.11) delivers

$$\frac{D_m}{\epsilon_m}\left(k_x^2 + k_y^2 + k_z^2\right) - k_m \left(\frac{k_x D_x}{\epsilon_x} + \frac{k_y D_y}{\epsilon_y} + \frac{k_z D_z}{\epsilon_z}\right) = \epsilon_0 \mu_0 \omega^2 D_m \ . \tag{2.13}$$

This can be further simplified using the relations $\epsilon_0 \mu_0 = 1/\mathrm{c}_0^2$ and $(k_x^2 + k_y^2 + k_z^2) = |\boldsymbol{k}|^2$, where c_0 is the vacuum speed of light, and the principal phase velocities $c_m = \mathrm{c}_0/\epsilon_m^{1/2}$ of the medium:

$$D_m = -\frac{k_m \epsilon_0 {\mathrm{c}_0}^2}{|\boldsymbol{k}|^2 \left(c^2 - c_m^2\right)} \left(k_x E_x + k_y E_y + k_z E_z\right) \tag{2.14}$$

$$:= A \, \frac{k_m}{c^2 - c_m^2} \ . \tag{2.15}$$

Because $\nabla \cdot \boldsymbol{D} = -\mathrm{i}(k_x D_x + k_y D_y + k_z D_z) = 0$, this can be written as

$$\frac{k_x^2}{c^2 - c_x^2} + \frac{k_y^2}{c^2 - c_y^2} + \frac{k_z^2}{c^2 - c_z^2} = 0 \ . \tag{2.16}$$

With the principal refractive indices $n_m = \epsilon_m^{1/2}$ and the refractive index $n = \mathrm{c}_0/c$ along a given direction of the medium, this becomes

$$\frac{k_x^2 n_x^2}{n_x^2 - n^2} + \frac{k_y^2 n_y^2}{n_y^2 - n^2} + \frac{k_z^2 n_z^2}{n_z^2 - n^2} = 0 \ . \tag{2.17}$$

Equation (2.17) is known as Fresnel's equation and is quadratic in n. Generally, solving this equation for the refractive index n of a plane wave propagating along $\boldsymbol{k}$ yields two solutions n_1, n_2. These two solutions correspond to two polarizations $\boldsymbol{D_{01}}$ and $\boldsymbol{D_{02}}$ of the wave with phase velocities

c_1 and c_2. These two polarizations are orthogonal, as can be verified by calculating

$$\boldsymbol{D_{01}} \cdot \boldsymbol{D_{02}} \overset{(2.14)}{=} \sum_{m=x,y,z} D_{m1} D_{m2} \tag{2.18}$$

$$= A_1 A_2 \sum_{m=x,y,z} \frac{k_m^2}{\left(c_1^2 - c_m^2\right)\left(c_2^2 - c_m^2\right)} \tag{2.19}$$

$$= \frac{A_1 A_2}{c_2^2 - c_1^2} \sum_{m=x,y,z} \frac{k_m^2}{c_1^2 - c_m^2} - \frac{k_m^2}{c_2^2 - c_m^2} \overset{(2.16)}{=} 0 \ . \tag{2.20}$$

An effect that is known as birefringence. The two solutions n_1 and n_2 become equal for certain directions of the wave vector. These directions are called the optic axes. Here, a distinction is made between the optic axis denoting the crystal direction in which no birefringence is observed and the optical axis denoting the propagation direction of light through an optical system.

2.2 Reflection and refraction on interfaces

The amplitudes of a plane electromagnetic wave, that is partially reflected and partially refracted at an interface between two optical media, underly boundary conditions that can be obtained from Maxwell's equations. These boundary conditions are given by

$$\boldsymbol{n_{12}} \cdot \left(\boldsymbol{D_2} - \boldsymbol{D_1}\right) = \rho \tag{2.21a}$$

$$\boldsymbol{n_{12}} \times \left(\boldsymbol{E_2} - \boldsymbol{E_1}\right) = 0 \tag{2.21b}$$

$$\boldsymbol{n_{12}} \cdot \left(\boldsymbol{B_2} - \boldsymbol{B_1}\right) = 0 \tag{2.21c}$$

$$\boldsymbol{n_{12}} \times \left(\boldsymbol{H_2} - \boldsymbol{H_1}\right) = \boldsymbol{j} \ , \tag{2.21d}$$

where the subscripts indicate medium 1 and 2 and $\boldsymbol{n_{12}}$ is the surface normal of the interface. Under the assumption, that is reasonable for dielectrics, that free surface charges ($\rho = 0$) and surface currents ($\boldsymbol{j} = 0$) are absent, Eq. (2.21a) and (2.21c) describe the conservation of the components $D_\perp$ and $B_\perp$ that are perpendicular to the interface and Eq. (2.21b) and (2.21d) describe the conservation of the components $E_\parallel$ and $H_\parallel$ that are parallel to

the interface. In the case of isotropic media, where $\boldsymbol{D}$ and $\boldsymbol{E}$ are parallel, the boundary conditions reduce to

$$\epsilon_1 E_{1\perp} = \epsilon_2 E_{2\perp} \tag{2.22a}$$
$$E_{1\parallel} = E_{2\parallel} \tag{2.22b}$$
$$B_{1\perp} = B_{2\perp} \tag{2.22c}$$
$$\frac{B_{1\parallel}}{\mu_1} = \frac{B_{2\parallel}}{\mu_2} \ . \tag{2.22d}$$

Note, that at optical frequencies, the magnetic permeability is $\mu = 1$ for most materials.

The reflection and transmission coefficients can be found using these boundary conditions, the law of reflection $\theta_\mathrm{i} = \theta_\mathrm{r}$ and Snell's law of refraction $n_\mathrm{i}\sin\theta_\mathrm{i} = n_\mathrm{t}\sin\theta_\mathrm{t}$. However, they depend on the polarization of the incident light. Considering three plane electromagnetic waves, that represent the incident (i), reflected (r) and transmitted (t) wave and which are described by

$$\boldsymbol{E}_m = \boldsymbol{E}_{0m}\mathrm{e}^{\mathrm{i}\boldsymbol{k}_m\cdot\boldsymbol{x}-\mathrm{i}\omega t}, \quad \boldsymbol{B}_m = n_m\frac{\boldsymbol{k}_m\times\boldsymbol{E}_m}{|\boldsymbol{k}_m|} \quad m\in\{\mathrm{i},\mathrm{r},\mathrm{t}\} \ , \tag{2.23}$$

a distinction is made between light that is polarized perpendicular to the plane of incidence (s-polarized) and light that is polarized parallel to the plane of incidence (p-polarized). In the following only the amplitudes of the waves are considered. For s-polarized light $\boldsymbol{E}$ is perpendicular to the plane of incidence and thus the component parallel to the interface is given by $E_{m\parallel} = |\boldsymbol{E}_{0m}| = E_{0m}$, while the component of $\boldsymbol{B}$ that is parallel to the interface is given by $B_{m\parallel} = |\boldsymbol{B}_{0m}|\cos\theta_m = n_m E_{0m}\cos\theta_m$. Using Eq. (2.22b) and Eq. (2.22b) it is possible to derive the Fresnel coefficients for s-polarized light

$$r_\mathrm{s} := \frac{E_{0\mathrm{r}}}{E_{0\mathrm{i}}} = \frac{n_\mathrm{i}\cos\theta_\mathrm{i} - n_\mathrm{t}\cos\theta_\mathrm{t}}{n_\mathrm{i}\cos\theta_\mathrm{i} + n_\mathrm{t}\cos\theta_\mathrm{t}} \tag{2.24}$$
$$t_\mathrm{s} := \frac{E_{0\mathrm{t}}}{E_{0\mathrm{i}}} = \frac{2n_\mathrm{i}\cos\theta_\mathrm{i}}{n_\mathrm{i}\cos\theta_\mathrm{i} + n_\mathrm{t}\cos\theta_\mathrm{t}} \ . \tag{2.25}$$

Similarly, the Fresnel coefficients for p-polarized light can be derived using Eq. (2.22a), (2.22b), and (2.22d) and the components of the electric field

parallel to the interface $E_{m\parallel} = E_{0m}\cos\theta_m$ and perpendicular to the interface $E_{m\perp} = E_{0m}\sin\theta_m$

$$r_\mathrm{p} := \frac{E_{0\mathrm{r}}}{E_{0\mathrm{i}}} = \frac{n_\mathrm{t}\cos\theta_\mathrm{i} - n_\mathrm{i}\cos\theta_\mathrm{t}}{n_\mathrm{i}\cos\theta_\mathrm{t} + n_\mathrm{t}\cos\theta_\mathrm{i}} \tag{2.26}$$

$$t_\mathrm{p} := \frac{E_{0\mathrm{t}}}{E_{0\mathrm{i}}} = \frac{2n_\mathrm{i}\cos\theta_\mathrm{i}}{n_\mathrm{i}\cos\theta_\mathrm{t} + n_\mathrm{t}\cos\theta_\mathrm{i}} \ . \tag{2.27}$$

Deriving the Fresnel coefficients of reflection and transmission at the interface between an isotropic and an anisotropic medium or two anisotropic media is much more complicated, because $\boldsymbol{D}$ and $\boldsymbol{E}$ are now related by the dielectric tensor and no longer collinear. The Fresnel coefficients depend on the orientation of the polarization relative to the interface and the orientation of the principal axes of the crystal relative to the propagation direction of the light.

2.3 Birefringence and bireflectance

As has been deduced in Sec. 2.1.2, the index of refraction in optically anisotropic media depends on the orientation of the polarization. This is referred to as birefringence. The refractive index as a function of the polarization direction is described by the index ellipsoid

$$\frac{x^2}{n_x^2} + \frac{y^2}{n_y^2} + \frac{z^2}{n_z^2} = 1 \ . \tag{2.28}$$

Birefringent materials are classified as uniaxial, if two of the principal refractive indices are equal, for example $n_x = n_y \neq n_z$. In this case, light that is polarized perpendicular to the z-axis experiences the same refractive index, called the ordinary refractive index n_o, regardless of the orientation of the polarization in the xy-plane. The z-axis is called the optic axis of the material. On the other hand, light that is polarized along the optic axis experiences a different refractive index, called extraordinary refractive index n_e. Light propagating in an arbitrary direction, with arbitrary polarization, can be decomposed into a part that is linearly polarized perpendicular to the optic axis, called the ordinary ray, and a part that has a component along the optic axis, called the extraordinary ray. The difference $\Delta n = n_\mathrm{e} - n_\mathrm{o}$ between the refractive indices quantifies the birefringence. If $\Delta n > 0$, the crystal is classified as positive uniaxial, otherwise it is negative uniaxial.

Refraction at the interface to a birefringence material has to be considered separately for the ordinary and extraordinary ray. While Snell's law applies to the ordinary ray

$$\sin\theta_\mathrm{i} = n_\mathrm{o}\sin\theta_\mathrm{t} \ , \tag{2.29}$$

it has to be modified by a refractive index that depends on the angle θ between the wave vector and the optic axis

$$\sin\theta_\mathrm{i} = n_\mathrm{e}\left(\theta\right)\sin\theta_\mathrm{t} \tag{2.30}$$

for the extraordinary ray. For non-normal incidence this leads to double refraction. Additionally, the ordinary and extraordinary ray have different phase velocities $\mathrm{c}_0/n_\mathrm{o}$ and $\mathrm{c}_0/n_\mathrm{e}\left(\theta\right)$, which leads to a phase change upon transmission through a crystal of thickness d of

$$\Phi_\mathrm{o} = \frac{2\pi n_\mathrm{o} d}{\lambda_0} \tag{2.31}$$

$$\Phi_\mathrm{e} = \frac{2\pi n_\mathrm{e}\left(\theta\right) d}{\lambda_0} \tag{2.32}$$

with the vacuum wavelength λ_0. The phase difference introduced by the crystal, also called retardance, is given by

$$\Delta\Phi = \Phi_\mathrm{e} - \Phi_\mathrm{o} = \frac{2\pi d}{\lambda_0}\left(n_\mathrm{e}\left(\theta\right) - n_\mathrm{o}\right) \ . \tag{2.33}$$

For incident light that is linearly polarized at an angle to the ordinary polarization direction, this leads to a change in its polarization state that depends on the thickness of the medium. It is possible to realize half-wave plates, that can be used to rotate the polarization, and quarter wave plates, that can be used to convert linear to circular polarization, by adjusting the thickness of the medium accordingly.

Crystals that have three unequal principal refractive indices $n_x \neq n_y \neq n_z$ are called biaxial. By convention the principal axes are labeled, so that $n_x < n_y < n_z$. Biaxial crystals posses two optic axes, that lie in the xz-plane with an angle of

$$\pm\alpha = \tan^{-1}\left(\frac{n_x^{-2} - n_y^{-2}}{n_y^{-2} - n_z^{-2}}\right)^{1/2} \tag{2.34}$$

relative to the z-axis. If $\alpha < 45°$ the crystal is classified as positive biaxial, otherwise it is negative biaxial.

In addition to the retardance observed in transmission, the anisotropic refractive index in birefringent materials also leads to a reflectivity that depends on the orientation of the plane of polarization. An effect that is referred to as bireflectance.

Both birefringence and bireflectance can be used to image ferroelastic domains. Additionally, since ferroelasticity is a condition for ferroelectricity, they can also be used to image ferroelectric domains [1].

2.4 Magneto-optical Kerr effect (MOKE) and Faraday effect

Microscopically, magneto-optical effects are caused by exchange interaction and spin-orbit coupling [2–6] in magnetic materials and lead to an alteration of the polarization of light transmitted through or reflected from the material that depends on the magnetization. Examples are the magneto-optical Kerr-effect [7, 8], the Faraday effect [9], the Voigt effect and the Cotton-Mouton effect [10]. These can be classified with regard to their dependence on the magnetization, the geometrical relation between the wave vector and the magnetization, and the nature of the physical effect [11]: The magneto-optical Kerr effect and the Faraday effect are linear in magnetization and sensitive to the magnetization component parallel to the wave vector. They lead to a rotation of the plane of polarization of linearly polarized light which is caused by a phase shift between left-handed and right-handed circularly polarized light. Therefore, these effects are classified as magnetic circular birefringence. In addition, different absorption for left-handed and right-handed circularly polarized light causes the reflected/transmitted light to be elliptically polarized. This is referred to as magnetic circular dichroism. The Kerr effect is observed in reflection and the Faraday effect in transmission. An important property of the linear magneto-optic effects is their non-reciprocity. The Cotton-Mouton effect and the Voigt effect are quadratic in magnetization and sensitive to the magnetization component perpendicular to the wave vector. For light that is linearly polarized at an angle to the magnetization, the components parallel and perpendicular to the magnetization experience both different refractive indices (magnetic

linear birefringence) and different absorption (magnetic linear dichroism), which leads to rotated and elliptically polarized light, respectively.

Magneto-optical effects can be described [12, 13] by the dielectric permittivity tensor $\bar{\bar{\epsilon}}_{\mathbf{mag}}$, which for an isotropic crystal and the components m_x, m_y and m_z of the magnetization vector $\boldsymbol{m} = \boldsymbol{M}/|\boldsymbol{M}|$ is given by

$$\bar{\bar{\epsilon}}_{\mathbf{mag}} = \epsilon \begin{pmatrix} 1 & -iQ_{\mathrm{v}}m_z & iQ_{\mathrm{v}}m_y \\ iQ_{\mathrm{v}}m_z & 1 & -iQ_{\mathrm{v}}m_x \\ -iQ_{\mathrm{v}}m_y & iQ_{\mathrm{v}}m_x & 1 \end{pmatrix} \tag{2.35}$$

$$+ \begin{pmatrix} B_1 m_x^2 & B_2 m_x m_y & B_2 m_x m_z \\ B_2 m_x m_y & B_1 m_y^2 & B_2 m_y m_z \\ B_2 m_x m_z & B_2 m_y m_z & B_1 m_z^2 \end{pmatrix} \tag{2.36}$$

with the Voigt constant Q_{v}, describing the linear magneto-optical Kerr effect and the Faraday effect, and the magneto-optical constants B_1 and B_2 that describe quadratic magneto-optical effects, such as the Voigt or the Cotton-Mouton effect. The observation of domains in magnetic materials relies mainly on two magneto-optical effects: the magneto-optical Kerr effect (MOKE) in reflection and the Faraday effect in transmission. The Voigt effect and the Cotton-Mouton-effect are rarely used for magnetic domain imaging. Neglecting quadratic magneto-optical effects, the dielectric law can be written [14] as

$$\boldsymbol{D} = \epsilon \left(\boldsymbol{E} + iQ_{\mathrm{v}} \boldsymbol{m} \times \boldsymbol{E} \right) \tag{2.37}$$

with the gyration vector $\boldsymbol{g} = Q_{\mathrm{v}}\boldsymbol{m}$.

A distinction between three types of MOKE with regard to the orientation of the magnetization and the plane of incidence is made: polar, longitudinal and transverse MOKE, being sensitive to the out-of-plane magnetization component, the in-plane magnetization component along the plane of incidence and the in-plane magnetization component perpendicular to the plane of incidence, respectively. These three configurations are shown in Fig. 2.1 for p-polarized light incident on a magnetic sample. For linearly polarized light, both the longitudinal and the polar MOKE lead to a rotation of the plane of polarization upon reflection on the sample surface, while the transverse MOKE leads to a modulation of the reflected intensity. In addition to the rotation of the plane of polarization, the longitudinal and polar MOKE also lead to elliptically polarized light caused by a difference in absorption for left- and right-handed circularly polarized light. Furthermore,

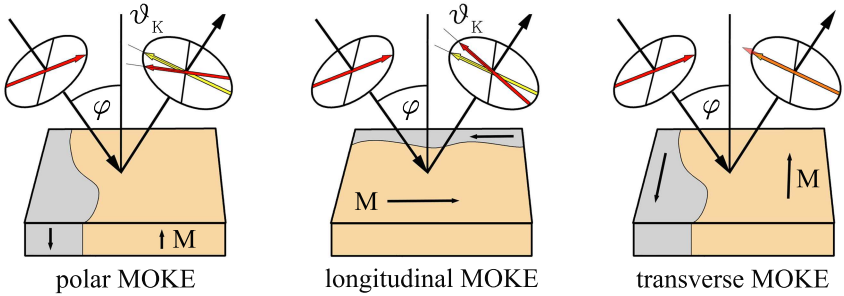

Figure 2.1: The three different configurations for the magneto-optical Kerr effect (adapted after [13]). The polar MOKE is sensitive to the out-of-plane component of the magnetization. The longitudinal MOKE is sensitive to the in-plane component of the magnetization lying in the plane of incidence. Both lead to a rotation of the plane of polarization. The transverse MOKE is sensitive to the magnetization component perpendicular to the plane of incidence and leads to a magnetization-dependent modulation of the reflected intensity.

the MOKE also depends on the angle of incidence (AOI). The polar MOKE is an even function of the AOI and has the largest amplitude for normal incidence. The longitudinal MOKE is an odd function of the AOI and increases with increasing AOI.

The Faraday effect can be observed when light is transmitted through transparent ferromagnetic or paramagnetic materials. It describes a rotation of the plane of polarization by an angle ϑ_F that is proportional to the component of the magnetic field $\boldsymbol{B}$ along the propagation direction $\boldsymbol{k}$ of the light and the length of the path d on which the light interacts with the material

$$\vartheta_\mathrm{F} = V\boldsymbol{B} \cdot \frac{\boldsymbol{k}}{|\boldsymbol{k}|} d \,, \tag{2.38}$$

with the material-specific Verdet constant V that describes the strength of the Faraday-effect in units of rad/(T m).

As an important application, the Faraday effect is exploited in magneto-optical indicator films (MOIF) [15], that can be used to image the magnetic stray field above a sample. These typically consist of thin ferrite-garnet films with in-plane anisotropy that are coated with a mirror on one side. The mirror side of the MOIF is placed in direct contact with the sample

under investigation, which is observed under perpendicular illumination with a polarizing microscope. The stray field of the sample leads to a deflection of the magnetization in the MOIF, that now has a component along the propagation direction of the light and thus becomes observable via the Faraday effect. For additional information on MOIF see Sec. 3.6.2.

2.5 Polarization optics and Jones calculus

2.5.1 Jones calculus

The wave equation of polarized light traveling in z-direction is described by the superposition of two plane waves with amplitude $|E|$ and phase Φ in the xz-plane and yz-plane and is given by

$$\boldsymbol{E}(z,t) = (|E_x|\mathrm{e}^{\mathrm{i}\Phi_x}\hat{\boldsymbol{x}} + |E_y|\mathrm{e}^{\mathrm{i}\Phi_y}\hat{\boldsymbol{y}})\mathrm{e}^{i(kz-\omega t)} \ . \tag{2.39}$$

Polarization optics and their effect on the polarization state of light can be described within the Jones calculus [16–19]. By introducing a global electric field wave E_{eff} and the relative amplitudes A and B of the x-component and y-component of the wave, as well as their phase relation δ

$$E_{\mathrm{eff}}(z,t) := \sqrt{|E_x|^2 + |E_y|^2}\mathrm{e}^{\mathrm{i}\Phi_x}\mathrm{e}^{\mathrm{i}(kz-\omega t)} \tag{2.40}$$

$$A := \frac{|E_x|}{\sqrt{|E_x|^2 + |E_y|^2}} \tag{2.41}$$

$$B := \frac{|E_y|}{\sqrt{|E_x|^2 + |E_y|^2}} \tag{2.42}$$

$$\delta := \Phi_y - \Phi_x \tag{2.43}$$

Eq. (2.39) can be rewritten as

$$\boldsymbol{E}(z,t) = E_{\mathrm{eff}}(z,t)\begin{pmatrix} A \\ B\mathrm{e}^{\mathrm{i}\delta} \end{pmatrix} \tag{2.44}$$

consisting of two parts: the effective wave E_{eff}, describing the amplitude, phase and frequency of the wave and the Jones vector $A\hat{\boldsymbol{x}} + B\mathrm{e}^{\mathrm{i}\delta}\hat{\boldsymbol{y}}$ describing its polarization state.

Generally, $\boldsymbol{E}(z,t)$ represents elliptically polarized light. The polarization ellipse can be characterized by the angle α, relative to the x-axis, at which the major axis occurs

$$\alpha = \frac{1}{2}\tan^{-1}\left(\frac{2AB\cos\delta}{A^2 - B^2}\right). \tag{2.45}$$

and the ellipticity ϵ, which is the ratio of the length of the minor and major axes

$$\epsilon = \frac{\sqrt{A^2\sin^2\alpha + B^2\cos^2\alpha + AB\cos\delta\sin 2\alpha}}{\sqrt{A^2\sin^2\alpha + B^2\cos^2\alpha - AB\cos\delta\sin 2\alpha}}. \tag{2.46}$$

Within the Jones calculus, the polarizing properties of optical components are described by 2 x 2 matrices acting on the Jones vector. The polarizing effects of optical elements usually depend on the orientation of their anisotropy axes relative to the reference coordinate system. At the same time, the polarizing properties of optical elements are easiest to describe in a coordinate system that is based on their anisotropy axes. The corresponding matrix for the reference coordinate system can then be obtained by applying a coordinate transformation to the components coordinate system and back.

For example an ideal linear polarizer that transmits light that is polarized along an axis a and blocks light along the perpendicular axis b can be described in the basis $(\hat{\boldsymbol{a}}, \hat{\boldsymbol{b}})$ by the matrix

$$\boldsymbol{P} = \begin{pmatrix} 1 & 0 \\ 0 & 0 \end{pmatrix}_{(\hat{\boldsymbol{a}},\hat{\boldsymbol{b}})}. \tag{2.47}$$

The corresponding matrix $\boldsymbol{P'}$ in the reference coordinate system, for the polarizer with an orientation of its a-axis at an angle θ to the x-axis, can be determined by applying a rotation $\boldsymbol{R}(\theta)$ to the basis $(\hat{\boldsymbol{a}}, \hat{\boldsymbol{b}})$ and back

$$\boldsymbol{P'} = \boldsymbol{R}(\theta)\boldsymbol{P}\boldsymbol{R}(-\theta) \tag{2.48}$$

$$= \begin{pmatrix} \cos\theta & -\sin\theta \\ \sin\theta & \cos\theta \end{pmatrix} \begin{pmatrix} 1 & 0 \\ 0 & 0 \end{pmatrix}_{(\hat{\boldsymbol{a}},\hat{\boldsymbol{b}})} \begin{pmatrix} \cos\theta & \sin\theta \\ -\sin\theta & \cos\theta \end{pmatrix} \tag{2.49}$$

$$= \begin{pmatrix} \cos^2\theta & \sin\theta\cos\theta \\ \sin\theta\cos\theta & \sin^2\theta \end{pmatrix}_{(\hat{\boldsymbol{x}},\hat{\boldsymbol{y}})}. \tag{2.50}$$

The Jones matrix of an optical system, consisting of several optical components can be obtained by matrix multiplication.

2.5.2 Linear polarizer

A non-ideal linear polarizer is characterized by its transmittance of electrical fields in two orthogonal directions, with transmission coefficients t_a and t_b ($t_a > t_b$) for light polarized along the a or b-axis, respectively. Or, alternatively, a linear polarizer is characterized by the transmission t_a and the extinction ratio $\kappa = t_b^2/t_a^2$, which is the ratio of minimum and maximum transmitted intensity for fully linearly polarized light. The Jones matrix of a real polarizer is given by

$$\boldsymbol{P} = \begin{pmatrix} t_a & 0 \\ 0 & t_b \end{pmatrix}_{(\hat{\boldsymbol{a}},\hat{\boldsymbol{b}})} = t_a \begin{pmatrix} 1 & 0 \\ 0 & \sqrt{\kappa} \end{pmatrix}_{(\hat{\boldsymbol{a}},\hat{\boldsymbol{b}})} . \tag{2.51}$$

A large number of different realizations of linear polarizers exist. The three types used in the setup discussed in chapter 3 are: Glan-Thompson prism, Wollaston prism, and polarizers based on oriented silver nanoparticles. A Glan-Thompson prism, shown in Fig. 2.2 (a), consists of two cemented calcite prisms. Calcite is birefringent with refractive indices n_o for the p-polarized ordinary ray and n_e for the s-polarized extraordinary ray. The refractive index of the cement n_c is chosen, so that $n_\mathrm{e} < n_\mathrm{c} < n_\mathrm{o}$. The cutting angle of the prisms is designed, so that the ordinary ray undergoes total internal reflection while the extraordinary ray is transmitted. Typically, an extinction ratio of $\kappa < 1 \times 10^{-6}$ and a transmission of $t_a > 90\,\%$ over a spectral range of $350 - 2700\,\mathrm{nm}$ can be achieved.

A Wollaston prism, shown in Fig. 2.2 (b), consists of two calcite prisms that are cemented together at their base. Because the optic axes of the two prisms are orthogonal, the s-polarized beam is the ordinary beam in the first prism and becomes the extraordinary beam in the second prism. The p-polarized beam on the other hand is the extraordinary beam in the first prism and becomes the ordinary beam in the second prism. Since the indices of refraction satisfy the condition $n_\mathrm{e} < n_\mathrm{c} < n_\mathrm{o}$, the s-polarized and p-polarized beam are refracted in opposite directions at the interface of the two prisms. A Wollaston prism consequently splits an incoming beam into two beams with orthogonal polarization. Typically, an extinction ratio of $\kappa < 1 \times 10^{-6}$ and a transmission of $t_a > 90\,\%$ over a spectral range of $350 - 2200\,\mathrm{nm}$ can be achieved.

Polarizers based on films of oriented prolate silver nanoparticles [20] are another type of polarizer that achieves high extinction ratios [Fig. 2.2 (c)]. The two plasmon resonance frequencies, for light polarized parallel and

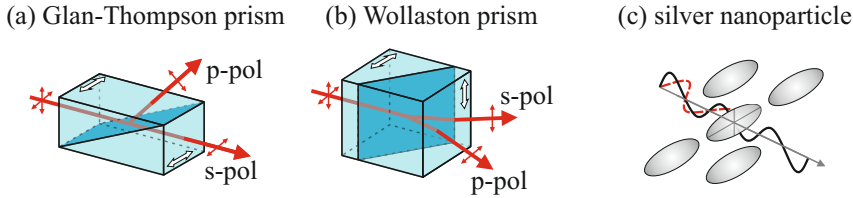

Figure 2.2: Three types of polarizers used for the setup. The white double-headed arrows indicate the optic axis of the respective birefringent crystals. (a) Glan-Thompson prism: total internal reflection of the ordinary ray. (b) Wollaston prism: s- and p-polarized light are refracted in opposite directions. (c) Oriented prolate silver nanoparticle polarizer: the component polarized along the long axis of the nanoparticle is absorbed.

perpendicular to the long axis of the nanoparticles, can be tailored by adjusting the aspect ratio and size of the nanoparticles. By choosing the right shape and size of nanoparticles, it is possible to achieve a high difference in transmission for light polarized perpendicular and parallel to the long axis of the nanoparticles in a certain wavelength range. These polarizers typically achieve extinction ratios of $\kappa < 1 \times 10^{-5}$ and a transmission of up to $t_a = 80\,\%$ over a bandwidth of around 100 nm within the optical regime. Due to the fact that the polarizing element is a thin film, these polarizers can be manufactured with a compact size.

2.5.3 Wave plates/retarder

A wave plate or retarder is an optical component that is constructed from a parallel plate of a birefringent material with the optic axis in the plane of the plate. Due to the difference in refractive index $\Delta n = n_\mathrm{o} - n_\mathrm{e}$, this leads to a relative phase shift between the ordinary and extraordinary beam of

$$\xi = \frac{2\pi \Delta n d}{\lambda_0} \,, \tag{2.52}$$

with the vacuum wavelength λ_0 and the crystal thickness d. The Jones-matrix of a retarder with relative phase shift ξ in a basis of ordinary and extraordinary beam $(\hat{\boldsymbol{a}}, \hat{\boldsymbol{b}})$ is given by

$$\boldsymbol{J}_{\mathbf{WP}}(\xi) = \begin{pmatrix} 1 & 0 \\ 0 & \mathrm{e}^{\mathrm{i}\xi} \end{pmatrix}_{(\hat{\boldsymbol{a}},\hat{\boldsymbol{b}})} . \tag{2.53}$$

The most important types of wave plates are half-wave plates, introducing a phase shift of $\xi = \pi$, and quarter-wave plates, introducing a phase shift of $\xi = \pi/2$. The effect of a wave plate with ordinary axis oriented at an angle θ with respect to the x-axis is given by $\boldsymbol{J}_{\mathbf{WP}}(\xi, \theta) = \boldsymbol{R}(-\theta)\boldsymbol{J}_{\mathbf{WP}}(\xi)\boldsymbol{R}(\theta)$. For a half-wave plate this matrix reduces to

$$\boldsymbol{J}_{\mathbf{WP}}(\pi, \theta) = \begin{pmatrix} \cos 2\theta & \sin 2\theta \\ \sin 2\theta & -\cos 2\theta \end{pmatrix}_{(\hat{\boldsymbol{x}},\hat{\boldsymbol{y}})} . \tag{2.54}$$

The effect of this matrix on linearly polarized light is a rotation of the plane of polarization by twice the angle between the ordinary axis and the initial orientation of the polarization. In the case of a quarter-wave plate, the matrix is given by

$$\boldsymbol{J}_{\mathbf{WP}}(\frac{\pi}{2}, \theta) = \begin{pmatrix} \cos^2\theta + \mathrm{i}\sin^2\theta & \sin\theta\cos\theta - \mathrm{i}\sin\theta\cos\theta \\ \sin\theta\cos\theta - \mathrm{i}\sin\theta\cos\theta & \sin^2\theta + \mathrm{i}\cos^2\theta \end{pmatrix}_{(\hat{\boldsymbol{x}},\hat{\boldsymbol{y}})} . \tag{2.55}$$

Quarter-wave plates can be used to convert linearly polarized light to elliptically polarized or vice versa.

Wave plates cannot be manufactured in thicknesses that provide a relative phase shift of a fraction of a wavelength. So called, multi-order wave plates provide a phase shift $\xi_{\mathrm{mult}} = 2n\pi + \xi_{\mathrm{zero}}$, $n \in \mathbb{N}$, that is a multiple of full wavelength shifts in addition to the desired phase shift ξ_{zero}. Multi-order wave plates are very sensitive to changes in wavelength or temperature. These drawbacks can be overcome by zero-order wave plates, which are manufactured by combining two multi-order wave plates with phase shifts ξ_1 and ξ_2 that differ by the desired phase shift ξ_{zero}. By aligning the ordinary axis of the second wave plate with the extraordinary axis of the first wave plate, the phase shifts of both multi-order wave plates compensate each other and a remaining phase shift $\xi_{\mathrm{zero}} = \xi_1 - \xi_2$ is obtained.

2.5.4 Reflection and transmission

The reflection and transmission of light at an interface is described by the complex-valued Fresnel coefficients, which are defined as the ratios of the reflected electric field E_r and transmitted electric field E_t to the incident electric field E_i for light polarized parallel to the plane of incidence (p-polarization) and perpendicular to the plane of incidence (s-polarization)

$$r_\mathrm{s,p} = \left(\frac{E_\mathrm{r}}{E_\mathrm{i}}\right)_\mathrm{s,p} = |r_\mathrm{s,p}| \cdot \mathrm{e}^{\mathrm{i}\phi} \tag{2.56}$$

$$t_\mathrm{s,p} = \left(\frac{E_\mathrm{t}}{E_\mathrm{i}}\right)_\mathrm{s,p} = |t_\mathrm{s,p}| \cdot \mathrm{e}^{\mathrm{i}\phi} \ . \tag{2.57}$$

The Fresnel coefficients, which depend on the angle of incidence θ, keep track of the amplitude and phase of the reflected and transmitted wave. The corresponding Jones matrices in the basis $(\hat{\boldsymbol{p}}, \hat{\boldsymbol{s}})$ are given by

$$\boldsymbol{J}_\mathbf{R}(\theta) = \begin{pmatrix} r_\mathrm{p} & 0 \\ 0 & r_\mathrm{s} \end{pmatrix}_{(\hat{\boldsymbol{p}},\hat{\boldsymbol{s}})} \tag{2.58}$$

and

$$\boldsymbol{J}_\mathbf{T}(\theta) = \begin{pmatrix} t_\mathrm{p} & 0 \\ 0 & t_\mathrm{s} \end{pmatrix}_{(\hat{\boldsymbol{p}},\hat{\boldsymbol{s}})} \ . \tag{2.59}$$

The polarizing effect of a mirror or transparent surface at an arbitrary angle is determined by the matrices $\boldsymbol{J}_\mathbf{R}$ and $\boldsymbol{J}_\mathbf{T}$ and by a rotation from the reference coordinate system to the $(\hat{\boldsymbol{p}}, \hat{\boldsymbol{s}})$ basis.

2.5.5 Magneto-optical effects

The magneto-optical Kerr effect, the reflection at the interface between a non-magnetic and a magnetic medium, can be described within the Jones calculus by the matrix [21–23]

$$\boldsymbol{J}_\mathbf{MOKE} = \begin{pmatrix} r_\mathrm{pp} & r_\mathrm{ps} \\ r_\mathrm{sp} & r_\mathrm{ss} \end{pmatrix} \tag{2.60}$$

with the off-diagonal components for the polar and longitudinal MOKE

$$\begin{aligned} r_\mathrm{sp}^\mathrm{pol} &= r_\mathrm{ps}^\mathrm{pol} \\ &= \frac{-\mathrm{i}Q_\mathrm{v} m^\mathrm{pol} n_\mathrm{mag} n_\mathrm{i} \cos\theta_\mathrm{i}}{(n_\mathrm{m}\cos\theta_\mathrm{i} + n_\mathrm{i}\cos\theta_\mathrm{m})(n_\mathrm{i}\cos\theta_\mathrm{i} + n_\mathrm{m}\cos\theta_\mathrm{m})} \end{aligned} \tag{2.61}$$

$$
\begin{aligned}
r_{\mathrm{sp}}^{\mathrm{long}} &= -r_{\mathrm{ps}}^{\mathrm{long}} \\
&= \frac{\mathrm{i}Q_{\mathrm{v}} m^{\mathrm{long}} n_{\mathrm{m}} \sin\theta_{\mathrm{m}} n_{\mathrm{i}} \cos\theta_{\mathrm{i}}}{(n_{\mathrm{m}}\cos\theta_{\mathrm{i}} + n_{\mathrm{i}}\cos\theta_{\mathrm{m}})(n_{\mathrm{i}}\cos\theta_{\mathrm{i}} + n_{\mathrm{m}}\cos\theta_{\mathrm{m}})\cos\theta_{\mathrm{m}}} \,,
\end{aligned}
\tag{2.62}
$$

where Q_{v} is the Voigt constant, n_{m} and n_{i} are the refractive indices of the magnetic medium and the medium of incidence, and θ_{i} and θ_{m} is the angle of incidence and the angle of the refracted light in the magnetic medium, respectively. The magnetization components under investigation in the polar configuration m^{pol} and longitudinal configuration m^{long} are given by the projection of $\boldsymbol{m} = \boldsymbol{M}/|\boldsymbol{M}|$ onto the propagation direction $\boldsymbol{k}/|\boldsymbol{k}|$.

The Faraday effect can be described as a retardation that is introduced between right-handed and left-handed circularly polarized light (magnetic circular birefringence). Therefore it has the diagonal Jones matrix

$$
\boldsymbol{J}_{\mathbf{F}}(\vartheta_{\mathrm{F}}) = \begin{pmatrix} e^{\mathrm{i}\vartheta_{\mathrm{F}}} & 0 \\ 0 & e^{-\mathrm{i}\vartheta_{\mathrm{F}}} \end{pmatrix}_{(\hat{\boldsymbol{l}},\hat{\boldsymbol{r}})}
\tag{2.63}
$$

in the basis $(\hat{\boldsymbol{l}}, \hat{\boldsymbol{r}})$ of the circular polarization states. The Faraday rotation angle ϑ_{F} is given according to Eq. (2.38). In the basis of orthogonal linear polarizations $(\hat{\boldsymbol{x}}, \hat{\boldsymbol{y}})$, this becomes

$$
\begin{aligned}
\boldsymbol{J}_{\mathbf{F}}(\vartheta_{\mathrm{F}}) &= \frac{1}{\sqrt{2}} \begin{pmatrix} 1 & \mathrm{i} \\ \mathrm{i} & 1 \end{pmatrix} \begin{pmatrix} \mathrm{e}^{\mathrm{i}\vartheta_{\mathrm{F}}} & 0 \\ 0 & \mathrm{e}^{-\mathrm{i}\vartheta_{\mathrm{F}}} \end{pmatrix}_{(\hat{\boldsymbol{l}},\hat{\boldsymbol{r}})} \frac{1}{\sqrt{2}} \begin{pmatrix} 1 & -\mathrm{i} \\ -\mathrm{i} & 1 \end{pmatrix} \\
&= \begin{pmatrix} \cos\vartheta_{\mathrm{F}} & \sin\vartheta_{\mathrm{F}} \\ -\sin\vartheta_{\mathrm{F}} & \cos\vartheta_{\mathrm{F}} \end{pmatrix}_{(\hat{\boldsymbol{x}},\hat{\boldsymbol{y}})} \,,
\end{aligned}
\tag{2.64}
$$

which shows that the Faraday effect causes a pure rotation of the polarization state in the linear basis.

3 | Design of the Instrument [1]

The properties of ferroic materials and devices are strongly affected by their microscopic domain structure. Knowledge about the domains often plays a key role in the understanding and interpretation of integral measurements, which puts an emphasis on the importance of imaging techniques. Polarized light microscopy is an excellent tool for this purpose and has been successfully applied to ferromagnetic [21], ferroelastic [26] and ferroelectric [27, 28] domain imaging. Alternative methods for imaging of magnetic domains include Bitter decoration [29], Lorentz microscopy [30], electron holography [31], magnetic force microscopy [32], scanning SQUID microscopy [33], scanning Hall probe microscopy [34], nitrogen vacancy center microscopy [35], X-ray magnetic circular dichroism [36], scanning electron microscopy (SEM) [37], and SEM with polarization analysis (SEMPA) [38]. A comparison of most of these methods can be found in Ref. [13]. Imaging of ferroelectric domains has also been accomplished by etching [39], nanoparticle decoration [40], scanning electron microscopy [41], piezoresponse force microscopy [42] and X-ray diffraction [43]. These techniques have been reviewed by Potnis *et al.* [44] and by Soergel [45].

Polarized light imaging provides a non-destructive, non-contact way to observe ferroic domains with sub-μm resolution and high sensitivity that can be carried out in high magnetic fields. The contrast for imaging of fer-

[1] Parts of this chapter have been published in [24]. Own contributions: On the basis of the original design by S. Guénon [25], I remodeled the microscope and designed the mechanical, optical and electronic parts covered in this chapter. F. Lever designed and built the Helmholtz coil generating the out-of-plane magnetic field. I developed the control software, assembled and tested the microscope and wrote the manuscript. I gratefully acknowledge advice by C. Kalkuhl and the electronics workshop and thank the mechanical workshop, especially M. Kleinmann and H. Eißler, for their outstanding work.

roelastic or ferroelectric domains arises from birefringence or bireflectance [1, 46], which is a consequence of the anisotropic permittivity tensor of these materials. Ferromagnetic domains, on the other hand, can be imaged via the magneto-optical Kerr effect [7] (MOKE) or the Faraday effect [9]. Both confocal laser scanning [47] and widefield [48] microscopy can be used for imaging with polarized light contrast. In confocal laser scanning microscopy the image is captured sequentially by scanning a focused laser beam across the sample. A confocal pinhole eliminates light that does not originate from the focal volume. This results in a high depth discrimination, a contrast enhancement, and a 28 % increase in lateral resolution. Widefield microscopy, on the other hand, has the advantage of faster acquisition rates and simultaneous image formation.

The instrument discussed below is based on an earlier design by Guénon [25] and combines a widefield- and a confocal laser scanning microscope with polarization-sensitive detectors. To study effects at low temperatures and in magnetic fields, the sample is mounted on a liquid-helium continuous flow cryostat offering a temperature range from 4 K to 300 K, and magnetic fields up to 800 mT with variable orientation in the substrate plane and 20 mT perpendicular to the substrate plane can be applied. The confocal laser scanning microscope offers an additional imaging mechanism: a beam-induced voltage across a current-biased sample can be generated by the local perturbation of the laser beam. This beam-induced voltage can be used to extract local information on the electric transport properties of the sample [49–53]. While several examples of low-temperature widefield [54–56] and laser scanning polarizing microscopes [57–59] have been published, the instrument presented here stands out with regard to the versatility offered by combining widefield and confocal laser scanning imaging modes, the accessible temperature range, as well as the very high lateral resolution it provides at low temperatures.

This chapter is organized as follows. The cryostat and the generation of magnetic fields is described in Section 3.1. The widefield polarizing microscope is discussed in Section 3.2, and a detailed description of the scanning laser microscope is presented in Section 3.3. Imaging of electric transport properties is addressed in Section 3.4, a brief introduction to digital image processing is given in Sec. 3.5, and examples demonstrating the performance of the instrument are presented in Section 3.6. The system specifications are summarized in Sec. 3.7.

3.1 Cryostat and electromagnets

The cryostat and microscope are mounted on a vibrationally isolated optical table. Since the sample is fixed on a coldfinger, the microscope needs to be positioned relative to the sample with sub-μm resolution. To allow for adjustment of the microscope position relative to the coldfinger, the microscope is connected to the cryostat via flexible bellows. Because of the forces exerted by the vacuum, which pull the microscope in z-direction with a force of approximately 200 N, a very sturdy and precise positioning unit needs to be used. The positioning unit is an improved version of the one designed by Guénon [25]. It allows for translation of the microscope in x, y, and z-direction, as well as the adjustment of pitch and yaw, to position the microscope so that the optical axis is perpendicular to the sample surface.

The liquid-helium continuous flow cryostat is a *Janis Research Company, inc. model ST-200*, with the sample in vacuum that has been modified to adapt the microscope. The modifications include a new vacuum isolation to adapt the microscope and a new infrared (IR) shielding that incorporates a vibration reduction mechanism.

Although the setup has been carefully isolated against external sources of vibrations, the helium evaporating inside the coldfinger can lead to mechanical oscillations that make high resolution imaging impossible. To reduce these vibrations, the coldfinger is stabilized relative to the IR shielding with two PEEK[2] bolts and one spring-loaded bolt, and the IR shielding is fixed in the same way relative to the vacuum isolation, as shown in Fig. 3.1. Vibrations are reduced to well below the resolution limit with this stabilization mechanism. The coldfinger and sample holder have a diameter of 25.4 mm. Electrical contacts and mounting screws around the perimeter of the sample holder limit the available space for sample mounting. Samples with a dimension of up to 12 mm × 12 mm can be conveniently mounted.

The temperature is regulated using a *Lakeshore LS340* temperature controller. The temperature can be adjusted in a range of $T = 4\,\mathrm{K}$ to $T = 300\,\mathrm{K}$, and a temperature stability in the mK range can be achieved. For electric transport measurements, 16 electrical lines are guided to the coldfinger. Because residual gases and water adsorbed to the cryostat walls tend to freeze onto the sample upon cool down, great care has been taken to ensure that all parts inside the cryostat have low outgassing rates and

[2] Polyether ether ketone

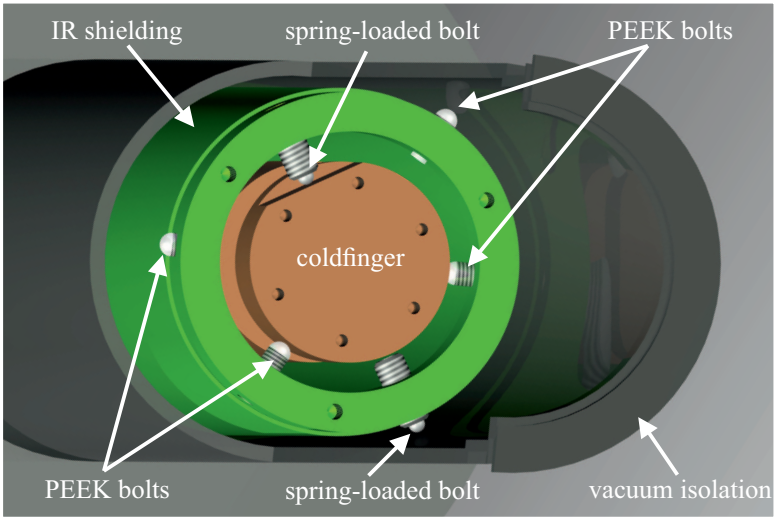

Figure 3.1: Stabilization of the coldfinger (25.4 mm diameter) against vibrations. The vacuum isolation is cut away partially to reveal the mechanism used to stabilize the coldfinger against vibrations caused by the evaporating helium. The coldfinger is stabilized relative to the IR shielding using two PEEK bolts and a spring-loaded bolt. The IR shielding is stabilized relative to the vacuum isolation in the same manner.

smooth surfaces. Where plastics couldn't be avoided, PEEK or Teflon was used and metal parts have been electropolished if possible. Before cool down, the cryostat is evacuated to a pressure of less than 1.5×10^{-6} mbar. During the measurement the vacuum pump needs to be disconnected from the setup to avoid vibrations.

Two electromagnets are used to generate in-plane magnetic fields of up to $B_{\parallel} = \pm 800\,\mathrm{mT}$ and out-of-plane magnetic fields of up to $B_{\perp} = \pm 20\,\mathrm{mT}$. The electromagnets are mounted on a frame that is separated from the rest of the setup to reduce the risk of vibrations being transferred to the microscope. The out-of-plane magnetic field is generated by a custom-made Helmholtz coil that achieves a field homogeneity of 0.2 % in a cylindrical volume of 5 mm length in out-of-plane direction and 20 mm diameter in the sample plane. The Helmholtz coil produces a magnetic field of 1.98 mT/A

and is driven by a power supply delivering a maximum current of 10 A [60]. The electromagnet for the in-plane magnetic field is a water-cooled *GMW model 5403*, that can be rotated around the cryostat to allow for an adjustment of the orientation of the in-plane magnetic field. It is driven by a unipolar *Sorensen DLM 40-75E* power supply, which is capable of delivering a current of up to 75 A. A current reversal switch has been designed to add the possibility of bipolar magnetic field sweeps. The in-plane magnetic field is homogeneous to within 1 % in a cubic volume with an edge length of 12 mm. The magnetic fields for both magnets have been calibrated using a Hall probe with an accuracy of 2 %. Due to spatial constraints limiting the size of the Helmholtz coil, the achievable out-of-plane magnetic field strength is limited to 20 mT. The range of applications of the instrument could be enhanced by replacing the two electromagnets by a superconducting vector magnet that allows the application of magnetic fields with a strength > 1 T and variable orientation.

3.2 Low-temperature widefield polarizing microscope (LTWPM)

The optical setup combines two imaging paths, a scanning polarizing microscope and a widefield polarizing microscope; the latter can be selected by inserting a mirror into the optical path. A schematic drawing of the imaging setup is displayed in Fig. 3.2. Conjugate planes to the image plane are denoted as image planes (IP) and shown in orange. Conjugate planes to the back focal plane (BFP) of the microscope objective are denoted as aperture planes (AP) and shown in green. AP and IP have a reciprocal relationship [48]: rays that are parallel in one set of planes are focused in the other set of planes. The position of a point in the IP translates to an angle in the AP and the angle of a ray in the IP corresponds to a point in the AP.

This section starts with a general description of the optical setup of the low-temperature widefield polarizing microscope (LTWPM) before proceeding to a detailed description of the components and their function. The LTWPM can be used by inserting the removable mirror, as indicated by the broken lines in the ray diagram (Fig. 3.2). The illumination follows a Koehler scheme [61] and the sample is illuminated through the microscope objective. The light source for the LTWPM is realized by fiber-coupled

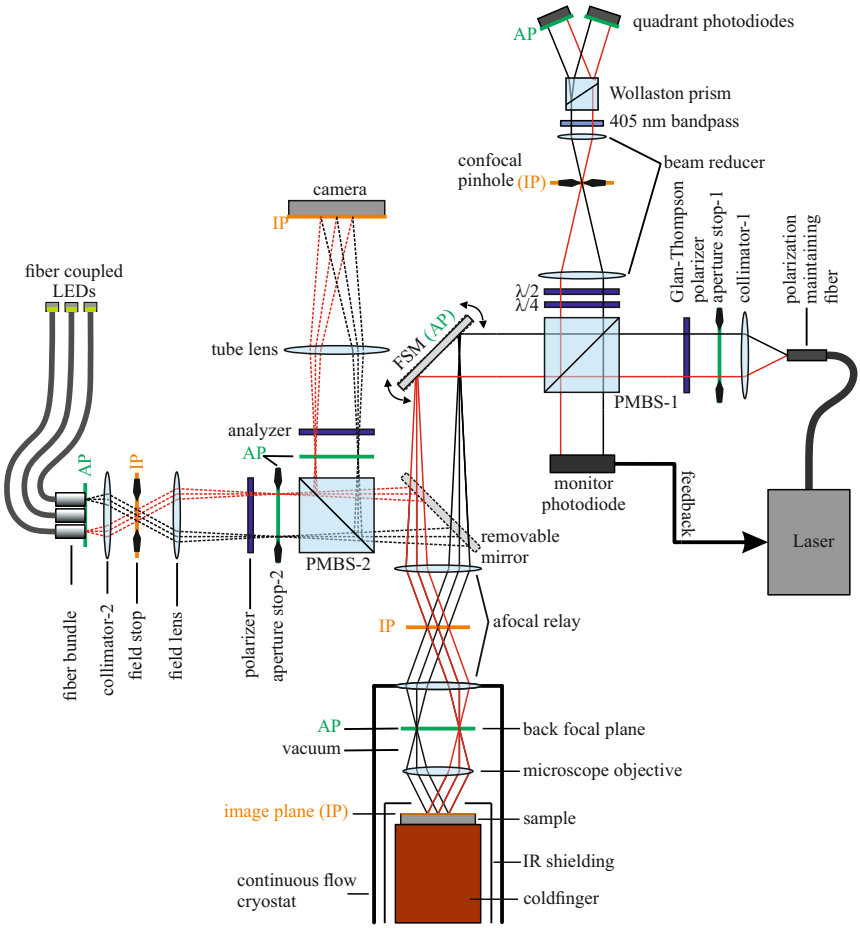

Figure 3.2: Schematic overview of the optical setup. Conjugate image planes (IP) are displayed in orange, conjugate aperture planes (AP) in green. The setup combines two imaging paths that can be selected via the removable mirror: a widefield polarizing microscope (mirror inserted), in which the sample is imaged onto the sensor of the camera, and a scanning polarizing microscope (mirror removed), that uses a fast-steering mirror (FSM) to scan a laser beam across the sample. From [24].

light-emitting diodes (LED), that are combined into a fiber bundle. The fiber bundle end face is imaged into the back focal plane of the microscope objective. To achieve this, the fiber output is collimated (collimator-2) and the field lens is used to image the fiber ends into an AP at the position of an interchangeable aperture stop (aperture stop-2). A rotatable polarizer in front of the aperture stop is used to define the plane of polarization. A field stop, aligned with the shared focal plane of collimator-2 and the field lens, can be used to confine the illuminated sample area. After passing a polarization maintaining beam splitter (PMBS-2), the light is reflected by the removable mirror onto the part of the setup that is shared with the scanning polarizing microscope. The light passes an afocal relay, which is used to extend the optical path into the cryostat and to image the light source into the BFP of the microscope objective. The afocal relay is discussed in detail in Sec. 3.3.3. After passing the afocal relay, the light is focused onto the sample by the microscope objective. The light is reflected back from the sample, passes the microscope objective, afocal relay and removable mirror and is deflected by the PMBS-2. Subsequently, it passes the rotatable analyzer, that is used to adjust the polarized light contrast. The tube lens forms the image on the sensor of the low noise, high dynamic range sCMOS camera.

3.2.1 Light source

The light source consists of nine high-power LEDs with a dominant wavelength of 528 nm that are coupled into multimode fibers. The LEDs are temperature stabilized by thermo-electric coolers and driven with highly stable current sources. The use of LEDs offers the advantage of low noise, compact size and excellent stability. The nine fibers are combined into a fiber bundle consisting of one central fiber of 1 mm diameter and eight surrounding fibers of 0.8 mm diameter as shown in Fig. 3.3. A similar illumination concept has been developed by Soldatov *et al.* [62, 63]. Since the LEDs can be controlled individually and the fiber ends are imaged into the back focal plane of the microscope objective, it is possible to switch between different angles of incidence. In magneto-optical imaging, the plane of incidence together with the plane of polarization, is used to adjust the sensitivity of the instrument to the polar, longitudinal or transverse MOKE [21, 64]. As was demonstrated by Soldatov *et al.*, this illumination

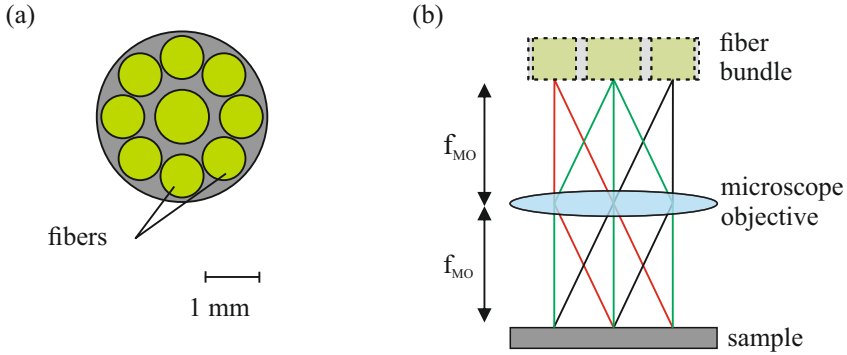

Figure 3.3: Illumination concept for the widefield microscope. (a) Cross section of the fiber bundle: The central fiber is aligned with the optical axis. The eight surrounding fibers are equally distributed on a concentric circle. (b) The fiber end faces are imaged into the microscope objective back focal plane. The light originating from each fiber reaches the sample at a specific angle. The angle of incidence for the illumination can be selected by controlling the LEDs output power individually. From [24].

concept can be used to separate longitudinal and polar MOKE and to achieve a contrast enhancement.

The LEDs can be pulsed with a frequency of more than 1 MHz, which can be used to image repeatable processes with μs temporal resolution. This is done by a stroboscopic technique. A periodic excitation, for example a current through a patterned microstructure or an alternating magnetic field, is used to trigger the repeatable process and short light pulses that are synchronized with the excitation signal are used to image the sample. By varying the delay between the begin of the excitation signal and the emission of the light pulse, time-resolved images can be acquired. It is necessary to integrate over many light pulses (typically several hundred to thousands), and hence many cycles of the excitation signal, to achieve a sufficient signal to noise ratio.

The basic design of the LED driver module is shown in Fig. 3.4. Two light-emitting diodes are used on each module. One of these LEDs is coupled into a multimode fiber, while the other only serves as an identical load. Modulation of the LEDs is achieved by switching between LED1 and LED2.

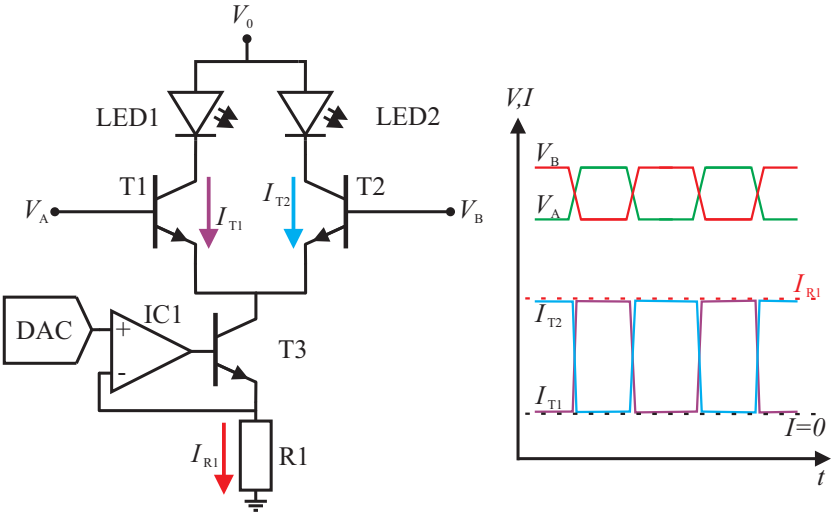

Figure 3.4: Basic design of the LED driver module. A constant current I_{R1} is steered between LED1 and LED2 by applying a differential voltage $V_{diff} = V_A - V_B$ to the bases of T1 and T2.

The design is based on a circuit known in electronics as "long-tailed pair": A constant current sink is realized by the digital to analog converter (DAC), operational amplifier (IC1), transistor (T3), and shunt resistor (R1) with resistance R_1. The operational amplifier controls its output voltage, and with it the base current flowing into T3, so that the voltage $V_1 = R_1 \cdot I_{R1}$ across the shunt resistor R1 is equal to the output voltage of the DAC. This makes a very stable programmable current sink that draws a constant current $I_{R1} = I_{T1} + I_{T2}$ through the transistors T1 and T2, and consequently through LED1 and LED2. By applying a differential voltage $V_{diff} = V_A - V_B$ to the bases of T1 and T2, the current is steered between LED1 and LED2. This circuit has the advantage that only the current flowing through the arms of the long-tailed pair is modulated at high frequencies, while the total current is a pure dc current.

3.2.2 Microscope objective

In order to achieve a high spatial resolution it is necessary to use a microscope objective with a high numerical aperture (NA). Such an objective typically has a short working distance, which does not allow for the use of a vacuum window in front of the objective. Also, a window in front of the objective would introduce unwanted variations to the polarization of the light. Therefore, the microscope objective needs to be mounted inside the cryostat. This imposes the requirement for the microscope objective to be vacuum compatible. At the same time, the possibly large difference in temperature between the microscope objective and the sample prohibits the use of immersion objectives or objectives with excessively short working distances, which limits the choice of high NA objectives.

A *NIKON CFI TU Plan Fluor EPI-P 50×* microscope objective is used. It has an equivalent focal length of $f_{\mathrm{MO}} = 4\,\mathrm{mm}$, a numerical aperture of 0.8, and a working distance of $WD = 1\,\mathrm{mm}$. The microscope objectives back focal plane is situated inside the objective assembly at a distance of 8.5 mm measured from the objective shoulder, and the exit pupil has a diameter of 6.4 mm. It has a field of view (FOV) of 500 μm diameter and features high transmission of about 80 % at 405 nm and 87 % at 528 nm wavelength. The objective is designed for polarized light microscopy with lenses that have been mounted strain free and is suitable for confocal scanning, which is an important requirement because it is also used for the scanning polarizing microscope.

Although the microscope objective is not designed for use in a high-vacuum environment, it works very well in this regard and, in contrast to a previously used objective by another manufacturer, no problems related to outgassing of components inside the objective assembly have been observed.

3.2.3 Camera, polarization sensitivity and resolution

The small variations in polarization, caused for example by magneto-optical effects, only lead to a very weak modulation of the intensity reaching the camera. Therefore, cameras with low noise and high dynamic range are required for imaging in polarized light microscopy. An *Andor Zyla 4.2 PLUS* sCMOS camera is used. The camera sensor with 2048 x 2048 pixels, a pixel size of 6.5 μm x 6.5 μm and a high quantum efficiency of $QE \approx 80\,\%$ at a wavelength of $\lambda = 528\,\mathrm{nm}$ is thermoelectrically cooled to a temperature

of 0 °C. The full-well capacity (maximum number of photoelectrons) that can be stored on a pixel is $FW = 30000$. The camera's noise specifications are given as a number of electrons. It features low median read noise of $N_\mathrm{r} = 0.9$ and a dark current of $D = 0.10\,\mathrm{s}^{-1}$ per pixel. The dynamic range of 33000:1 is sampled with a bit depth of 16 bit. The communication with the camera is established through USB 3.0 and supports frame rates of up to 53 frames per second (fps) when capturing the full field of view or up to 1627 fps when imaging a 128 x 128 pixel region of interest.

The achievable polarized light contrast depends on the extinction ratio of the polarizer and analyzer, as well as on the depolarizing effects occurring at the optics in between the polarizer and analyzer. Due to their compact size and moderate cost, polarizers based on oriented silver nanoparticles featuring an extinction ratio exceeding $\kappa = 1 \times 10^{-5}$ at a wavelength of 528 nm are used. Depolarizing effects occuring at the optical elements between polarizer and analyzer [65] lead to a reduction of the extinction ratio to a value around $\kappa = 1 \times 10^{-2}$.

The polarization sensitivity can be estimated based on the extinction ratio of the microscope and the camera specifications. The signal is given by the number of photoelectrons $N = M \cdot B \cdot P \cdot t \cdot QE$ that are generated by a photon flux P during the exposure time t on a pixel with the quantum efficiency QE for integrating over M exposures and binning of B pixels. The noise sources contributing to the overall noise are: the signal related shot noise $\delta_\mathrm{shot} = \sqrt{N}$, dark noise $\delta_\mathrm{dark} = \sqrt{M \cdot B \cdot D \cdot t}$ due to thermally generated electrons and readout noise $\delta_\mathrm{read} = \sqrt{M \cdot B} \cdot N_\mathrm{r}$. By adding the noise contributions in quadrature, the signal-to-noise ratio

$$\mathrm{SNR} = \sqrt{M \cdot B} \cdot \frac{P \cdot t \cdot QE}{\sqrt{P \cdot t \cdot QE + D \cdot t + N_\mathrm{r}^2}} \,. \tag{3.1}$$

is derived.

The SNR increases with the square root of the number of integrated images and binned pixels. In polarized light imaging, the signal N has to be substituted by the difference in photoelectrons that is generated by a rotation of the plane of polarization by an angle θ. This is a function of the analyzer angle β and is given by $N_\mathrm{pol} = N \cdot (1-\kappa)(\sin^2(\beta+\theta) - \sin^2(\beta))$. The shot noise has to be replaced by the expression $\delta_\mathrm{shot} = \sqrt{N \cdot ((1-\kappa) \cdot \sin^2(\beta+\theta) + \kappa)}$. If it is further considered that the full well capacity FW (maximum number of photoelectrons) of a camera pixel is limited, it can be seen that the

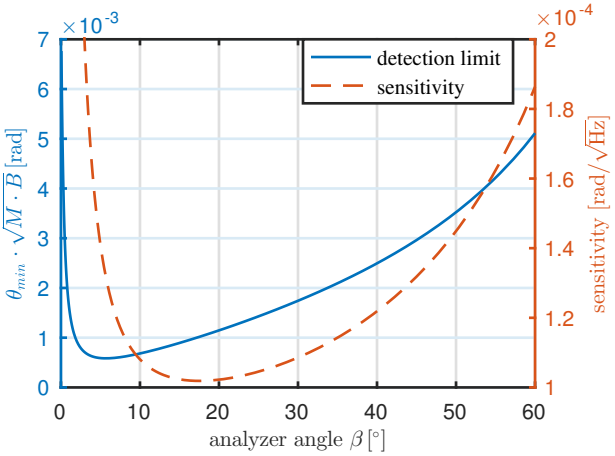

Figure 3.5: Detection limit $\theta_{min}\sqrt{M \cdot B}$ (solid blue line) and sensitivity (dashed red line) as a function of analyzer angle. From [24].

highest SNR for a single exposure is achieved after an exposure time of $t_1 = FW/\left(P \cdot QE\left((1-\kappa)\sin^2(\beta+\theta)+\kappa\right)\right)$. With this it is possible to evaluate the smallest angle θ_{min}, the detection limit, that can be measured with a SNR of 1 as a function of analyzer angle β for a exposure time of t_1. As can be seen in Fig. 3.5, a detection limit of $\theta_{\mathrm{min}}\sqrt{M \cdot B} = 6 \times 10^{-4}\,\mathrm{rad}$ is reached for an analyzer angle of $\beta = 5.7\,°$. However, since the exposure time increases with decreasing analyzer angle β, the highest sensitivity of $\theta_{\mathrm{min}}\sqrt{t_1} = 1.0 \times 10^{-4}\,\mathrm{rad}/\sqrt{\mathrm{Hz}}$ is realized for an analyzer angle of $\beta = 17.6\,°$.

The magnification m_{wf} of the image, formed by the tube lens on the camera sensor, is determined by the ratio of the 200 mm focal length f_{TL} of the tube lens and the 4 mm focal length f_{MO} of the microscope objective, divided by the angular magnification M_{AFR} of the afocal relay (see Sec. 3.3.3). This results in a total magnification of $m_{\mathrm{wf}} = f_{\mathrm{TL}}/(f_{\mathrm{MO}}\,M_{\mathrm{AFR}}) \approx 27$. The diffraction limited resolution at a wavelength of 528 nm and for the NA of 0.8 is given by the Rayleigh criterion $d_{\mathrm{min}} = 0.61\,\lambda/\mathrm{NA} = 403\,\mathrm{nm}$, which equals to about 11μm on the camera sensor. The image is sampled with a resolution of $d_{\mathrm{px}} = 6.5\,\mu\mathrm{m}$ on the image sensor. Therefore, the achievable

resolution is effectively limited by the Nyquist sampling theorem and is given by

$$d_{\mathrm{eff}} = \frac{2\,d_{\mathrm{px}}}{m_{\mathrm{wf}}} = 481\,\mathrm{nm}\ . \tag{3.2}$$

3.3 Low-temperature scanning polarizing microscope (LTSPM)

In principle, two different scanning mechanisms can be utilized in scanning laser microscopy. First, there is mechanical scanning, where either the microscope or the sample is moved with piezo drives or stepper motors. The second possibility is optomechanical scanning, where the optical path is modified by a movable component, for example a mirror, so that the laser spot changes its position on the sample. A decision in favor of optomechanical scanning has been made, because it offers several advantages over mechanical scanning. While providing a very good spatial resolution, optomechanical scanning has the advantage of a larger field of view and enables faster acquisition rates. Another benefit is that electromagnetic noise, that is generated by piezo drives and could disturb measurements of the electric transport properties of a sample, is avoided. Additionally, if the sample is to be mounted in a cryostat, good thermal coupling of the sample to the coldfinger is easily achieved. However, in optomechanical scanning, greatest care has to be taken to ensure that the modification of the lightpath doesn't cause abberrations that prevent diffraction limited imaging or lead to a non-negligible influence on the polarization state. Therefore, all the components that are used in the beam scanning part of the microscope need to be polarization maintaining and designed for confocal scanning.

Hereafter, a general description of the LTSPM setup, shown in Fig. 3.2, is given and subsequently, the individual components are discussed in detail. The light source for the LTSPM is a 405 nm wavelength laser diode coupled into a single-mode polarization maintaining fiber. The fiber output is collimated and the beam diameter is defined by an adjustable aperture stop. The plane of polarization is defined by a Glan-Thompson polarizer. The light passes a polarization-maintaining beam splitter (PMBS-1) with a splitting ratio of 50:50, the light that is deflected by the beam splitter is captured by a photodiode and is used as feedback for the stabilization of the laser intensity. The transmitted light is deflected by a two-axis fast-steering

mirror (FSM), which is used to set the position of the laser spot on the sample. The mirror is in a conjugate plane to the back focal plane (aperture plane AP) of the infinity corrected microscope objective. An afocal relay is used to image the mirror onto the back focal plane. The angular position of the FSM thereby defines the XY-position of the laser spot on the sample. This results in a telecentric illumination of the sample, where the beam is reflected and consequently passes the microscope objective, afocal relay and FSM in opposite direction. The light is then deflected by the PMBS-1. A quarter-wave plate ($\lambda/4$) is used to correct for the ellipticity of the reflected beam's polarization and a half-wave plate ($\lambda/2$) can be used to rotate the plane of polarization. A beamreducer is necessary to match the beam diameter to the size of the photodiodes. In the intermediate image plane of the beamreducer, a pinhole aperture is inserted to make the microscope confocal. The beam then passes a 405 nm center wavelength band-pass filter and is split into two perpendicularly polarized beams by the Wollaston prism. These two beams are detected using two quadrant photodiodes.

3.3.1 Light source

The key requirements for the light source are long-term stability and low noise. The light source consists of a temperature-stabilized diode laser with a wavelength of $\lambda = 405\,\text{nm}$ and a maximum output power of $P_{\text{max}} = 50\,\text{mW}$, which is coupled into a polarization maintaining single-mode fiber. The control electronics of the laser diode operate on a battery power supply to reduce noise and the output power is controlled using the photodiode at the PMBS-1 as feedback. The laser power can be modulated with frequencies up to $f_{\text{max}} = 1\,\text{MHz}$.

3.3.2 Fast-steering mirror (FSM)

Laser-beam scanning can be accomplished by means of galvanometric scanners [66], acousto-optical deflectors [67] or fast-steering mirrors. Galvanometric scanners and acousto-optic deflectors provide angular displacement of the beam about a single axis. Therefore, it is necessary to use two separate scanners in a perpendicular orientation to achieve XY-scanning. Unless additional relay optics are used in between the two scanners, this results in linear displacement of the laser beam from the optical axis. The main advantage of fast-steering mirrors is that they provide angular displacement

about two perpendicular axes in a single device. Thus, the mirror can be placed in a conjugate plane to the back focal plane of the microscope objective. This results in pure angular displacement of the beam and a telecentric illumination of the sample. Here, a two-axis fast-steering mirror with a mechanical scan range of $\pm 1.5\,^\circ$ and an angular resolution of better than $2\,\mu$rad is used.

As has been discussed by Ping *et al.* [68], reflection of a linearly polarized laser beam at a mirror surface will lead to depolarization, caused by the difference in reflectivity and phase for s- and p-polarized light, if the beam is not purely s- or p-polarized. Pure s- or p-polarization can only be realized for a single scan axis. Since a two-axis scan mirror is used, depolarizing effects cannot be avoided.

The depolarizing effects occurring at the mirror can easily be evaluated using the Jones calculus [16, 69] introduced in Sec. 2.5. The Jones matrix for a mirror is defined in the mirrors coordinate system with axes perpendicular (s) and parallel (p) to the plane of incidence. The reflection-coefficients $r_\mathrm{p}(\alpha)$, $r_\mathrm{s}(\alpha)$ and the phase difference $\delta(\alpha)$ are a function of the angle of incidence α. The Jones matrix for a two-axis scan mirror at an azimuth angle α and inclination β is calculated by applying a coordinate transformation, a rotation $\boldsymbol{R}(\beta)$, to the mirrors coordinate system.

$$\boldsymbol{M}(\alpha,\beta) = \boldsymbol{R}(-\beta) \begin{pmatrix} r_\mathrm{p}(\alpha) & 0 \\ 0 & r_\mathrm{s}(\alpha) e^{\mathrm{i}\delta(\alpha)} \end{pmatrix} \boldsymbol{R}(\beta)\ . \tag{3.3}$$

By considering a rotation of the plane of polarization by an angle θ_MO through a magneto-optical effect and the fact that the light is reflected twice by the mirror, the resulting polarizing state $\boldsymbol{E}_\mathbf{out}$ for a given initial polarization state $\boldsymbol{E}_\mathbf{in}$ is given by

$$\boldsymbol{E}_\mathbf{out} = \boldsymbol{M}(\alpha,\beta)\boldsymbol{R}(\theta_\mathrm{MO})\boldsymbol{M}(\alpha,\beta)\boldsymbol{E}_\mathbf{in}\ . \tag{3.4}$$

To minimize depolarizing effects, a dielectric mirror (*Layertec 107810*) with a phase difference of less than $5\,^\circ$ and a reflectivity difference below $0.05\,\%$ for s- and p-polarized light at angles of incidence of $45 \pm 3^\circ$ and a wavelength of 405 nm is used. The error introduced by this mirror is evaluated according to Eq. (3.4). The dominant error is a gradient in the orientation of the polarization for scanning along the β direction. This can be seen as a gradient of roughly $1.6\,\mu\mathrm{rad}/\mu\mathrm{m}$ along the y-direction in the image plane.

3.3.3 The afocal relay (AFR)

In confocal laser beam scanning microscopy, the laser spot is scanned across the sample by pivoting the laser beam in the back focal plane of the microscope objective. To achieve this, the scan mirror is imaged into the back focal plane using an afocal relay. Here, the microscope objective is mounted inside the cryostat and consequently a vacuum window is needed at some point before the beam enters the microscope objective. Instead of a dedicated vacuum window, one of the lenses of the afocal relay serves as the vacuum window.

An afocal relay is realized by combining two focal systems in such a way that the rear focal point of the first focal system is coincident with the front focal point of the second focal system. A collimated beam entering the first focal system will exit the second focal system as a collimated beam. The linear magnification $m = f_2/f_1$ and the angular magnification $M = f_1/f_2$ are determined by the equivalent focal lengths f_1 and f_2 of the first and second focal system, respectively. Cemented achromatic doublets are often used to realize relay lenses. However, they are not well suited for confocal imaging, mainly because of the astigmatism and field curvature they introduce [70, 71]. Therefore, more complex lens systems need to be used, which are designed to correct these aberrations. Air spaced triplets are used as a starting point for the two lens groups that make up the afocal relay, since they offer sufficient degrees of freedom to be made anastigmatic [72]. However, a fourth lens, which acts as the cryostat window, has to be added to the lens group facing the microscope objective, because the mechanical stress exerted by the vacuum needs to be handled.

The afocal relay has been specifically designed for use with the microscope objective and scan mirror. It has an angular magnification of $M_{\mathrm{AFR}} = 1.85$, so that the range of the scan mirror is matched to the field of view of the microscope objective, and the rear aperture of the microscope objective will be completely filled using a laser beam with a diameter of 12 mm. The relay consists of two lens groups: a triplet of two bi-convex and one bi-concave lenses and a quadruplet of two bi-convex, one bi-concave and one meniscus lens (Fig. 3.6). The two lens groups are aligned as a 4f system, with the scan mirror placed in the front focal plane of the triplet lens group and the microscope objective back focal plane being coincident with the back focal plane of the quadruplet lens group. The lens parameters for the afocal relay are given in table 3.1.

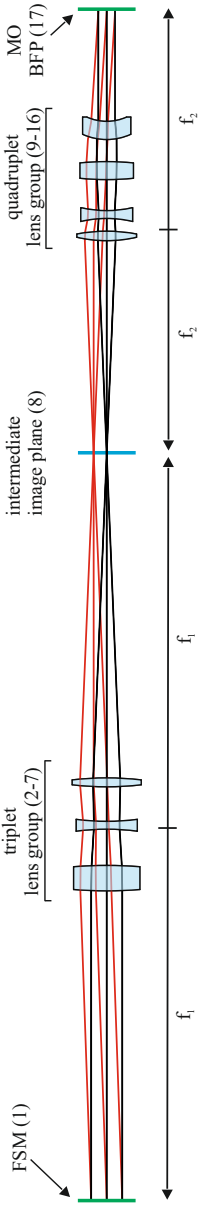

Figure 3.6: Layout of the afocal relay. Two lens groups, one triplet and one quadruplet, are used to relay the fast-steering mirror (FSM) onto the microscope objective's back focal plane (MO-BFP). The FSM is placed in the entrance pupil on the left side, the MO-BFP is coincident with the exit pupil on the right side. The rightmost lens of the quadruplet, a meniscus lens, is used as the cryostat window. The surface numbering is consistent with table 3.1. From [24].

Table 3.1: Lens data for the AFR: Radius of curvature of the surfaces defining the optical system and their separation along the optical axis. Material specifies the medium that fills the space between the current surface and the next surface. The surface numbering is consistent with Fig. 3.6.

surface no.	radius [mm]	separation [mm]	material	description
1	inf	119.637	air	entrance pupil
2	159.604	9.809	N-LASF44	bi-convex
3	-159.604	14.000	air	lens
4	-89.906	3.000	SF1	bi-concave
5	89.906	13.356	air	lens
6	113.967	3.431	N-BAF10	bi-convex
7	-113.967	125.237	air	lens
8	inf	82.248	air	intermediate image plane
9	50.810	3.647	N-LAF34	bi-convex
10	-61.500	4.945	air	lens
11	-43.268	3.000	SF1	bi-concave
12	43.268	12.000	air	lens
13	104.606	6.928	N-LAK33A	bi-convex
14	-104.606	8.549	air	lens
15	22.402	7.000	SF57HHT	meniscus lens and cryostat
16	18.607	42.571	vacuum	window
17	inf			exit pupil

The AFR design has been optimized using a ray tracing software, Zemax OpticStudio [73], to reduce all aberrations, especially astigmatism, coma, spherical aberration, field curvature and distortion for wavelengths of $\lambda = 405\,\mathrm{nm}$ and $\lambda = 528\,\mathrm{nm}$. Since the relay needs to be polarization maintaining, the design has also been optimized in this regard, including strain-free mounting of the lenses. The meniscus lens acts as the cryostat window and is, unavoidably, under considerable mechanical stress. This lens was not only optimized with regard to its optical performance but also with regard to the mechanical demands imposed by the vacuum. This lens has been fabricated from SF57HHT glass, which has an extremely low stress-optical coefficient, to minimize stress birefringence. Optical performance of the relay is diffraction limited over the entire scan range, which is essential for confocal imaging.

3.3.4 Beam reducer, confocal pinhole and resolution

The beam reducer is built from two commercial achromatic doublets with a design wavelength of 405 nm. They have equivalent focal lengths of $f_{\mathrm{BR1}} = 125\,\mathrm{mm}$ and $f_{\mathrm{BR2}} = 25\,\mathrm{mm}$, so that the exiting beam is matched to the photodiode diameter of 2.5 mm. The confocal pinhole aperture is mounted in the intermediate image plane of the beamreducer, which is a conjugate plane to the sample, and consequently blocks light that is not originating from the focal volume. The pinhole diameter d_{ph} is determined by the diameter of the airy disc and the magnification $m_{\mathrm{cf}} = f_{\mathrm{BR1}}/(f_{\mathrm{MO}}\, M_{\mathrm{AFR}})$ of the microscope. It is given in Airy units (AU), with 1 AU being the diameter of the image of the airy disc in the intermediate image plane of the beamreducer. The 125 mm achromat was selected, so that $1\,\mathrm{AU} = 10\,\mu\mathrm{m}$, with

$$1\mathrm{AU} = \frac{1.22\,\lambda}{\mathrm{NA}}\, m_{\mathrm{cf}}\ . \tag{3.5}$$

The resolution in confocal microscopy is increased by 28 % in comparison to widefield microscopy. In widefield microscopy, the resolution is given by the distance between two points for which their point spread functions (PSF) can be distinguished and is expressed by the Rayleigh criterion $d_{\mathrm{min}} = 0.61\,\lambda/\mathrm{NA}$. In the Rayleigh criterion, the point spread function is described by the Airy disk. Two point sources are considered to be resolvable, if the first minimum of the Airy disk of one point coincides with the global maximum of the other. In this case, the combined intensity

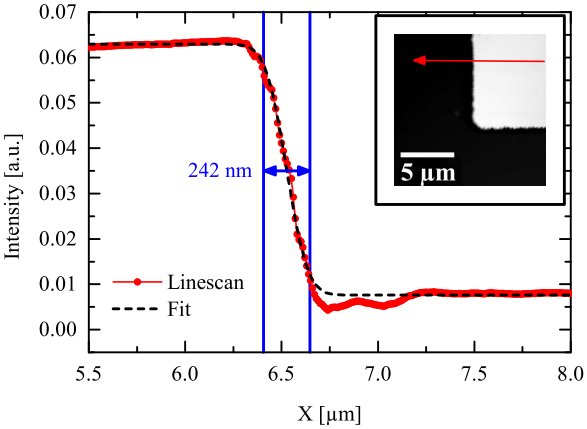

Figure 3.7: Resolution of the LTSPM. Linescan (red) across the structure shown in the inset. The red arrow indicates the position and direction of the linescan. The data has been fitted (dashed black line) using Eq. (3.8). A resolution of 242 nm is achieved. From [24].

profile shows a dip of $\approx 26\,\%$ between the maxima corresponding to the two points. The increase in resolution in confocal microscopy originates from the fact, that the confocal volume is defined by the product of the illumination PSF and the convolution of the detection PSF with the pinhole [47]. For a pinhole with a diameter of 0.5 AU, this results in a function with a sharper peak compared to the widefield PSF. In this case, the confocal resolution d_{cf} is given by

$$d_{\mathrm{cf}} = \frac{0.44\,\lambda}{\mathrm{NA}} = \frac{0.44 \cdot 405\,\mathrm{nm}}{0.8} = 222\,\mathrm{nm}\ . \tag{3.6}$$

Using pinholes smaller than 0.5 AU does not increase the resolution, but deteriorates the SNR. A linescan across the edge of a patterned structure is shown in Fig. 3.7. A confocal pinhole of 0.5 AU diameter was used for the acquisition of the image and the linescan. The intensity profile of the linescan can be used to evaluate the width of the PSF and the corresponding

resolution. For a Gaussian laser beam, the PSF has a Gaussian profile with maximum intensity I_0 and 1/e-width ω

$$I(x,y) = I_0\,\mathrm{e}^{-\frac{(x^2+y^2)}{\omega^2}} \quad . \tag{3.7}$$

The edge-spread function (ESF), obtained by scanning over a sharp edge at $x = 0$, is the convolution of the PSF at position X and the edge profile defined by a reflectance R_1 for $x < 0$ and R_2 for $x \geq 0$. The ESF is given by

$$\begin{aligned} P(X) &= \pi\omega^2 I_0 R_1 - R_1 \int_{-\infty}^{0}\int_{-\infty}^{\infty} I(x-X,y)\,\mathrm{d}x\,\mathrm{d}y \\ &\quad + R_2 \int_{0}^{\infty}\int_{-\infty}^{\infty} I(x-X,y)\,\mathrm{d}x\,\mathrm{d}y \\ &= \pi\omega^2 I_0 \left[\frac{R_1}{2}\left(1-\operatorname{erf}\frac{X}{\omega}\right) + \frac{R_2}{2}\left(1+\operatorname{erf}\frac{X}{\omega}\right)\right] \quad . \end{aligned} \tag{3.8}$$

A resolution criterion for two Gaussian PSF at a distance d, that is similar to the Rayleigh criterion, is realized when their combined intensity profile shows a $\approx 26\,\%$ dip. This distance is related to the 1/e-width of the PSF by $d_{\mathrm{Rayleigh}} \approx 1.97\,\omega$. To determine the resolution, the linescan in Fig. 3.7 is fitted using Eq. (3.8), and a value for the 1/e-width of the PSF of $\omega = 122.6\,\mathrm{nm}$ is obtained. The resolution, according to the Rayleigh criterion, is found to be $d_{\mathrm{Rayleigh}} \approx 242\,\mathrm{nm}$, which is close to the theoretical value obtained from Eq. (3.6).

3.3.5 Detector

Detectors featuring a high sensitivity for the orientation of the plane of polarization θ are needed for polarized light microscopy. A useful measure to assess the detector sensitivity is the noise spectral density for the orientation of the plane of polarization $S_\theta^{1/2}$, given in $\mathrm{rad}/\sqrt{\mathrm{Hz}}$. Different approaches towards the measurement of the polarization of light have been employed for scanning polarizing microscopy. The most basic one is the use of a polarizer that is rotated close to $90\,^\circ$ relative to the polarization of the beam. More advanced designs use photoelastic modulators [74] or Faraday

modulators [75] to modulate the polarization of the light before it is passed through the analyzer. This generates a signal at the second harmonic of the modulation frequency that is proportional to the Kerr rotation and a signal at the modulation frequency that is proportional to the Kerr ellipticity. Cormier *et al.* [76] measured a polarization noise of 0.3 mdeg for an integration time of 50 s using polarization modulation. This corresponds to a sensitivity of $3.7 \times 10^{-5}\,\mathrm{rad}/\sqrt{\mathrm{Hz}}$. Another approach is to use a differential detector [77]. Flajšman *et al.* [78] report a sensitivity of $5 \times 10^{-7}\,\mathrm{rad}$ using a differential detector, however they do not provide information on the bandwidth of this measurement. Spielmann *et al.* [79] developed a detector based on a Sagnac interferometer. A sensitivity of $1 \times 10^{-7}\,\mathrm{rad}/\sqrt{\mathrm{Hz}}$ using a Sagnac interferometer was demonstrated by Xia *et al.* [80].

The detector for the LTSPM is a differential detector based on the design by Clegg *et al.* [81]. It uses a Wollaston prism to split the incident beam into two beams with orthogonal polarization [Fig. 3.8 (a)] with intensities $I_1 \propto I_0 \sin^2\theta$ and $I_2 \propto I_0 \cos^2\theta$, for an incident beam with intensity I_0 and linear polarization at an angle θ relative to the s-polarized beam. The orientation of the polarization, the angle θ, can be extracted from the intensities I_1 and I_2

$$I_2 - I_1 = I_0(\cos^2\theta - \sin^2\theta) = I_0\cos(2\theta) \tag{3.9}$$

$$\theta = \frac{1}{2}\arccos\left(\frac{I_2 - I_1}{I_0}\right) = \frac{1}{2}\arccos\left(\frac{I_2 - I_1}{I_1 + I_2}\right)\ . \tag{3.10}$$

Note that, with this detection mechanism, the orientation of the plane of polarization can be measured independently from the intensity I_0. This differential detection scheme is an important feature, because it cancels to a high degree variations in reflectivity that may occur due to the sample topography.

The intensity of the two beams is measured using two quadrant photodiodes. Since the microscope objective focuses the beam onto the sample and the quadrant photodiodes are in a conjugate plane to the back focal plane of the microscope objective, each of the quadrants corresponds to a unique range of angles of incidence , as shown in Fig. 3.8 (b). Furthermore, opposite quadrants correspond to opposite angles of incidence. Because the longitudinal MOKE is an odd function of angle of incidence, while the polar MOKE is an even function of angle of incidence, the polar and longitudinal

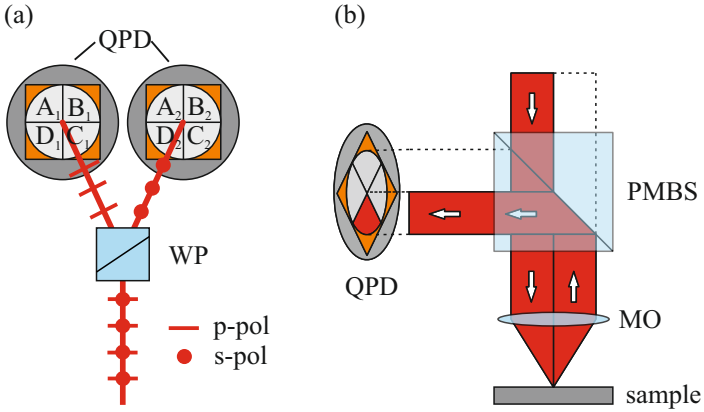

Figure 3.8: Selection of the illumination path for the LTSPM detector. (a) Scheme of the detector: the beam is split into two orthogonally polarized beams by the Wollaston prism (WP). These beams are detected by two quadrant photodiodes (QPD). (b) Simplified lightpath for the read out of one quadrant. Each quadrant corresponds to a different illumination direction. From [24].

MOKE can be separated by measuring the Kerr rotation individually for every quadrant [81, 82]. For a quadrant X, the plane of polarization is given by

$$\theta_X = \frac{1}{2} \arccos\left(\frac{I_{X2} - I_{X1}}{I_{X1} + I_{X2}}\right), \; X = \{\mathrm{A}, \mathrm{B}, \mathrm{C}, \mathrm{D}\} \; . \tag{3.11}$$

In total, six different signals can be measured simultaneously. The polar Kerr signal $\theta_{\mathrm{K}}^{\mathrm{polar}}$ which is sensitive to the out-of-plane magnetization

$$\theta_{\mathrm{K}}^{\mathrm{polar}} = \theta_{\mathrm{A}} + \theta_{\mathrm{B}} + \theta_{\mathrm{C}} + \theta_{\mathrm{D}} \; , \tag{3.12}$$

the longitudinal Kerr signal $\theta_{\mathrm{K},ij}^{\mathrm{long}}$ which is sensitive to the magnetization component along the $ij = \{\mathrm{xy}, \mathrm{x\bar{y}}, \mathrm{x}, \mathrm{y}\}$ direction in the image plane

$$\theta_{\mathrm{K},\mathrm{x\bar{y}}}^{\mathrm{long}} = \theta_{\mathrm{A}} - \theta_{\mathrm{C}} \tag{3.13}$$

$$\theta_{\mathrm{K},\mathrm{xy}}^{\mathrm{long}} = \theta_{\mathrm{D}} - \theta_{\mathrm{B}} \tag{3.14}$$

$$\theta_{\mathrm{K,y}}^{\mathrm{long}} = (\theta_{\mathrm{C}} + \theta_{\mathrm{D}}) - (\theta_{\mathrm{A}} + \theta_{\mathrm{B}}) \tag{3.15}$$

$$\theta_{\mathrm{K,x}}^{\mathrm{long}} = (\theta_{\mathrm{A}} + \theta_{\mathrm{D}}) - (\theta_{\mathrm{B}} + \theta_{\mathrm{C}}) \tag{3.16}$$

and the reflected intensity (conventional image)

$$I_{\mathrm{tot}} = \sum_{X=\{\mathrm{A,B,C,D}\}} I_{X1} + I_{X2} \ . \tag{3.17}$$

For reasons of noise suppression and dc error cancellation of the electronics, the measurement is performed in a lock-in configuration where the laser is modulated with a frequency of several kHz and a lock-in amplifier is used to extract the signal. The photocurrent from each quadrant is converted to a voltage using a transimpedance amplifier with a gain of $G_{\mathrm{TI}} = 2\,\mathrm{MV/A}$. A second programmable gain amplifier (PGA) stage provides additional gain from $G = 1$ to $G = 8000$. The PGA is ac-coupled by inserting a high-pass filter with a cut-off frequency $f_{\mathrm{c}} = 200\,\mathrm{Hz}$ at the input of the PGA. The output of the PGAs is recorded with a sampling rate of 2 MHz and a resolution of 16 bit by a simultaneous sampling data acquisition card. The signal is demodulated using a software-based lock-in algorithm.

3.3.6 Noise considerations

The different noise sources contributing to the overall system noise can be divided into three main parts: laser intensity noise, detector noise and mechanical noise. The laser intensity noise consists of the shot noise and excess noise related to the pump current, mode hopping, thermal fluctuations, etc. The excess noise can be reduced by measuring the output power and using it as feedback to control the pump current, as well as stabilizing the temperature of the laser diode. The shot noise, however, cannot be overcome and is a fundamental limit to the intensity noise. Since the orientation of the plane of polarization is measured using a balanced detector, laser intensity noise is canceled to a high degree.

The detector noise is produced by the electronic components within the detector and does not depend on the signal reaching the detector. The dark noise of one quadrant of the detector, measured at the output of the PGA, is shown by the green curve in Fig. 3.9 (a). The dark noise at the output of the digital lock-in amplifier, for a reference frequency of $f_{\mathrm{ref}} = 10\,\mathrm{kHz}$ and a integration time of $t_{\mathrm{int}} = 1\,\mathrm{ms}$ is shown in red. Using lock-in detection shifts

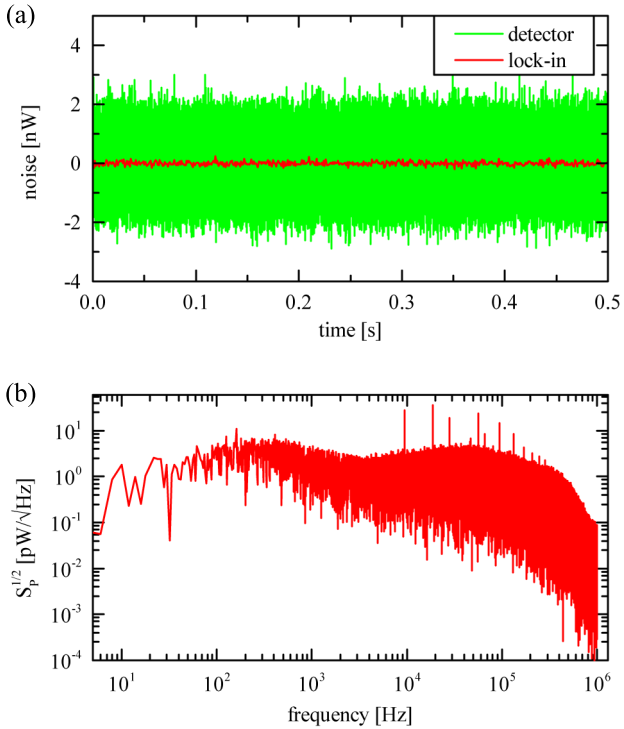

Figure 3.9: Noise characteristics of the detector: (a) Detector noise at the PGA output (green) and after lock-in detection with $f_{\mathrm{ref}} = 10\,\mathrm{kHz}$, $t_{\mathrm{int}} = 1\,\mathrm{ms}$ (red). Lock-in detection reduces noise by more than an order of magnitude. (b) Noise spectral density at the PGA output. $1/f$ noise is elliminated by ac-coupling the PGA.

the signal to higher frequencies, where the $1/f$ part of the noise is negligible. The rms noise at the output of the lock-in amplifier is proportional to the detection bandwidth, which is controlled by the lock-in integration time t_{int}. In the case of frequency independent white noise, it is calculated by dividing the noise spectral density $S_P^{1/2}$ at the PGA output by the square root ot the integration time, and is given by $\Delta P_{\mathrm{rms}} = S_P^{1/2}/\sqrt{t_{\mathrm{int}}}$. The noise spectral density for the PGA output is shown in Fig. 3.9 (b). Noise below the cut-off frequency ($f_{\mathrm{c}} = 200\,\mathrm{Hz}$) of the ac-coupling filter is suppressed and $1/f$ noise is practically eliminated. The lock-in detection results in a noise reduction of more than one order of magnitude that can be further increased by increasing the integration time.

An additional noise source is mechanical noise, which is related to perturbations to the imaging path caused by vibrations, noise in the angular position of the FSM, vibrations of the coldfinger, etc. A value of $5 \times 10^{-6}\,\mathrm{rad}/\sqrt{\mathrm{Hz}}$ for the sensitivity to the orientation of the plane of polarization has been determined for the LTSPM detector.

3.4 Imaging of electric transport properties

Imaging of electric transport properties using low-temperature scanning electron microscopy (LTSEM) has first been demonstrated by Stöhr *et al.* [83]. In LTSEM, the electron beam generates a local perturbation to the electric transport characteristics of typically a current-biased sample that leads to a global voltage response, which serves as image contrast. A general response theory for this imaging mechanism was developed by Clem *et al.* [84]. For a detailed description of the LTSEM technique see the reviews by Huebener [85] and by Gross *et al.* [86]. A similar technique using a focused laser beam to perturb the sample was used by Divin *et al.* [87, 88]. It was shown by Dieckmann *et al.* [89] that this technique, low-temperature scanning laser microscopy (LTSLM), delivers results that are equivalent to LTSEM. LTSLM has, among others, been applied to research on superconductors [51, 53, 90, 91], the quantum Hall effect [92], spintronics [93, 94], and spin-caloritronics [95]. The LTSPM can be operated in LTSLM mode to gain information on the electric transport properties of a sample. The intensity-modulated laser beam generates a periodic perturbation that leads to a periodic global voltage response ΔV, which can be measured with a lock-in amplifier (Fig. 3.10). Maps of the voltage

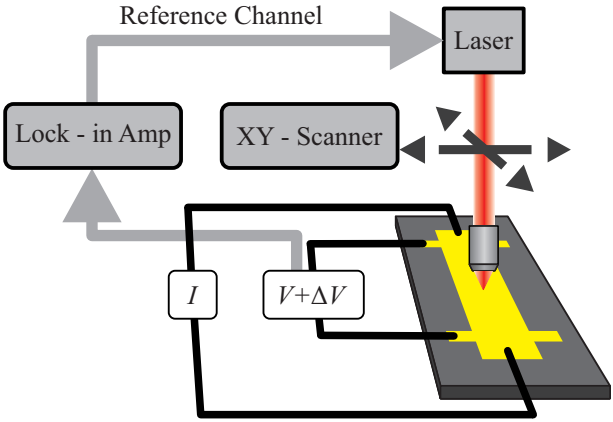

Figure 3.10: Principle for LTSLM imaging of local electric transport properties. The laser beam, that is intensity modulated at the reference frequency of the lock-in amplifier, locally perturbs the electric transport properties of the current-biased sample. The perturbation leads to a change ΔV in global voltage, which is detected by the lock-in amplifier. From [24].

response ΔV, the voltage image, can be acquired by scanning the laser across the sample. Usually, the primary nature of the perturbation is local heating [96], although additional mechanism such as the photovoltaic effect, photoconductivity or quasiparticle creation in superconductors [97] are possible and may need to be considered for the interpretation of these images. The spatial resolution of this technique is governed by the length scale on which the laser beam induced perturbation decays. In the case of local heating this is the thermal decay length [86] and a typical resolution of a few μm can be achieved.

3.5 Image processing

Because of the typically weak contrast in polarized light imaging, the application of digital image processing techniques is often necessary to extract the relevant information. In MOKE imaging, e.g. using the LTWPM, the magneto-optical signal is superimposed by differences in reflectivity and inhomogeneous illumination of the sample. The magneto-optical signal

throughout a hysteresis loop can, for example, be extracted by subtracting a reference image in which the sample shows a homogeneous magnetization, i.e. is in a saturated state. The open-source software FIJI [98] provides a wide range of functionalities that can be used for image processing in polarized light microscopy. Apart from the possibility to efficiently implement standard mathematical operations to large data sets, it includes a scripting interface that enables batch processing and custom image processing techniques. A particularly useful feature is a plugin ('StackReg') that can be used to automatically correct for sample drift between subsequent acquisitions with sub-pixel resolution [99].

3.6 Examples

In this Section, two examples demonstrating the capabilities of the microscope system are presented. First, the imaging of magnetic domains in barium hexaferrite is addressed. Second, the imaging of magnetic flux structures in superconductors is discussed. A detailed description of the underlying physics for these examples is omitted as it would go beyond the scope of this thesis. However, a short motivation and description for each study is given.

3.6.1 Magnetic domains in barium hexaferrite [3]

Magnetic domains in the basal plane of a barium hexaferrite crystal [$BaFe_{12}O_{19}(0001)$] observed with the LTSPM at room temperature and zero magnetic field are shown in Fig. 3.11 (a) and (b). This ferromagnetic material has been extensively studied by magnetic force microscopy and scanning Hall probe microscopy [100–102] as a substrate for superconductor-ferromagnet hybrids. The magnetic domains in $BaFe_{12}O_{19}(0001)$ form a labyrinth pattern with zigzag domain walls [102] in the remanent state. Due to its uniaxial anisotropy, the magnetization within the domains is parallel/anti-parallel to the [0001]-direction [101]. The width of the Bloch-type domain walls was found to be around 200 nm [100, 101]. For a superconductor-ferromagnet hybrid, where a superconducting film is deposited on top of a ferromagnetic substrate, the magnetic landscape within the superconducting film that is generated by the ferromagnetic

[3] The author thanks J. Fritzsche (K.U. Leuven) for providing the $BaFe_{12}O_{19}$ crystal.

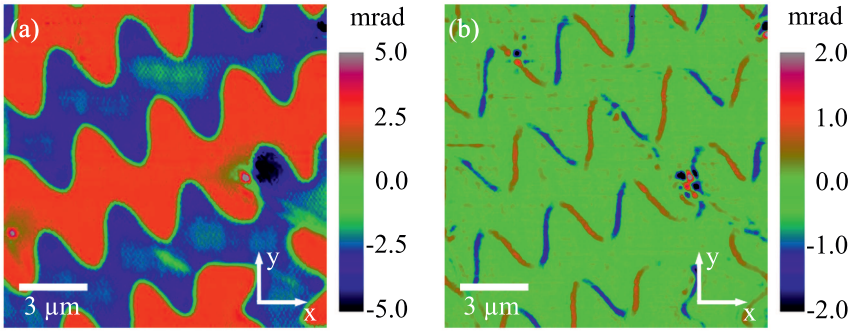

Figure 3.11: Magnetic domains in $BaFe_{12}O_{19}$ observed via (a) the polar MOKE θ_{K}^{polar} and (b) the longitudinal MOKE $\theta_{K,y}^{long}$ at room temperature and zero magnetic field. From [24].

substrate modifies the nucleation of superconductivity. This can lead to reverse-domain and domain-wall superconductivity, which has been imaged by LTSLM [103, 104]. The polar MOKE (θ_{K}^{polar}) image is shown in Fig. 3.11 (a). The zigzag folding of the domain walls between domains with magnetization parallel/antiparallel to the z-direction can clearly be seen. Fig. 3.11 (b) is acquired at the same time and displays the longitudinal MOKE ($\theta_{K,y}^{long}$) image, which is sensitive to the magnetization component along the y-direction. No contrast is obtained between adjacent domains, where the magnetization points in the out-of-plane/into-the-plane direction. However, a magneto-optical signal is obtained along the Bloch domain walls, where the magnetization has an in-plane component along the direction of the domain wall. Since the displayed longitudinal MOKE signal $\theta_{K,y}^{long}$ is only sensitive to the y-component of the magnetization, the contrast is best if the domain wall runs in y-direction and is lost if the domain walls run in x-direction.

3.6.2 Magneto-optical imaging of magnetic flux structures in superconductors

When a type-II superconductor is subjected to an external magnetic field that exceeds the lower critical field B_{c1}, flux enters into the superconductor in the form of Abrikosov vortices [105], characterized by a normal core

with a diameter of approximately twice the superconducting coherence length ξ_{GL} that is surrounded by a supercurrent that decays on the length-scale of the London penetration depth λ_{L}. Abrikosov vortices carry a quantized flux that is an integer multiple of the magnetic flux quantum $\Phi_0 = h/2e = 2.07 \times 10^{-5}\,\mathrm{Tm}^2$. In an ideal superconductor, the vortices would enter from the boundaries when B_{c1} is exceeded and would spread, due to a repulsive interaction between the individual vortices, within the superconductor until their interaction energy is minimized, resulting in a triangular vortex lattice. In a real superconductor, pinning centers that trap the vortices are always present. The penetration of flux into hard bulk superconductors, i.e. where pinning is strong, is described by the Bean model [106]. In thin films the magnetic field penetration differs from the Bean model and is described by the model by Norris [107], Brandt and Indenbom [108].

Experimentally, the magnetic field distribution above the surface of a superconductor can be determined using magneto-optical indicator films (MOIF) [109]. These consist of a magneto-optically active layer, often coated with a mirror, that is positioned on top of the superconductor. The Faraday effect in the MOIF leads to a rotation of the polarization of linearly polarized light that is proportional to the magnetic field and is given by $\vartheta_{\mathrm{F}} = 2VB_z d_{\mathrm{MOIF}}$ with the Verdet constant V, the magnetic field component along the propagation direction B_z and the thickness of the magneto-optically active layer d_{MOIF}. The magneto-optical imaging principle is illustrated in Fig. 3.12 for a MOIF that consists of a magneto-optically active layer and a mirror. The magnetic field distribution above the superconductor (type-II SC) is modulated by the presence of vortices. Without magnetic field, the magnetization of the magneto-optically active layer lies in the film plane. The magnetic field above the vortices leads to a rotation of the magnetization that now possesses an out-of-plane component. Under perpendicular illumination with polarized light, this out-of-plane component leads to a rotation of the plane of polarization by an angle ϑ_{F}, that can be visualized using polarized light microscopy. As the magnetic flux rapidly spreads above the surface of the superconductor, the achievable spatial resolution of this technique strongly depends on the distance z_0 between the MOIF and the sample. Magneto-optical imaging of single vortices has been demonstrated by Goa *et al.* [55] and Veshchunov *et al.* [110] using magneto-optical indicator films that are based on magneto-optically active ferrite-garnet films of composition $(\mathrm{Bi,Lu})_3(\mathrm{Fe,Ga})_5\mathrm{O}_{12}$ that exhibit large Verdet

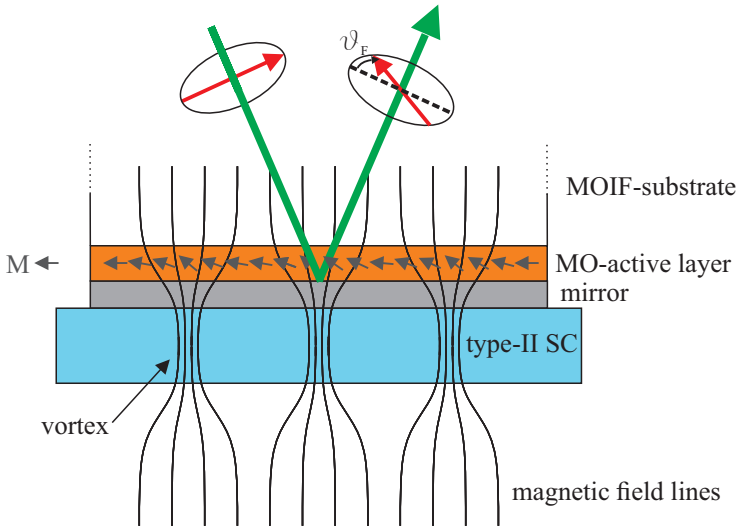

Figure 3.12: Magneto-optical imaging principle for the visualization of the magnetic field distribution above a superconductor (SC) containing three Abrikosov vortices. The magnetic field at the position of the magneto-optically active layer leads to a deflection of the magnetization M. The out-of-plane component of the magnetization leads to a rotation of the plane of polarization by an angle ϑ_F for linearly polarized light under perpendicular incidence.

constants of $V = 0.019\,^\circ/(\mathrm{mT}\,\mu\mathrm{m})$ [55] and $V = 0.06\,^\circ/(\mathrm{mT}\,\mu\mathrm{m})$ [110] at a temperature of 10 K. A key factor in achieving single vortex resolution is the minimization of the distance z_0 between MOIF and sample, as the maximum magnetic field modulation ΔB_z rapidly decays with increasing distance from the surface. Following the work by Carneiro and Brandt [111], Goa *et al.* [55] calculated the field distribution and ΔB_z as a function of distance to the surface. For a hexagonal lattice of vortices with a spacing of $2\,\mu$m, they found that the field modulation that is $\Delta B_z \approx 20\,\mathrm{mT}$ at the surface of the superconductor rapidly decreases with increasing distance from the surface, so that for a distance of $1.6\,\mu$m the magnetic field modulation ΔB is as low as $10\,\mu$T. The signal, i.e. the difference in Faraday rotation, $\Delta\vartheta_F$ results

from integrating the field modulation over the thickness of the indicator film

$$\Delta\vartheta_{\mathrm{F}} = 2V \int_{z_0}^{z_0+d_{\mathrm{MOIF}}} \Delta B_z(z)\ \mathrm{d}z\ . \tag{3.18}$$

It is evident that, to achieve single vortex resolution, the MOIF should exhibit a large Verdet constant and be as close as possible to the surface of the sample. The characterization and investigation of magneto-optical indicator films for low-temperature imaging of flux structures in superconductors was the subject of two state examination theses[4] by Felix Lever [60] and Theo Luibrand [112]. The MOIF that have been characterized in these theses, have kindly been provided by Morris Lindner (Innovent e.V., Jena). The MOIF employ a bismuth substituted rare-earth (RE) iron garnet layer, of composition $(\mathrm{Bi,RE})_3(\mathrm{Fe,Ga})_5\mathrm{O}_{12}$, as the magneto-optically active element and have been grown by liquid phase epitaxy on a gadolinium gallium garnet ($\mathrm{Gd_3Ga_5O_{12}}$) substrate. The standard version of the MOIF is covered with a mirror layer and a protective layer of diamond-like carbon (DLC) with an integral thickness of $4\,\mu$m. The response of ferrite-garnet based MOIF to external magnetic fields can be tuned by balancing the different contributions to their anisotropy. In general, it is attempted to realize films that have an easy axis in the film plane and show a continuous Stoner-Wohlfahrt [113] rotation of their magnetization when subjected to perpendicular magnetic fields. Neglecting the cubic crystalline anisotropy, the magnetic anisotropy of ferrite-garnet based MOIF can be described by an effective uniaxial anisotropy $K_{\mathrm{u}}^{\mathrm{eff}}$ perpendicular to the film surface that consist of the following contributions [15]

$$K_{\mathrm{u}}^{\mathrm{eff}} = K_{\mathrm{u}}^{\mathrm{g}} + 2B_1 e - \frac{\mu_0 M_{\mathrm{s}}^2}{2} + \frac{K_{\mathrm{Su}}}{d_{\mathrm{MOIF}}}\ , \tag{3.19}$$

where $K_{\mathrm{u}}^{\mathrm{g}}$ is a growth-induced anisotropy, $\mu_0 M_{\mathrm{s}}^2/2$ is the shape anisotropy with the saturation magnetization M_{s}, $2B_1 e$ is the magnetoelastic anisotropy with the cubic magnetostrictive constant B_1 and strain e, and $K_{\mathrm{Su}}/d_{\mathrm{MOIF}}$ is a surface contribution that can be neglected for films with $d_{\mathrm{MOIF}} > 1\,\mu$m. Due to the small mismatch between substrate and ferrite-garnet film, the magnetoelastic contribution can usually be neglected. The growth-induced

[4] Both the work by F. Lever and the work by T. Luibrand has been performed under my supervision.

anisotropy K_u^g can be tailored by adjusting the chemical composition [114] and deposition parameters. By balancing the growth-induced anisotropy and the shape anisotropy, films with small and negative effective uniaxial anisotropy $K_u^{eff} < 0$ can be realized. As a result, the magnetization, lying in the film plane in zero field, can be easily deflected by an external magnetic field which results in a high sensitivity and large effective Verdet constant.

Three different standard MOIF, provided by Innovent e.V. Jena, were examined in the thesis by F. Lever [60]: A so-called 'Type C' MOIF with a thickness of $d_{MOIF} = 4\,\mu m$, a saturation magnetization of $M_s = 130\,kA/m$, and a dielectric mirror plus DLC protective layer with a common thickness of $3 - 4\,\mu m$. A so-called 'Type B' MOIF with a thickness of $d_{MOIF} = 4.9\,\mu m$, a saturation magnetization of $M_s = 30\,kA/m$, and a dielectric mirror plus DLC protective layer with a common thickness of $3 - 4\,\mu m$. And finally, a 'Type B' MOIF with a thickness of $d_{MOIF} = 5.1\,\mu m$, a saturation magnetization of $M_s < 30\,kA/m$, and a 100 nm thick aluminum mirror. The low-temperature characterization of these MOIF revealed an increasing influence of the cubic crystalline anisotropy with decreasing temperature that leads to the appearance of domains and hysteresis. Nevertheless, imaging of flux structures in a niobium thin film has been achieved using the 'Type B' MOIF with dielectric mirror (see Sec. 3.6.2). Because of the relatively thick protective layer and mirror, the MOIF is at a distance to the superconductor where it is not possible to resolve the stray field of individual vortices. For a detailed description of the low-temperature characteristics of these MOIF see Ref. [60].

Because the relatively thick mirror and protective layer, as well as unnecessarily thick ferrite-garnet films, were suspected to limit the achievable spatial resolution, thinner films without mirror and protective layer have been prepared and investigated in the ensuing thesis by T. Luibrand [112]. These were four MOIF of 'Type B' with different thicknesses (200 nm, 350 nm, 660 nm, and 1.35 μm). Since the mirror layer on the MOIF was omitted, the light was reflected directly by the sample which served as the mirror. Only the two thickest MOIF showed the expected magneto-optical response with Verdet constants of $V = 0.016\,°/(mT\,\mu m)$ and $V = 0.026\,°/(mT\,\mu m)$ for the 660 nm and 1.35 μm thick film, respectively. The Verdet constant of these films is comparable to the MOIF used by Goa *et al.* [55]. Although the Verdet constant should be sufficiently large and it should be possible to bring the MOIF closer to the sample without the mirror and protective layer, single vortex resolution could not be achieved. It is likely that this is

due to dirt and particles on the sample surface which still leads to a too large sample to MOIF spacing. First attempts at mounting the sample and MOIF in a cleanroom have been made that hopefully will lead to improved resolution and single vortex imaging in the near future. More details on this topic can be found in Ref. [112].

Flux structures in Nb thin films [5]

As an example for the imaging of magnetic flux in superconductors, a study of the penetration of vortices into a superconducting resonator is presented. The measurements have been conducted by Felix Lever as part of his state examination theses [60]. The performance of superconducting niobium coplanar half-wavelength resonators for hybrid quantum systems in perpendicular magnetic fields is detrimentally affected by the presence of Abrikosov vortices [115–117]. The motion of Abrikosov vortices leads to energy dissipation and hence to increased losses that reduce the quality factor of the resonator. Fig. 3.13 (a) shows an optical image of a capacitatively coupled niobium half-wavelength resonator. The ground planes and the center conductor are the bright parts, while the gaps between them appear dark. The penetration of magnetic flux into the part of the resonator that is highlighted by the blue square has been investigated using the LTWPM and a MOIF. The MOIF used for this study was the 'Type B' indicator film with a thickness of 4.9 μm and protective layer of 4.9 μm that has been characterized in [60]. Because of this relatively thick protective layer, the MOIF is at a distance to the superconductor where it is not possible to resolve the stray field of individual vortices.

To obtain calibration data, the magneto-optic response of the MOIF was measured at 10 K, where the niobium film is in the normal state. The resonator was cooled to a temperature of 5.3 K in zero magnetic field and a reference image was acquired, before the magnetic field was increased. For the subsequent acquisitions, it is possible to convert the raw image data to magnetic field maps, by subtracting the reference image and rescaling the pixel values according to the calibration data that has been acquired at 10 K. This was done using the image processing software FIJI [98]. Fig. 3.13 (b) shows the magnetic field distribution at an externally applied magnetic field, with an orientation perpendicular to the substrate surface, of $B_\perp = 1.4\,\mathrm{mT}$.

[5] The author thanks D. Bothner and B. Ferdinand (Universität Tübingen) for providing the Nb resonator and M. Lindner (Innovent e.V. Jena) for providing the MOIF.

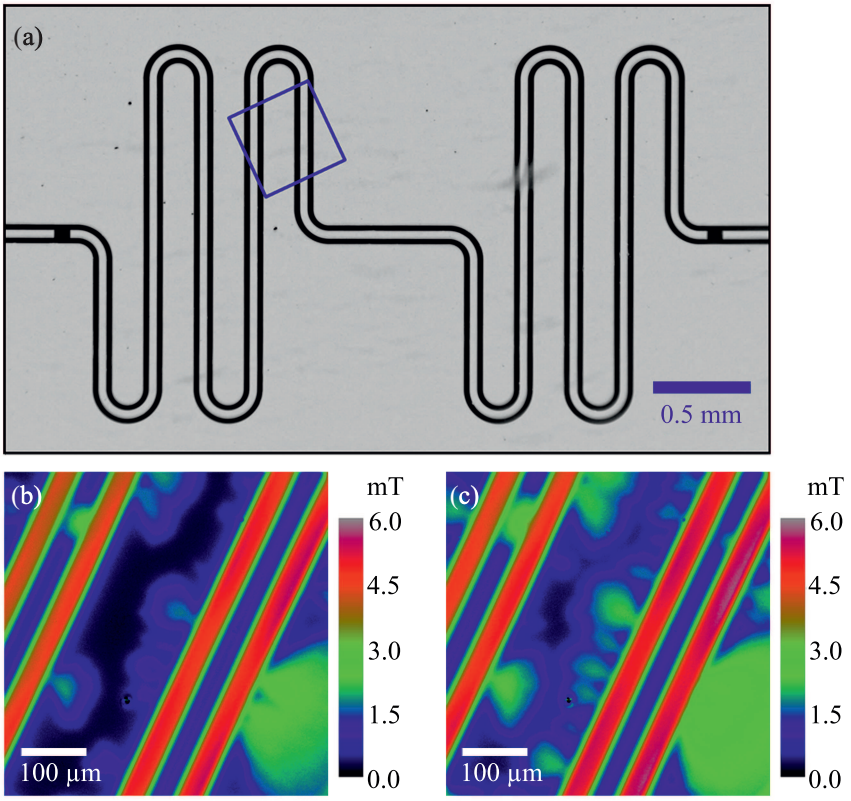

Figure 3.13: Imaging of magnetic flux in a superconducting niobium resonator. Optical image of a superconducting niobium half-wavelength resonator (a). The ground plane and center conductor appear bright, the gaps between them appear dark. The blue square indicates the area that has been imaged in (b) and (c) using a MOIF and the LTWPM. Magnetic field distribution above the resonator at an externally applied field of $B_\perp = 1.4\,\mathrm{mT}$ (b) and $B_\perp = 1.8\,\mathrm{mT}$ (c) at a temperature of 5.3 K. From [24].

The magnetic field is focused through the gap between the center conductor and the ground planes and magnetic flux in the form of Abrikosov vortices has entered the superconducting film. A few locations along the edge of the

Table 3.2: System specifications

	LTSPM	LTWPM
resolution	242 nm	481 nm
sensitivity	$5 \times 10^{-6}\,\mathrm{rad}/\sqrt{\mathrm{Hz}}$	$1.0 \times 10^{-4}\,\mathrm{rad}/\sqrt{\mathrm{Hz}}$
field of view	$500\,\mu\mathrm{m} \times 500\,\mu\mathrm{m}$	
temperature range	4 K to 300 K	
$B_{\parallel}$	± 800 mT	
$B_{\perp}$	± 20 mT	

niobium film are favored for flux entry, indicating a locally reduced surface barrier for flux penetration. The vortices that enter at these sites tend to get pinned at defects in the superconducting film. This results in a highly non-homogeneous distribution of Abrikosov vortices in the niobium film. As the magnetic field is increased to $B_{\perp} = 1.8\,\mathrm{mT}$ [Fig. 3.13 (c)] further flux entry sites appear and additional vortices enter the superconducting film. A comprehensive study of magnetic flux penetration in niobium thin films and the effect of indentations and roughness at the film border has been carried out by Brisbois *et al.* [118].

3.7 Summary

In summary, a versatile polarizing microscope that offers the possibility to image ferromagnetic, ferroelectric and ferroelastic domains by using either confocal laser scanning (LTSPM) or widefield microscopy (LTWPM) has been presented. Both imaging modes achieve excellent lateral resolution over a wide field of view. The lateral resolution of the LTSPM of 242 nm is close to the resolution limit for imaging with visible light. The instrument is equipped with highly sensitive polarized light detectors that provide a sensitivity of $1.0 \times 10^{-4}\,\mathrm{rad}/\sqrt{\mathrm{Hz}}$ for the LTWPM and $5 \times 10^{-6}\,\mathrm{rad}/\sqrt{\mathrm{Hz}}$ for the LTSPM. A ^{4}He continuous flow cryostat enables observations at sample temperatures ranging from 4 K to 300 K, and magnetic fields with variable orientation can be applied to the sample. The system specifications are summarized in table 3.2. The capability of the microscope to image ferromagnetic domains and domain walls in $BaFe_{12}O_{19}$ and the magnetic field distribution above a superconducting Nb film has been demonstrated.

It is expected that the instrument will prove to be useful for investigations of a wide variety of solid-state effects. The combination of magnetic, structural and electric imaging with high lateral resolution and variable temperature has the potential to deliver important insights e.g. for research in spintronics, spin-caloritronics, superconductivity, magnetism and their hybrid systems.

4 Twin Walls between Ferroelastic Domains in $SrTiO_3$ and their Effect on Electric Transport at the $SrTiO_3$/$LaAlO_3$ Interface [1]

4.1 Introduction

The emergence of novel effects in low-dimensional structures such as interfaces, grain boundaries, twin boundaries, and magnetic domain boundaries in bulk crystals, thin films or heterostructures of ferromagnetic, ferroelectric, ferroelastic, or superconducting materials is studied in the flourishing field of domain boundary engineering [120], that aims to achieve control of the functionality of domain boundaries at the nano-scale. Strontium titanate $SrTiO_3$ (STO) has attracted considerable interest in this regard. Although cubic at room temperature, STO undergoes a ferroelastic phase transition to a tetragonal crystal structure at around 105 K [121]. In its tetragonal phase,

[1] Parts of this chapter have been published in [119]. The LTSEM measurements have been performed by S. Scharinger, H.J. Harsan Ma and D. Kohlberger at the Universität Tübingen. Own contributions: For this publication, I conducted optical microscopy studies using the LTWPM that confirmed the presence of twin walls. Further details on these measurements are given in Sec. 4.4. Additionally, I prepared numerical simulations on the origin of the electron-beam induced voltage signal. Finally, I assisted in analyzing the data and contributed to the preparation of the publication [119].

STO shows pronounced twinning [122] and it has been shown by resonant ultrasonic spectroscopy [123], piezoelectric spectroscopy [124], and scanning stress microscopy [125] that the twin boundaries between tetragonal domains (twin walls) can be polar. However, due to zero-point fluctuations a macroscopic ferroelectric state in STO is not realized. Instead, STO becomes a quantum paraelectric at temperatures around 37 K [126–128]. Yet, signatures of electric-field induced ferroelectricity have been found [126, 129, 130] above a threshold field of 1.40 kV/cm at around 5 K. It has been suggested that the twin walls become ferroelectric at low temperatures [124, 131], which could be an explanation for the field-induced ferroelectricity.

STO is widely used as a substrate for the growth of thin films and usually considered as a homogeneous single crystal. However, this assumption holds not true in the low temperature tetragonal phase, where twinning produces a landscape of ferroelastic domains with twin walls at their boundaries. An example that is particularly sensitive to the influence of twin walls in STO is the conducting interface between $LaAlO_3$ (LAO) and STO: although both materials are insulating in bulk, the interface between a LAO-layer of at least four unit cells thickness and its TiO_2-terminated STO substrate becomes electrically conducting [132]. Several mechanisms leading to the formation of the two-dimensional electron gas (2DEG) at the LAO/STO interface are being discussed: First, the discontinuity between non-polar STO and polar LAO leads to electronic reconstruction at the interface [133–135]. The alternating layers of $La^{3+}O^{2-}$ and $Al^{3+}O_2^{4-}$ posses alternating charge. When grown on neutral TiO_2-terminated $SrTiO_3(001)$, this would lead to a diverging electric potential for increasing thickness of the LAO layer [Fig. 4.1 (a)]. This scenario is known as the 'polar catastrophe'. To avoid the polar catastrophe, half an electron per unit cell is transferred to the LAO/STO interface [Fig. 4.1 (c)]. In consequence, the electric potential no longer diverges and the excess charge at the interface leads to the formation of a 2DEG. Second, the interface could become conducting through the creation of oxygen vacancies during growth of the LAO film [136–138]. The third possible mechanism is intermixing of cations at the interface that leads to conducting $La_{1-x}Sr_xTiO_3$ [139]. In addition to the formation of a 2DEG, the LAO/STO interface has been shown to become superconducting [140, 141] below temperatures of approximately 200 mK and ferromagnetic [142–144].

Since it has been shown that the twin walls in the tetragonal phase of STO can be polar, it is straightforward to assume, within the elec-

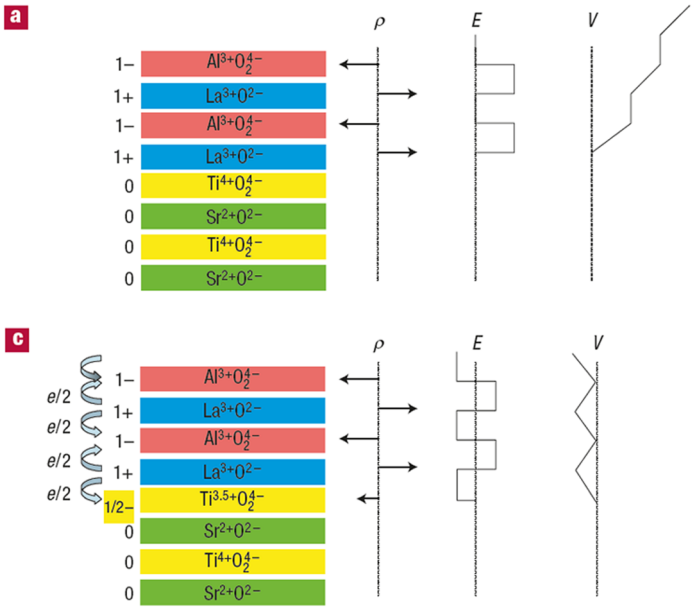

Figure 4.1: Electronic reconstruction at the interface between $LaAlO_3$ and TiO_2 terminated $SrTiO_3(001)$. (a) The $La^{3+}O^{2-}$ layers posses positive charge, while the $Al^{3+}O_2^{4-}$ layers have negative charge. Grown on the neutral $Ti^{4+}O_2^{4-}$ plane, this leads to a diverging electric potential (V). (c) By transferring half an electron per unit cell to the LAO/STO interface, the electric field is centered around zero and the potential no longer diverges. From [133].

tronic reconstruction scenario, that they will have a profound effect on the 2DEG at the LAO/STO interface. The influence of twin walls on the two-dimensional electron gas at the LAO/STO interface has been studied by scanning SQUID microscopy [145], scanning single-electron transistor microscopy [146], scanning stress microscopy [125], and LTSEM [119].

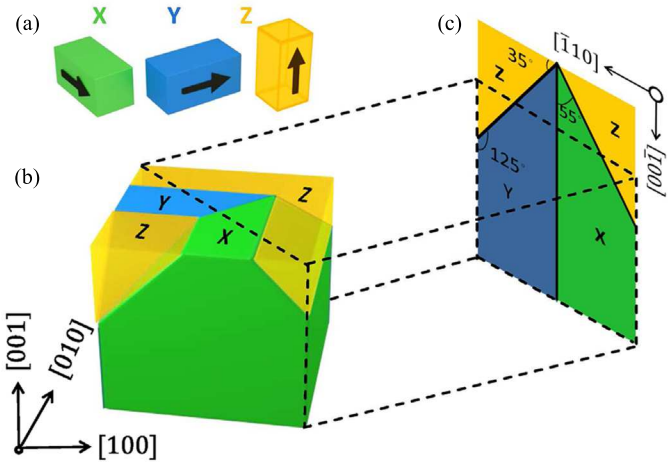

Figure 4.2: (a) Possible orientation of tetragonal twins in STO. Twin walls are possible where adjacent twins share an *a*-axis. Twin walls between X, Y, and Z domains in the (001)-plane (b) and in the (110)-plane (c). Modified from [119].

4.2 Configuration of twin walls in the tetragonal phase of $SrTiO_3$

At temperatures below the ferroelastic cubic to tetragonal phase transition in STO, twins with an orientation of the long axis (*c*-axis) of their tetragonal unit cell along the [100], [010], and [001]-direction of the cubic unit cell are possible and are labeled as X, Y, and Z, respectively in Fig. 4.2 (a). The orientation of twin walls between the different twin domains can be found by using the tiling rules of tetragonal domains [146]. Dislocations are minimized when two adjacent domains share an *a*-axis. The possible orientations of twin walls in the (001)-plane of the cubic crystal are shown in Fig. 4.2 (b), while Fig. 4.2 (c) shows the orientations in the (110)-plane of the cubic crystal. Twin walls with angles of 0°, 45°, and 90° relative to the [100]-axis are possible in the (001)-plane. In the (110)-plane twin walls can form at angles of 0°, 55°, and 125° with the [001]-axis or 35°, 90°, and 145° with the [$\bar{1}$10]-axis, respectively.

4.3 LTSEM imaging of tetragonal domains in $SrTiO_3$

Low-temperature scanning electron microscopy (LTSEM) is a method that can be used to map local electric transport properties of a sample (see Sec. 3.4). A periodically blanked electron beam is used to locally perturb the electric transport properties of the current-biased sample. This leads to a periodical voltage response with amplitude ΔV that can be measured using a lock-in amplifier. This voltage response serves as contrast for the LTSEM images.

The samples investigated in this study were prepared at the National University of Singapore by growing LAO thin films with a thickness of 5 to 20 unit cells on STO single crystal substrates with either (001) or (110) orientation. To achieve TiO_2-terminated surfaces, the STO(001) substrates have been treated with buffered HF for 30 s and annealed at 950°C for 1.5 hours in air, while the STO(110) have been annealed at 1050°C for 2.5 hours following the HF treatment. The LAO thin films were grown by pulsed laser deposition (PLD) at oxygen partial pressures from 2×10^{-4} to 2×10^{-3} Torr and a substrate temperature of 750°C. The LAO layer has been patterned into Hall bar microbridges with a size of $165\,\mu m \times 50\,\mu m$ using photolithography. The microbridges are oriented along the [100] or [010]-direction of the STO(001) substrate and along the [001] and $[1\bar{1}0]$-direction of the STO(110) substrate, respectively. For further information on sample preparation, see Refs. [147, 148].

Figure 4.3 shows LTSEM images of samples grown on STO(001) and STO(110) at a temperature of 5 K. Stripe-like patterns at different angles relative to the long side of the Hall bar can be seen in these samples. Samples No. 1 [Fig. 4.3 (a)] and No. 4 [Fig. 4.3 (b)] have been grown on STO(001) and show stripes at angles of 0 °, 45 °, and 90 °. These angles agree perfectly with the possible orientations of twin walls in the STO(001) surface (see Sec. 4.2). Samples No. 5a [Fig. 4.3 (c)] and No. 6a [Fig. 4.3 (d)] have been grown on STO(110). Here, stripes occur at angles of 55 ° and 125 °, which again agrees with the possible orientation of twin walls in the STO(110) surface. The observed stripe angles and expected orientations of twin walls for a number of different samples are summarized Table 4.1. The good agreement between the observed patterns and the expected orientation of twin walls indicates that the stripe-like patterns in the LTSEM images are indeed caused by twin walls.

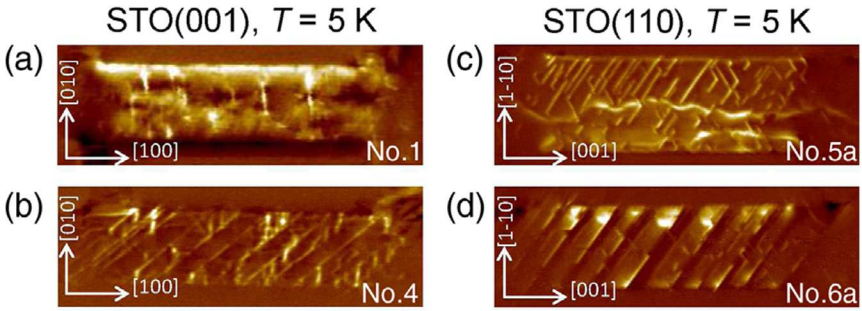

Figure 4.3: LTSEM images of different samples at 5 K. Twin walls are observed along different crystallographic axes and at different angles with respect to the long side of the 165 μm wide microbridge: (a) Along [010] (90 °) and [100] (0 °) in sample No. 1. (b) Along [010] (90 °) and [110] (45 °)in sample No. 4. (c) At angles of 55 ° and 125 ° in sample No. 5a. (d) At angles of 55 ° and 125 ° in sample No. 6a. The observed orientations of twin walls agree perfectly with the possible orientations (Sec. 4.2) for the STO(001) and STO(110) surfaces. From [119].

Table 4.1: Summary of device characteristics for samples grown on STO(001) and STO(110). The thickness of the LAO layer (in unit cells), as well as the expected and observed orientation of twin walls are given. The angles are measured relative to the long side of the Hall bar.

STO(001)			
		Pattern angles (deg)	
sample no.	LAO thickness [uc]	expected	observed
1	5	0, 90, 45, 135	0, 90, 135
2	20	0, 90, 45, 135	0, 90
3	5	0, 90, 45, 135	0, 90, 135
4	10	0, 90, 45, 135	0, 90, 45
STO(110)			
		Pattern angles (deg)	
sample no.	LAO thickness [uc]	expected	observed
5a	5	0, 55, 125	55, 125
5b	5	35, 90, 145	35, 90, 145
6a	10	0, 55, 125	55, 125
6b	10	35, 90, 145	35, 90, 145

Further evidence that the signal is generated at twin walls is shown in Figure 4.4, which displays LTSEM images measured on sample No.1 for increasing temperature. Stripe-like patterns along the [010]-direction can be observed. The contrast of these stripes decreases with increasing

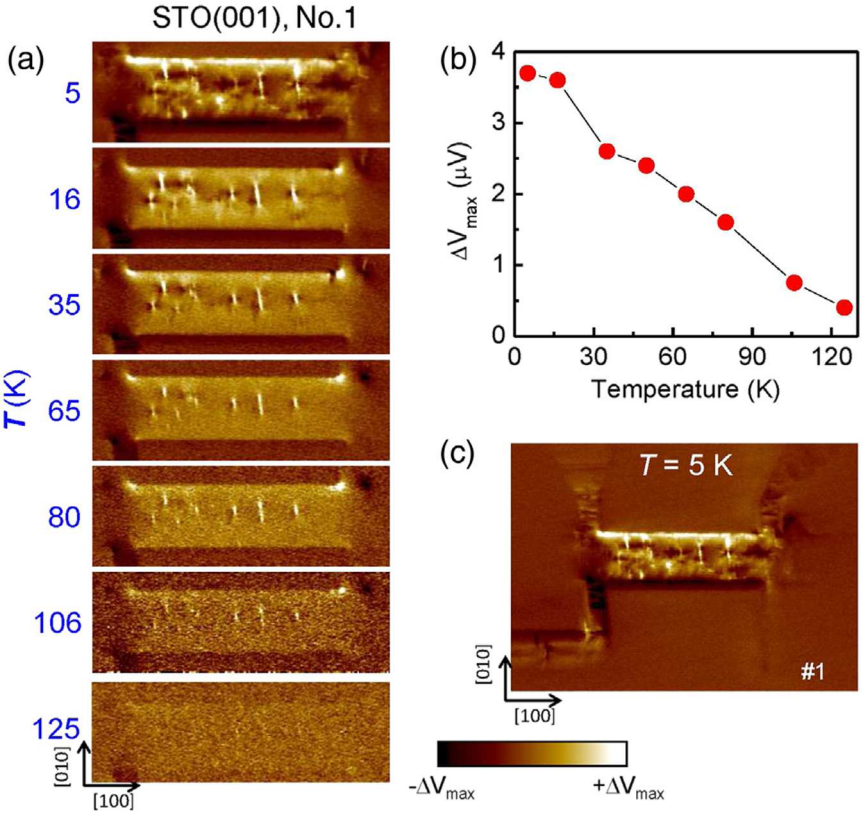

Figure 4.4: LTSEM images of sample No. 1 on STO(001) for different temperatures (a). The contrast decreases with increasing temperature (b). A LTSEM image including the electrodes (c) shows stripes that are oriented along the [100] and [010]-directions. The microbridge has a width of 165 μm. From [119].

temperature [Fig. 4.4 (b)] and approaches zero just above the cubic-to-tetragonal phase transition temperature of STO at 105 K. Additionally, the

configuration of the stripe-like patterns changes after thermal cycling to above 125 K, which supports the assumption that the patterns are related to twin walls. A larger part of the sample that includes the leads is shown in Fig. 4.4 (c). Here, stripes along both the [100] and [010]-direction can be seen. The mechanism leading to the contrast in LTSEM imaging is often due to local heating [86] and the voltage response ΔV is proportional to the temperature derivative $\mathrm{d}R/\mathrm{d}T$ of the resistance R. However, in this case both the resistance R and its derivative $\mathrm{d}R/\mathrm{d}T$ increase with T, while the contrast decreases. Therefore, local heating cannot be the origin of the observed signal and alternative mechanisms need to be considered. A possible explanation might be local charge carrier (holes and electrons) generation in STO by the electron beam. A fraction of these charge carriers diffuses to the LAO/STO interface where they get separated in the electric field along the current-biased Hall bar. Within this scenario, the increased signal at twin walls can be explained either by a higher charge carrier generation efficiency, an enhanced diffusion coefficient along the twin wall or a combination of both.

As the field of domain wall engineering aims at control over their functionality, the electric field response of twin walls in STO has been studied by applying an electric field via a side-gate or a back-gate electrode. The configuration of the side-gate measurement is shown in Fig. 4.5 (a). The electrode is at a distance of 165 μm to the Hall bar, so that the threshold field for the field-induced ferroelectricity [126] of 1.40 kV/cm is reached at a side-gate voltage of about 23 V. The back-gate electrode [Fig.4.5 (b)] is on the backside of the 500 μm thick STO substrate. Therefore, the threshold field is reached at a back-gate voltage of about 70 V. Fig. 4.5 (c) shows LTSEM images of sample No. 1 for side-gate voltages from 0 V to -200 V at a temperature of 5 K. With increasing negative gate voltage, a large number of stripes perpendicular to the long side of the Hall bar appear. Interestingly, the configuration that is established at a side-gate voltage of -200 V persists after the gate voltage is switched off. Moreover, it cannot be erased by thermal cycling the sample to temperatures below 100 K for a duration of 12 hours. However, after thermal cycling to 300 K most of the stripes disappear. Note, that the configuration after thermal cycling to 300 K closely resembles the configuration at a side-gate voltage of -20 V. A sequence of LTSEM images for back-gate voltages from 0 V to -210 V is shown in Fig. 4.5 (d). The behavior is similar to the side-gate measurement: more and more stripes appear upon increase of the negative gate voltage,

although due to the lower electric field at a given voltage not as many as in the side-gate measurement. Subsequent application of a positive back-gate voltage of 210 V did not change the configuration that was previously obtained at -210 V. The number of induced twin walls, shown in Fig. 4.6, scales

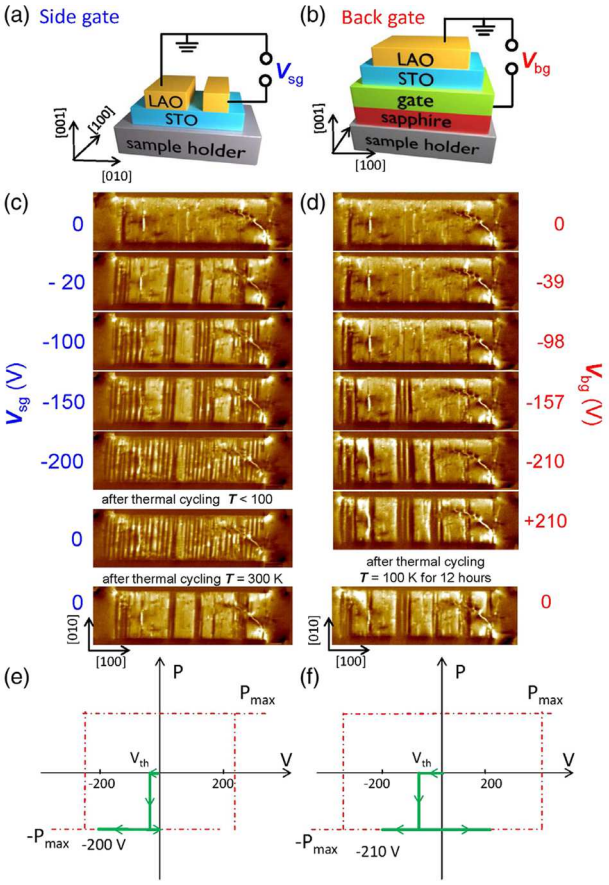

Figure 4.5: Electric-field response of twin walls in sample No. 1: (a) side-gate configuration, (b) back-gate configuration, (c) LTSEM images for different side-gate voltages V_{sg}, (d) LTSEM images for different back-gate voltages V_{bg}. The microbridge has a width of 165 μm. From [119].

linearly with the electric field for values above a threshold of $\sim 1.5\,\mathrm{kV/cm}$ that agrees well with values previously observed for electric-field induced order. The twin walls are believed to show ferroelectric order after exceeding the threshold field E_{th}. Still, a ferroelectric hysteresis loop that shows switching of the induced polarization and should manifest in a change in the twin wall configuration when the electric field is reversed has not been observed. This is probably due to the fact that the applied electric

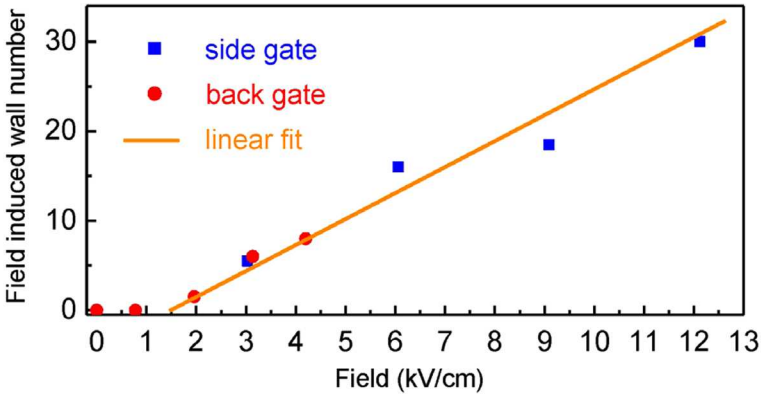

Figure 4.6: Number of electric-field induced twin walls as a function of the applied electric field. The number of twin walls increases linearly for fields above a threshold of $\sim 1.5\,\mathrm{kV/cm}$. From [119].

field (the maximum electric field reached is on the order of $10\,\mathrm{kV/cm}$) is below the coercive field for switching of the twin walls. This is schematically indicated in Fig. 4.5 (e) and (f) for the side-gate and back-gate configuration, respectively. Normally, a ferri-electric ordering of the dipole moments of a polar twin wall is expected. However, Zykova-Timan *et al.* [131] showed in simulations that the dipole moments form vortex-like structures that posses a component pointing in a direction perpendicular to the wall that is switchable and gives rise to ferroelectricity within the twin wall.

In summary, LTSEM imaging of twin walls between ferroelastic domains in tetragonal STO has been demonstrated. The twin walls are imaged by measuring their effect on the transport properties of the two-dimensional electron gas at the interface of the STO substrate and a LAO layer that has been deposited on top. Despite the fact that twin walls possess a width

($\sim 1\,\mathrm{nm}$) that is about three orders of magnitude below the resolution of the instrument, their influence on the transport properties is significant enough to obtain good contrast in the LTSEM images. The stripes that are seen in the LTSEM images appear at angles that perfectly match the possible orientations of twin walls. The stripes disappear above 105 K and form in a different configuration when the sample is repeatedly cooled to the tetragonal phase. Applying an electric field that exceeds a threshold of 1.5 kV/cm leads to the creation of stripes in the LTSEM images that are interpreted as a signature of electric-field induced ferroelectric order at the twin walls.

4.4 Optical imaging of twin walls

Imaging of twin walls in tetragonal STO is also possible by polarized light microscopy [26]. Birefringence in the STO substrate [149] leads to a contrast at the twin walls between adjacent ferroelastic domains.

Figure 4.7 shows an image series acquired with the LTWPM during cool-down of sample No. 5a that has been grown on STO(110). The orientation of the crystallographic axes and the possible orientation of twin walls is indicated in Fig. 4.7 L. The horizontal direction is the [001]-axis, the vertical direction the [$\bar{1}$10]-axis. At a temperature of 107 K (A), above the cubic to tetragonal transition, no ferroelastic twins or twin walls can be observed. After cooling to 100 K (B), faint lines at an angle of 55 ° and 125 ° with the [001]-axis are discernible. These are twin walls between ferroelastic domains of the STO crystal that formed at the cubic to tetragonal phase transition at 105 K. The twin walls become more readily visible when the temperature is further decreased. Two horizontal lines, at 0 ° with the [001]-axis, are visible at 85 K in addition to the slanted twin walls. The observed orientations perfectly match the expected angles (see Table 4.1 and Sec. 4.2). Although all the possible orientations are already present, the twin-wall (or ferroelastic domain) configuration continues to develop. In Fig. 4.7 D, acquired at 75 K, a bright line entering from the left side along the Hall bar can be seen. This line expands to the right and moves downwards in the image when the temperature is lowered to 50 K (E and F). Notice that another twin wall appeared close to the lower edge of the image and that now there are two parallel twin walls along the [001]-direction in the lower quarter of the image. As the temperature is reduced to 40 K (G),

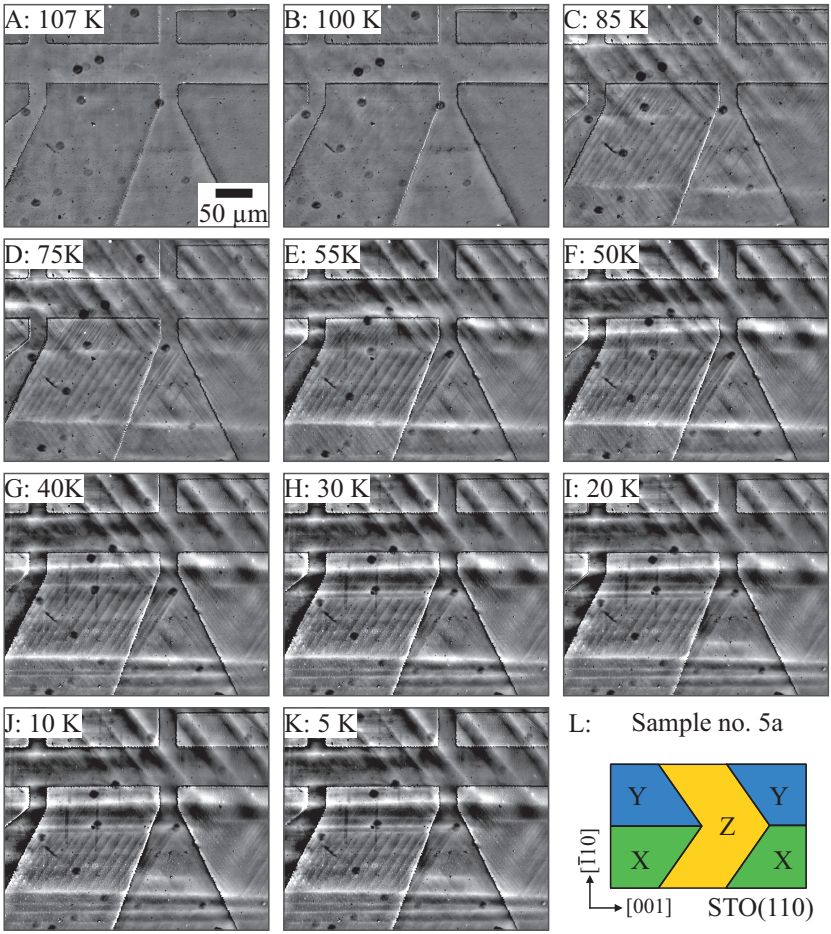

Figure 4.7: Temperature evolution of ferroelastic domains and twin walls in sample no. 5a, grown on STO(110). Panel L shows the orientation of the crystallographic axes and the possible orientations of twin walls between the ferroelastic X, Y, and Z domains.

a needle domain propagates from left to right in between these twin walls. Similarly, another needle domain along the [001]-direction can be observed in the center of image (H) at a temperature of 30 K. For lower temperatures, down to 5 K, the twin-wall configuration remains virtually unchanged (I-K). The twin walls with angles of 55 ° and 125 ° are formed at the X-Z and Y-Z domain boundaries, respectively, while the horizontal (0 °) twin walls are found at the boundary between X and Y domains.

An interesting observation is that twin walls between Y and Z or X and Z domains form with a high density (or narrow spacing) at the cubic to tetragonal phase transition and that their configuration remains almost unaffected by a change in temperature of 100 K. The twin walls between Y and X domains, on the other hand, are relatively scarce and widely spaced at temperatures near the cubic to tetragonal transition but become more frequent at lower temperatures, when e.g. a Y domain is split by the insertion of an additional X domain, as is the case for the needle domain observed along the lower edge of the images. Note that no twin walls between X and Y domains have been observed along the LAO microbridge. This might explain why it has not been possible to observe twin walls along the microbridge by LTSEM.

Figure 4.8 shows a comparison of the twin-wall configuration in sample No. 1 (a) and sample No. 5a (b) at a temperature of 10 K and a schematic representation of the possible orientations of twin walls in STO(001) (d) and STO(110) (e). Many twin walls at angles of 45 ° and 135 ° with the [100]-axis are readily visible in Fig. 4.8 (a). Apart from the large twin walls spanning almost the entire field of view, a lot of narrow spaced twin walls can be distinguished in between. However, twin walls at 0 ° and 90 ° are not apparent. Still, the zoom on the red rectangle in (a) that is shown in Fig. 4.8 (c), shows rectangular areas containing 45 ° and 135 ° twin walls that are surrounded by regions that are free of twin walls. The boundaries between these regions are highlighted by the dotted red lines. By comparing this with (d), the schematic representation of possible orientations of twin walls, it is discernible that the diagonal twin walls are boundaries between alternating X and Y domains, while the areas that appear to be free of twin walls have to be Z domains. Consequently, 0 ° and 90 ° twin walls have to be present but exhibit poor contrast. Figure 4.8 (b), shows the twin-wall configuration of sample no. 5a that has been grown on STO(110). Twin walls at angles of 0 °, 55 °, and 125 ° with the [001]-axis are visible, which corresponds exactly to the expected orientations (e). The images shown in

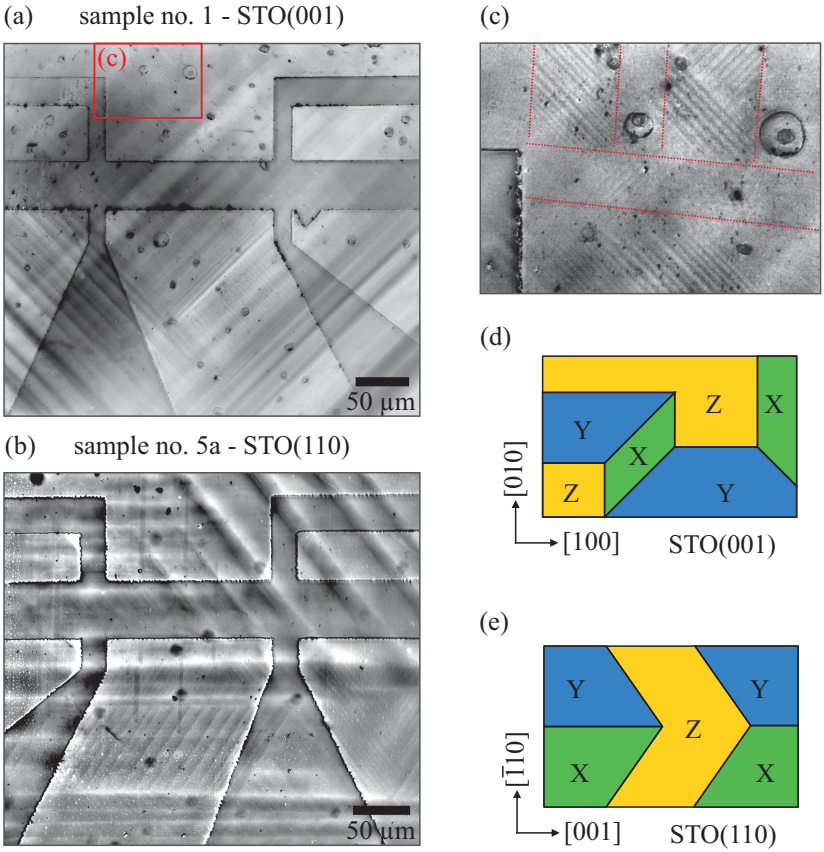

Figure 4.8: Twin-wall configuration in sample no. 1 (a) and sample no. 5a (b) at a temperature of 10 K. The possible orientations of twin walls between X, Y, and Z twins are schematically shown in (d) and (e) for STO(001) and STO(110), respectively. (c) shows a zoom on the part of sample no. 1 that is indicated by the red rectangle in (a). The red dotted lines in (c) highlight the boundaries between regions containing X and Y domains and regions that appear to be free of twin walls and are identified as Z domains.

Fig. 4.7 and Fig. 4.8 have been corrected for uneven illumination by using the 'subtract background' feature in FIJI [98].

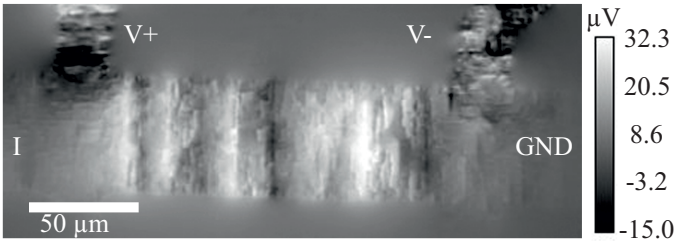

Figure 4.9: LTSLM ΔV image of a Nb/LAO/STO(001) Hall bar at a bias current of 11 μA and a temperature of 5 K.

The LTSPM offers the possibility to acquire ΔV images (Sec. 3.4). A LTSLM ΔV image of a Nb/LAO/STO(001) sample[2] (sample no. 2) at a temperature of 5 K is shown in Fig. 4.9. Since LAO and STO are highly transparent for visible light, a niobium layer has been added on top of the sample to absorb the laser beam, resulting in a local perturbation to the sample. A bias current of 11 μA was sent through the two-dimensional electron gas (from I to GND). The voltage response ΔV, due to the perturbation of the laser beam, was measured between V+ and V- using a lock-in amplifier operating at a reference frequency of 10 kHz and with a time constant of 1 ms. Twin walls in the STO substrate lead to a modification of the LTSLM response and are visible as stripe-like structures at an angle of 90 ° with the long side of the Hall bar in the LTSLM image. The ΔV image bears a strong resemblance to the images acquired with the LTSEM and confirms that the observed stripes are related to twin walls in the STO substrate.

[2]fabricated by A. Stöhr and H.J. Harsan Ma.

5 | Metal-Insulator Transition in V_2O_3 [1]

5.1 Introduction

Over the last decades, the strongly correlated vanadium sesquioxide (V_2O_3) has attracted extensive interest from both experimental and theoretical side due to the metal-insulator transition (MIT) it shows with doping, pressure, and temperature [151, 152]. Due to the good agreement between predictions from the Hubbard model and experimental data, V_2O_3 is commonly regarded as the prototypical Mott-Hubbard insulator that shows an electron localization that is caused by Coulomb repulsion [153, 154]. The phase diagram of V_2O_3 (Fig. 5.1) shows that, as a function of temperature, pressure, and doping with titanium or chromium, one of three distinct phases is realized. At room temperature and ambient pressure, stoichiometric V_2O_3 is a paramagnetic metal (PM) with corundum structure. An isostructural metal-insulator transition to a paramagnetic insulting phase (PI) is found for doping with Cr or a change in external pressure. Doping and pressure have been considered to have an equivalent influence [155] on the phase of V_2O_3 for a long time. However, this assumption has been

[1] This work was performed in collaboration with the group of Ivan K. Schuller at UCSD, San Diego. The measurements were performed by D. Schwebius as part of his master's thesis [150] (under my supervision) and by me. Own contributions: I performed part of the measurements. I analyzed the data, interpreted the results, and developed the numerical model. I especially thank Stefan Guénon for initiating the study and Yoav Kalchheim for providing the sample. I gratefully acknowledge fruitful discussions with Stefan Guénon, Yoav Kalcheim, Marcelo Rozenberg, Ivan K. Schuller, Reinhold Kleiner, and Dieter Koelle.

refuted, recently [156, 157]. At low temperatures, V_2O_3 is found in an antiferromagnetic insulating phase (AFI) with monoclinic structure. The transition between the PM and AFI phase occurs, for undoped V_2O_3 and at ambient pressure, at a temperature of about 150 K.

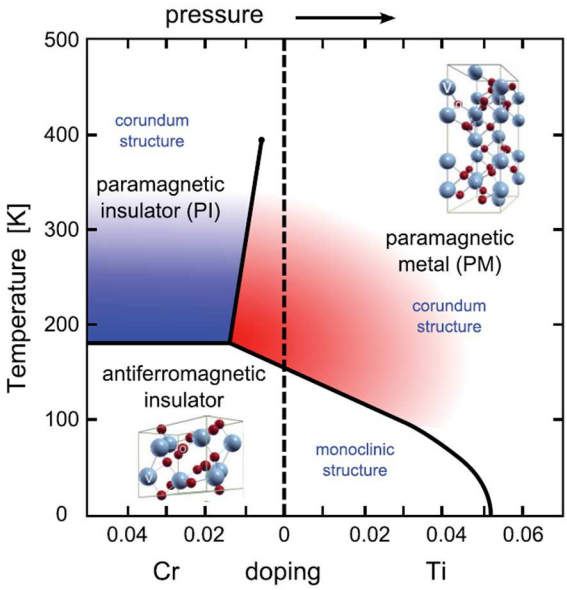

Figure 5.1: Phase diagram of vanadium sesquioxide. From [152].

The vanadium d states are split into lower lying t_{2g} and higher lying e_g^σ states by the crystal field. The trigonal distortion of the oxygen octahedra leads to a splitting of the t_{2g} into a single a_{1g} and a doubly degenerate e_g^π state [152, 158]. The two vanadium d-electrons occupy the lower lying t_{2g} states. The occupation of these states is different for the distinct phases of V_2O_3. The possible configurations are that both occupy the e_g^π state or that one electron is in the e_g^π and the other in the a_{1g} state. The ratio of these configurations $e_g^\pi e_g^\pi : e_g^\pi a_{1g}$ has been found to be 2:1 in the AFI phase, 1:1 in the PM phase, and 3:2 in the PI phase [159]. Each of the t_{2g} levels is again split into an upper and lower Hubbard band by the strong on-site Coulomb repulsion [160, 161]. The electronic density

of states is schematically represented in Fig. 5.2 for the AFI and PM phase. The density of states in the AFI phase is based on local-density

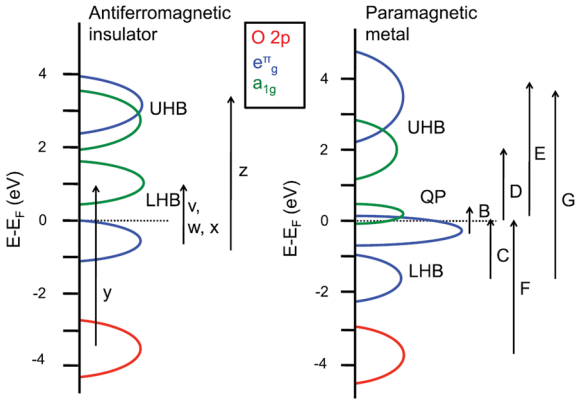

Figure 5.2: Density of states in the antiferromagnetic insulating phase (left) and the paramagnetic metallic phase (right). Upper (UHB) and lower (LHB) Hubbard bands for the e_g^{π} and a_{1g} levels, as well as oxygen $2p$ bands approximately 4 eV below the Fermi energy E_F. Additional quasiparticle peaks (QP) emerge in the PM phase. From [161].

approximation calculations incorporating an effective Hubbard potential (LDA+U) [162], while the density of states in the PM phase is obtained from LDA+DMFT calculations [160]. In the AFI phase, an energy gap of ≈ 0.5 eV is present between the e_g^{π} and a_{1g} lower Hubbard bands, which is a typical result for the band gap for both theoretical calculations and spectroscopic measurements [163, 164]. For the PM phase, two quasiparticle peaks (for e_g^{π} and a_{1g}) emerge at the Fermi level [160].

Due to the strong coupling between electronic and lattice degrees of freedom in correlated oxides, V_2O_3 thin films grown on different substrates show a strong influence of the deposition conditions on the metal-insulator transition [165–169]. This is attributed to the strain incorporated through the lattice mismatch between substrate and film. Compressive strain along the c-axis (or tensile strain along the a-axis) leads to a shift of the metal-insulator transition to higher temperatures [165, 166, 168, 169], whereas tensile strain along the c-axis (compressive strain along the a-axis) leads

to a decrease in metal-insulator transition temperature or even metallic behavior down to temperatures of 2 K [168]. The strain is often expressed in the c/a-ratio of the lattice parameters of the films. For bulk V_2O_3 the lattice parameters are $c = 14.00083$ Å and $a = 4.9540$ Å resulting in a ratio of $c/a = 2.826$. It has been shown that a c/a-ratio slightly below the bulk value can be realized for V_2O_3 films grown on r-cut sapphire and that these films exhibit a metal-insulator transition at slightly elevated temperatures [165]. The structural phase transition from the corundum to the monoclinic structure in bulk V_2O_3 goes along with a reduction of c and an increase of a [155]. Therefore, a reduced c/a-ratio due to strain assists the metal-insulator transition and leads to higher transition temperatures. Consequently, growing V_2O_3 on substrates where either the c-axis or a-axis is rigidly clamped hinders the corundum-monoclinic transition, and with it the metal-insulator transition. On the other hand, V_2O_3 films showing an insulator-metal transition with a resistance change over several orders of magnitude can be obtained on r-cut sapphire substrates that allow for a change in c/a-ratio [165].

Phase separation in strongly correlated electron systems has been theoretically predicted from mean-field theory [170], dynamical cluster approximation in the Hubbard model [171], and thermodynamics [172]. Experimentally, a separation of the metallic and insulating phase at the metal-insulator transition in a 300 nm thick V_2O_3 film, grown on r-cut sapphire, has been found by McLeod *et al.* [173] using scanning near-field infrared microscopy. In their study they show that the metal-insulator transition progresses from a homogeneous metallic state to a homogeneous insulating state through two intermediate stages, the first of which is characterized by percolative paths formed by metallic and insulating domains whereas the second stage is characterized by metallic islands in a insulating matrix. This self-organized phase coexistence is attributed to competing short- and long-range interactions [174]. Moreover, through complementary X-ray diffraction measurements, they show that the metal-insulator transition is decoupled from the structural phase transition between the corundum and the monoclinic phase and that metallic domains persist in the monoclinic phase. They conclude that the striped domain configuration at the metal-insulator transition is caused by elastic long-range interactions [175, 176] that are produced by the lattice mismatch of the corundum and monoclinic phase with the substrate. A similar nano-scale phase separation has also been found in strained VO_2 films [177]. Although a sharp transition between the metallic

and insulating phase is forbidden due to the long-range interaction [178], McLeod *et al.* found that the near-field infrared signal locally shows a jump at the metal-insulator transition temperature, indicating a first-order phase transition, which is in agreement with dynamical mean-field theory treatments of the Hubbard model [151, 153, 179]. However, the near-field infrared signal does not show a transition between two discrete levels for the insulating and metallic phase but a gradual increase when approaching the insulator-metal transition, which they attribute to a narrowing of the insulating bandgap.

At temperatures close to the insulator-metal transition, V_2O_3 can be driven from the insulating phase to the metallic phase by applying a large enough bias current. This electrically driven breakdown of the insulating phase, that is also observed in other strongly correlated materials exhibiting a metal-insulator transition, is under extensive investigation as it bears potential for novel electronic devices [180], memristive devices [181, 182], electro-optical elements [183], and as a possible building block for neuromorphic computing [184–186]. Whether the electrical breakdown is driven by electric field, as has been theoretically proposed from DMFT calculations [187–191], or if it occurs due to the formation of electro-thermal domains [192–198] is in the focus of recent research. The breakdown has been shown to occur through the development of current filaments, which have been imaged using optical microscopy in VO_2 [196–199] and LTSEM in V_2O_3 [194]. Although optical microscopy is a tool well suited to investigate metal-insulator transitions, optical imaging of current filaments in V_2O_3 has not been reported.

This chapter is structured as follows: Imaging of the phase separation at the metal-insulator transition using the low-temperature widefield microscope is covered in Sec. 5.2, a detailed study of the electrical breakdown of the insulating phase is presented in Sec. 5.3, a numerical model reproducing the breakdown characteristics is described in Sec. 5.4. The results are summarized and discussed in Sec. 5.5.

5.2 Phase separation at the metal-insulator transition

Here, the phase coexistence in V_2O_3 is studied by low-temperature widefield microscopy (see Sec. 3.2). A microscope image of the sample investigated in this study is shown in Fig. 5.3 (a). All the data shown hereafter have

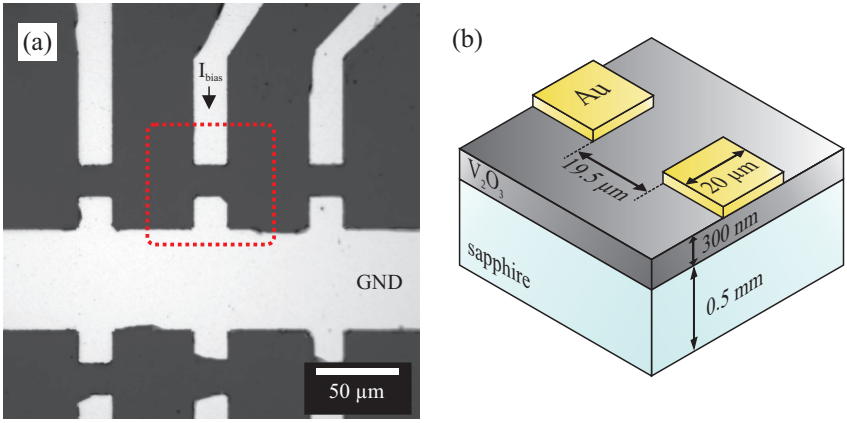

Figure 5.3: Layout of the V_2O_3 sample: (a) Microscope image of the sample. The device under investigation is highlighted by the red rectangle. The bias current is sent into the upper electrode. The wide horizontal electrode is at ground. (b) Schematic view of the sample: The gold electrodes are deposited onto a pristine 300 nm thick V_2O_3 film, grown on a r-cut sapphire substrate.

been measured on the device that is highlighted by the red rectangle. Figure 5.3 (b) shows a schematic drawing of the sample and its dimensions. Gold electrodes with a spacing of $\approx$ 19.5 μm and a width of $\approx$ 20 μm have been patterned on top of the 300 nm thick continuous V_2O_3 film, which has been grown by rf-sputtering on a r-cut sapphire substrate at UC San Diego. The V_2O_3 film has not been patterned to avoid potential defects or alterations to the electrical behavior that could be caused by ion irradiation. For imaging of the sample, the widefield microscope is used with parallel orientation of polarizer and analyzer, and consequently the intensity reflected by the sample is recorded. In contrast to the study by McLeod *et al.*, the samples resistance is measured concomitantly with the microscopic images, allowing a direct correlation of domain configuration and global resistance. The electric transport measurement is conducted using a *Keithley 2400 source/meter unit* configured as a current source. In addition to the global resistance measurement, a numerical model, which is described in detail in Sec. 5.4, gives access to the temperature dependence of the insulating phase that, in global measurements, is masked by the

coexistence of metallic and insulating phase at temperatures close to the transition temperature.

Figure 5.4 (a) shows the resistance as a function of temperature [$R(T)$] for cool-down and warm-up of the sample. The resistance was measured by applying a bias current of 5 μA to the sample while cooling from room temperature to 80 K and, subsequently, heating back to room temperature. The sample shows a five-order-of-magnitude increase in resistance across the metal-insulator transition. It is noteworthy that the metal-insulator transition of the V_2O_3 film is amongst the sharpest observed so far. A distinction is made between the cooling branch henceforth referred to as metal-insulator transition (MIT) and the heating branch referred to as insulator-metal transition (IMT). A thermal hysteresis of approximately 5 K between the MIT and IMT is apparent. Figure 5.4 (b) shows a series of images acquired during the $R(T)$ measurement. The images are labeled with letters from A to T and the temperature at which the image has been recorded. The corresponding point in the $R(T)$ curve in Fig. 5.4 (a) is indicated by a red cross with label A to T. Close-up views of the area between the electrodes are presented and the contrast has been adjusted to show the V_2O_3 film. Therefore, the electrodes appear overexposed (white). A first obvious observation is that the contrast of the V_2O_3 film changes from dark (lower reflectivity) in the metallic phase to bright (higher reflectivity) in the insulating phase. Note that this is in contrast to the intuitive expectation that the metallic phase would exhibit a higher reflectivity compared to the insulating phase. The reason for this behavior will be discussed on page 88. The transition between the two phases progresses through the formation of domain patterns with dark and bright contrast that are identified as metallic and insulating regions, respectively. Starting from a homogeneous metallic state (A: 176 K), small insulating islands begin to form (B: 170 K) that grow and connect to form a herringbone-like domain pattern (C: 168 K and D: 166 K). At this point, the metallic domains still provide continuous paths connecting the electrodes. These get disconnected when the temperature is further decreased (E: 164 K and F: 162 K) which goes along with a steep increase in resistance, as the current now has to flow through parts of the film that are in the insulating phase. This is henceforth referred to as the percolation temperature $T_{\mathrm{MIT}}^{\mathrm{perc}} \approx 162\,\mathrm{K}$. At even lower temperatures (G: 161 K, H: 160 K, and I: 158 K) the V_2O_3 film is in a state where metallic patches are embedded within an insulating matrix. The size of the metallic domains decreases with decreasing temperature until the sample is in a

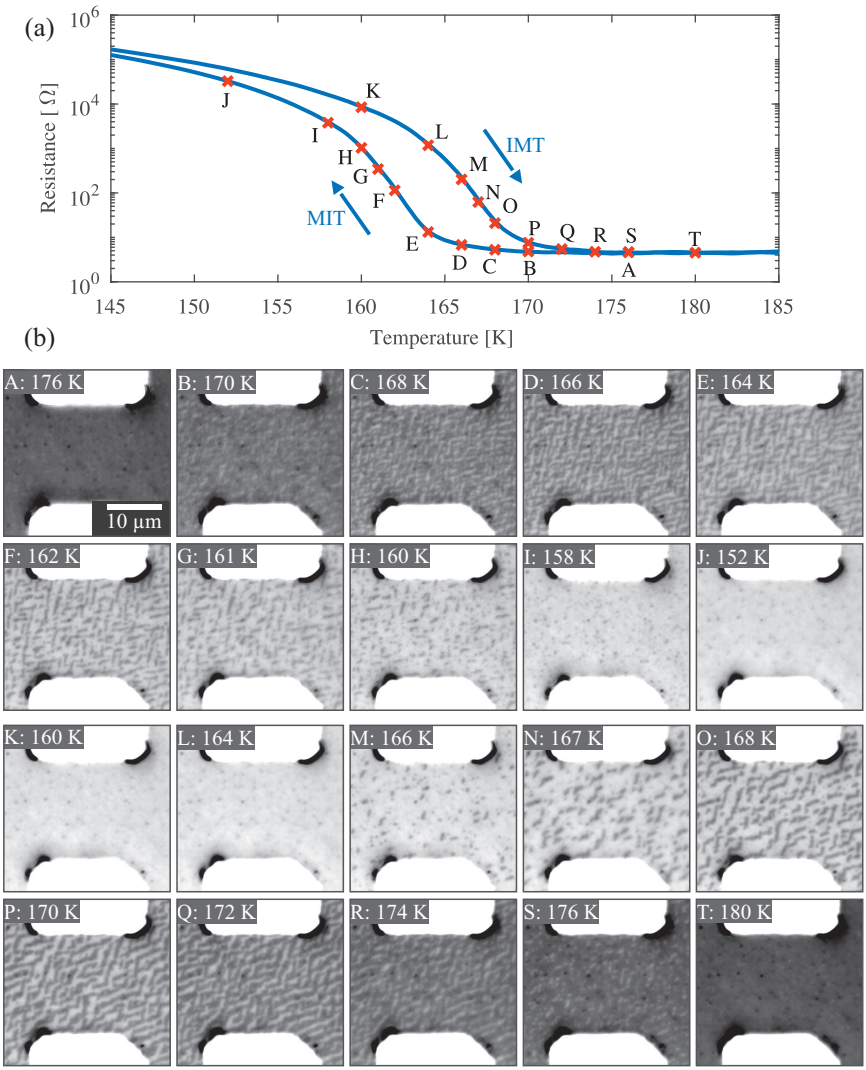

Figure 5.4: Phase separation in V_2O_3 at the metal-insulator transition: (a) $R(T)$ curve showing a five-order of magnitude increase of the resistance across the metal-insulator transition (MIT). A thermal hysteresis of approximately 4.5 K is present between the cooling (MIT) and the heating branch (IMT). (b) Images acquired at the points, labeled A to T in (a), during cool-down and warm-up of the sample.

homogeneous insulating state (J: 152 K). The heating branch shows a slightly different behavior. Beginning from the homogeneous insulating state (K: 160 K), small metallic islands appear (L: 164 K and M: 166 K) that connect to elongated domains (N: 167 K and O: 168 K). These domains are wider than the domains in the cooling branch and have a different preferred direction. Upon further increase of the temperature, more metallic domains appear and long metallic paths are created that eventually form continuous metallic paths that connect the electrodes (P: 170 K). The percolation temperature is estimated to be around $T_{\mathrm{IMT}}^{\mathrm{perc}} \approx 169\,\mathrm{K}$. The metallic regions grow (Q: 172 K and R: 174 K) until only isolated insulating patches are left (S: 176 K). Eventually the film arrives in a homogeneous metallic state (T: 180 K).

The preferred direction of the domains and their periodicity can be estimated from the fast Fourier transform (FFT) of the images, which are shown for selected temperatures, together with corresponding optical images, in Fig. 5.5. The FFT of the domain configuration in the MIT [Fig. 5.5 (a) and (b)] clearly shows four peaks that correspond to directions of $\approx 101\,^\circ$ and $\approx 171\,^\circ$, measured counter-clockwise with respect to the horizontal axis, with a mean periodicity of $\approx 1.3\,\mu$m at 166 K and $\approx 1.5\,\mu$m at 162 K. The preferred orientations of the long axis of the domains in real space are perpendicular to the directions found in the FFT and are indicated by the broken lines at $\approx 11\,^\circ$ and $\approx 81\,^\circ$ in the images. Figure 5.5 (c) and (d) show the domain configuration and FFT for temperatures of 168 K and 172 K in the IMT. Here, it is not possible to distinguish the peaks of the $101\,^\circ$ and $171\,^\circ$-axes in the FFT. However, the real space image at 168 K shows that a lot of the domains still are oriented along the $11\,^\circ$ and $81\,^\circ$-axes, while some domains have an orientation that lies in between these axes. At 172 K, on the other hand, only few domains are oriented along the $81\,^\circ$-axis, and the preferred directions become $11\,^\circ$ and $68\,^\circ$, which is observed in the FFT as a narrowing of the peaks in angular direction. The mean periodicity of the domains in the heating branch (IMT) is found to be $\approx 2.2\,\mu$m at 168 K and $\approx 1.8\,\mu$m at 172 K.

Figure 5.6 (a) and (b) show the domain configuration at 168 K in the heating branch for two subsequent measurement runs. A complete thermal cycle (heating to room temperature and cooling to 80 K) separates the two images. While the overall density of metallic domains is similar, the domain patterns differ significantly. For comparison, a color-coded overlay is shown in Fig. 5.6 (c). Metallic domains that are present in both (a) and (b),

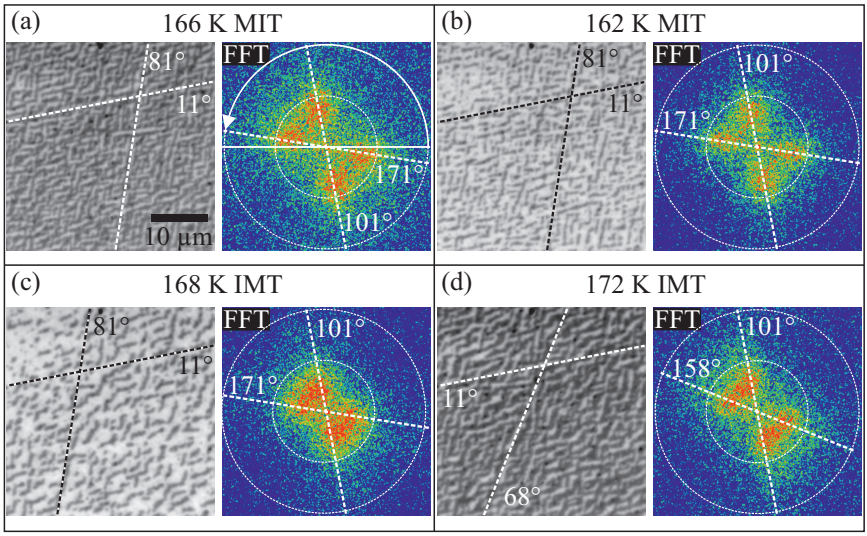

Figure 5.5: Domain configuration (left) and fast Fourier transform (right) for selected temperatures of (a) 166 K and (b) 162 K in the cooling branch (MIT) and (c) 168 K and (d) 172 K in the heating branch (IMT). The dashed lines highlight the predominant directionality of the long axis of domains in the real-space images and the directions at which the peaks occur in the FFT. The angles are measured counter-clockwise with respect to the horizontal axis. The inner circle in the FFT corresponds to a spatial frequency of $1/\mu$m, the outer circle to a spatial frequency of $2/\mu$m.

appear dark. Domains that are present only in image (a) are represented in green, those that are only present in (b) in red. It is apparent, that the domain configuration for repeated measurements is neither deterministic nor random. The same holds true for other temperatures in both the MIT and IMT. This indicates that the phase separation is not due to growth-induced local inhomogeneities of the film, for example in chemical composition, that lead to a spatially varying transition temperature but rather is caused through minimization of local strain as proposed by McLeod *et al.* [173]. As a consequence of strong lattice-electron interactions, strain has also been determined to play an important role for the phase separation at the metal-insulator transition in VO_2 films [177, 200] and nanostructures [201].

Domain patterns, bearing a strong resemblance to those observed here, can be found by numerical approximations to the Cahn-Larché equation, which describes the phase separation of a binary mixture in the presence of elastic stress [202].

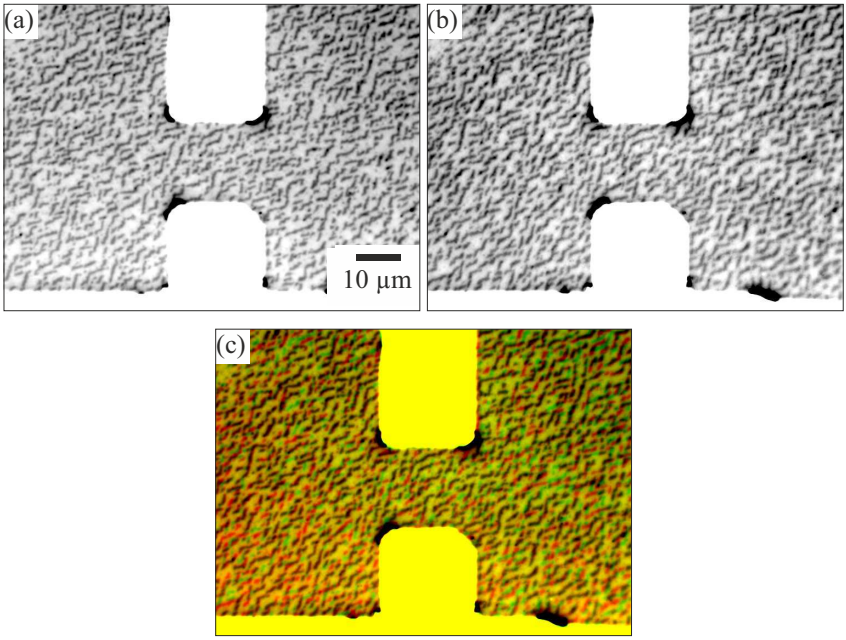

Figure 5.6: Repeatability of domain configuration. (a) and (b) show the domain configuration at 168 K in the heating branch for two subsequent runs with a full thermal cycle in between. A color-coded overlay to highlight the differences is depicted in (c). Metallic domains that are present in both (a) and (b) appear dark. Domains that are present only in (a) are shown in green. Domains that are present only in (b) are shown in red. The domain configuration is neither random nor deterministic.

The evolution of reflectivity with temperature for the global reflectivity, obtained by averaging over the field of view, and the local reflectivity evaluated from data of a single pixel, are shown in Fig. 5.7. The reflectivity has been normalized to the reflectivity of the gold electrodes. The global

reflectivity shows a smooth transition from lower reflectivity in the metallic phase to higher reflectivity in the insulating phase with a contrast around 15 %. Note that the contrast is reversed in comparison with the findings of McLeod *et al.*, where, as one would intuitively expect, the reflectivity was higher in the metallic state. However, they have been imaging at a

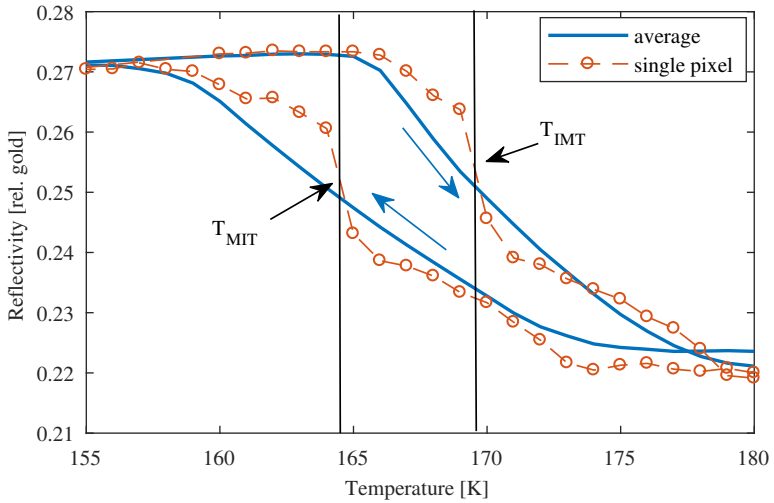

Figure 5.7: Reflectivity of the V_2O_3 film, normalized to the reflectivity of the gold electrodes, averaged over the field of view (solid blue line) and for a single pixel (broken red line) as a function of temperature.

much longer wavelength of 10 μm (0.124 eV), whereas here a wavelength of 532 nm (2.33 eV) is used. Spectral measurements of V_2O_3 in the metallic and insulating phase [161] show that for energies above 1 eV the optical conductivity in the insulating phase is higher than in the metallic phase and that the Drude plasma frequency ω_p drops from around 1.2 eV to nearly 0 eV when going from the metallic to the insulating phase. Therefore, McLeod *et al.* have been probing the reflectivity below ω_p in the metallic phase and above ω_p in the insulating phase and observed a transition from high to low reflectivity, respectively. Here, the probing energy is above the plasma frequency ω_p regardless of phase, and the contrast between the metallic and insulating phase can be attributed to interband transitions between the e_g^π

and a_{1g} lower Hubbard bands in the insulating state and transitions from the quasiparticle peak [160, 203] to the a_{1g} upper Hubbard band (cf. [161] and Fig. 5.2) in the metallic state.

The local reflectivity curves show a jump, as would be expected for a first-order phase transition, at what is defined as the *local* metal-insulator transition temperature T_{MIT} and the *local* insulator-metal transition temperature T_{IMT}. However, the local reflectivity does not switch between two discrete levels for the insulating and metallic phase but shows a gradual change for temperatures approaching the local transition temperature. A similar behavior has been observed by McLeod *et al.* [173] and is attributed to a narrowing of the band gap.

By analyzing the single-pixel reflectivity curves, it is possible to evaluate the local transition temperatures of the V_2O_3 film. Figure 5.8 (a) shows a map of the metal-insulator transition temperature $T_{\mathrm{MIT}}(x, y)$, the corresponding insulator-metal transition temperature map $T_{\mathrm{IMT}}(x, y)$ is shown in Fig. 5.8 (b). The maps show a quite heterogeneous spatial distribution of patches with different transition temperature, where the transition temperature within one patch is the same. The shape and size of individual patches resembles very much the shape of the domains shown in Fig. 5.4. Histograms of the local transition temperatures, shown in Fig. 5.9, reveal that for both the IMT and the MIT, the transition is quite abrupt towards low temperatures, whereas it is more gradual towards high temperatures. The mean transition temperatures are found to be $\bar{T}_{\mathrm{IMT}} = 169.6\,\mathrm{K}$ and $\bar{T}_{\mathrm{MIT}} = 164.3\,\mathrm{K}$, while the modal transition temperatures are $\tilde{T}_{\mathrm{IMT}} = 168\,\mathrm{K}$ and $\tilde{T}_{\mathrm{MIT}} = 162\,\mathrm{K}$. The modal values of the transition temperature correlate well with the percolation temperatures and the points of the largest change in resistance.

Comparing the $R(T)$ curve [Fig. 5.4 (a)] with the corresponding images [Fig. 5.4 (b)] and the temperature profile of the global reflectivity (Fig. 5.7) reveals that the resistance shows hysteresis for temperatures below 152 K where the images of the sample indicate a homogeneous insulating state with equal reflectivity for both the cooling and heating branch. Although the metal-insulator transition in V_2O_3 is a first-order phase transition, this suggests that the resistivity shows an gradual increase from the metallic phase to the insulating phase (and vice versa) over a finite temperature interval. Due to the phase mixture at the MIT the temperature-dependent resistivity of the insulating phase is not readily accessible from global resistance measurements, unless the device is scaled down to the size of

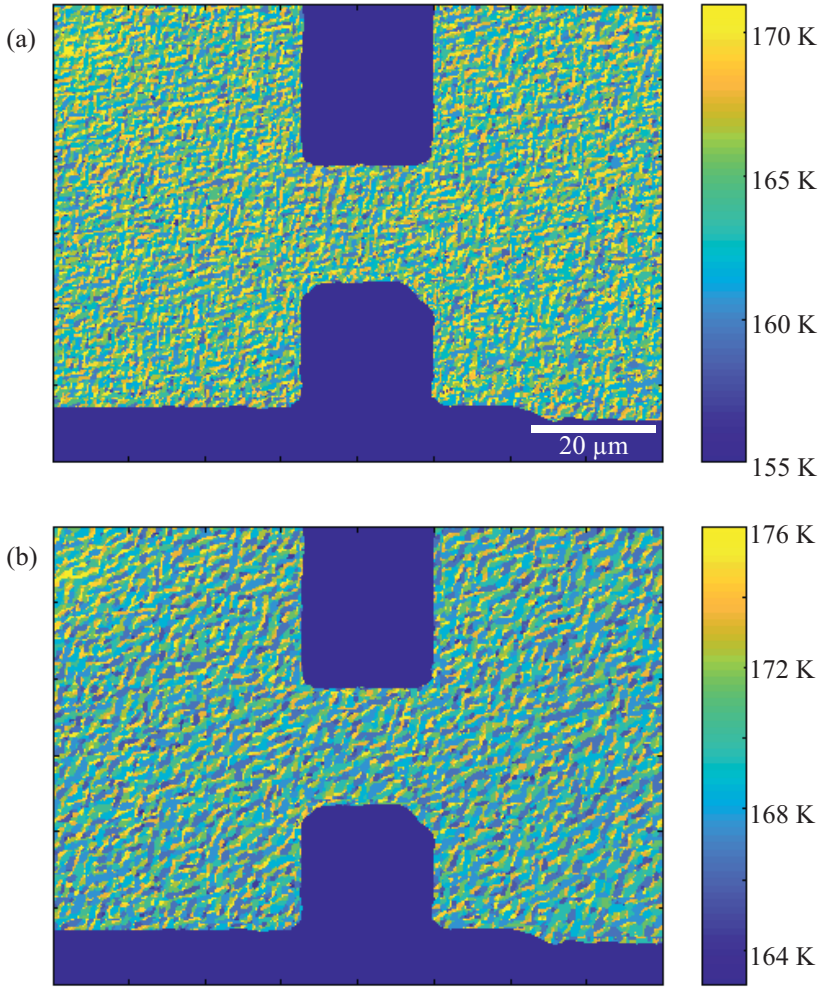

Figure 5.8: Local transition temperatures (a) T_{MIT} for the metal-insulator transition, (b) T_{IMT} for the insulator-metal transition.

a single domain. However, since the domain configuration and resistance have been measured concomitantly, it is possible to assign a temperature

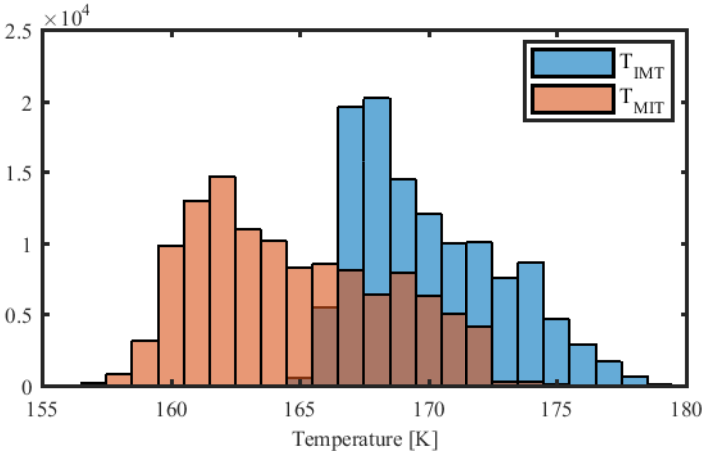

Figure 5.9: Histogram of the local transition temperatures T_{IMT} and T_{MIT}.

dependence to the transition region that reproduces the globally measured $R(T)$ by taking into account the spatial distribution of the insulating and metallic phase. This is done using the model presented in Sec. 5.4.

In conclusion, imaging of the phase separation at the metal-insulator transition of undoped V_2O_3 has been accomplished by using low-temperature widefield microscopy for the first time. Overall, the results obtained here are in excellent agreement with the findings of McLeod *et al.* [173]. The phase separation and appearance of domains at the metal-insulator transition is likely going to influence the breakdown characteristics of the device that will be addressed in the ensuing chapter.

5.3 Electrical breakdown

Here, imaging of current filamentation in V_2O_3 using low-temperature widefield microscopy is demonstrated for the first time. The data suggests that the cause for the electrical breakdown is the formation of electrothermal domains caused by Joule heating and self-reinforced focusing of the current due to the negative temperature coefficient $\partial\rho/\partial T$ of the resistivity ρ of V_2O_3.

The electrical breakdown of the insulating phase was studied for temperatures from 157 K to 169 K by measuring the current-voltage characteristic (IV) and simultaneously recording the reflectivity of the device with the widefield microscope. Several consecutive IVs have been acquired at each temperature. Before the recording of each set of IVs, the sample was brought into a defined initial state by thermal cycling, i.e. heating to room temperature followed by cooling to 80 K. The IVs were obtained in a current-biased measurement by ramping the current from 0 mA to 20 mA and back and measuring the voltage in a 2-point configuration.

5.3.1 Electrical breakdown at 158 K

Figure 5.10 (b) shows the first IV measured at a temperature of 158 K. The images corresponding to the points, labeled A to R, are shown in Fig. 5.10 (a). The IV starts at zero bias current. After warming from 80 K, the complete sample is in the insulating state at 158 K (A). When the current is increased, the IV soon starts to deviate from ohmic behavior indicating a decrease in resistance. This can be interpreted as an increase in temperature through Joule heating which leads to a decrease in resistance due to the negative temperature coefficient of the resistivity. The IV even shows a back bending, i.e. a reduction of voltage for increasing current, until it arrives at point B. Note that the image at (B) shows no change compared to (A) and the sample is still completely in the insulating state. However, further increase in current leads to a discontinuous jump to lower voltages that goes along with the formation of continuous metallic filaments connecting the electrodes (C) and the creation of disconnected metallic domains around the device. Whether this breakdown can be explained by Joule heating or is driven by electric field is at the center of this study. As the current is ramped up, most of the metallic domains around the device disappear (D). A pertinent observation is that the voltage remains pretty constant with increasing current after the breakdown (C-I), which implies that the resistance is proportional to the inverse of the current $R \propto 1/I$. Looking at images C-I, the reason for this voltage regulation becomes obvious: the filaments grow in width for increasing current with a width that has to be approximately proportional to the bias current. Once it is formed, the filament can be understood as an electro-thermal domain. The current is confined to the filament and heats it above the insulator-metal-transition temperature. When the current is increased, Joule

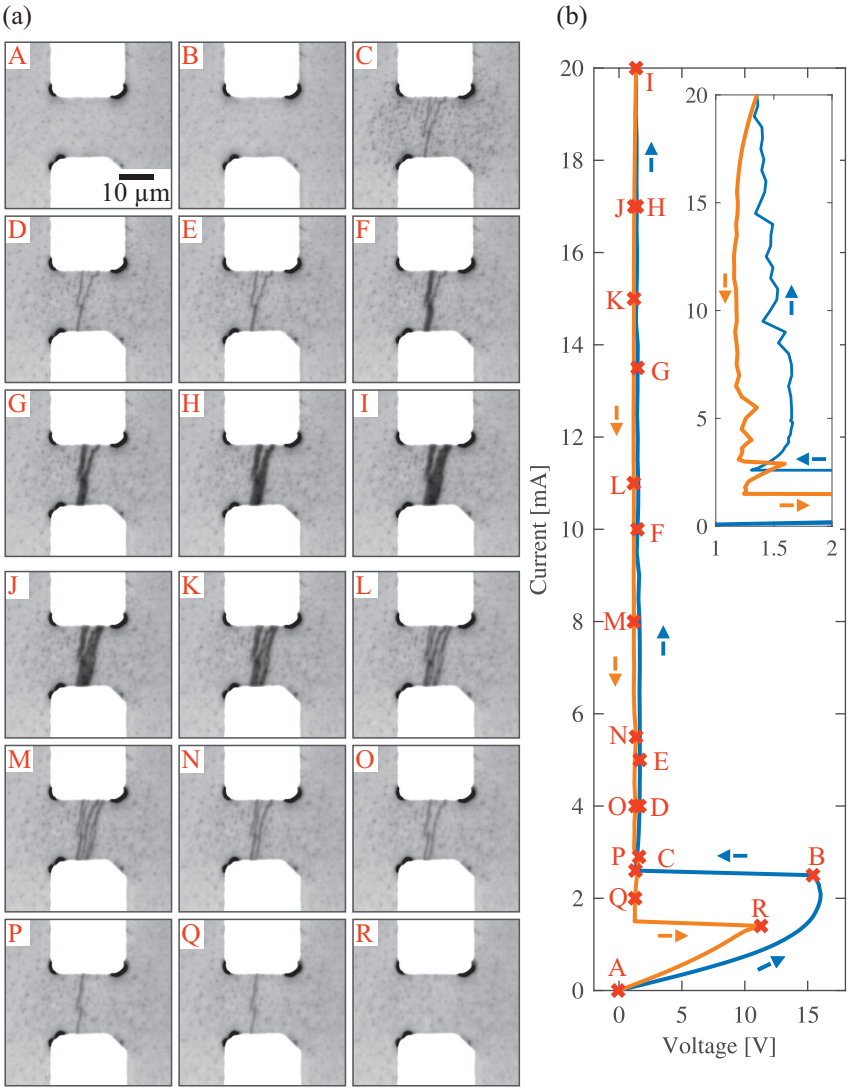

Figure 5.10: Electrical breakdown in V_2O_3 at 158 K. (a) Images of the device at different bias currents throughout the first IV at 158 K after thermal cycling. (b) Corresponding IV curve. The highlighted points, labeled A-R, indicate where the images in (a) were taken.

heating increases and it is now possible to sustain a wider electro-thermal domain. In a perfectly homogeneous material this would lead to a smooth increase in filament width and a smooth IV-curve with perfect voltage regulation, as the filament would always be at critical width for a given current. However, due to the spatial variation of transition temperatures and thermal hysteresis described in Sec. 5.2, this is not the case here and the filament growth proceeds through steps. When the current is increased the filament grows by switching adjacent domains when their insulator-metal transition temperature is exceeded. A domain that has been switched will remain metallic until the temperature drops below the metal-insulator-transition temperature. As a consequence, the critical relationship between current and filament width is not fulfilled at any time. Whenever the filament grows by a larger domain, there is drop in voltage because the filament width now is larger than the critical value. This drop is followed by an increase in voltage that shows ohmic behavior until the critical relation between current and filament width is reestablished. This behavior can be seen in the inset in Fig. 5.10 (b), showing a zoom on the part of the IV after breakdown. When the current is reduced from the maximum value, the filament first remains almost unchanged (J), which is due to the thermal hysteresis between IMT and MIT. The filament starts to split up into several narrower filaments (K-M) when the temperature has decreased to the point where it locally falls below the metal-insulator transition temperature and insulating domains can be created within the filament. As the current decreases, the filaments disappear one after another (M-O) until there is only one filament left (P). Whenever a filament disappears, the current is redistributed to the remaining filaments and a slight increase in voltage is observed that is followed by a reduction in voltage that shows ohmic behavior. As the current is redistributed, the remaining filaments heat up and are no longer critical and hence show ohmic behavior. Only when the current is reduced far enough to reach the critical state, the voltage regulation kicks back in. A jump to higher voltages is seen in the IV, when the last filament vanishes (R). The corresponding image shows a recovery of the insulating state, although the voltage (and resistance) remain lower than in the up-sweep.

The mean filament width, that has been determined by calculating the sum of all filament areas and dividing by their length, is shown in Fig. 5.11 (a) as a function of bias current. In the up-sweep the filament growth proceeds through steps that occur when the current has reached the critical value for

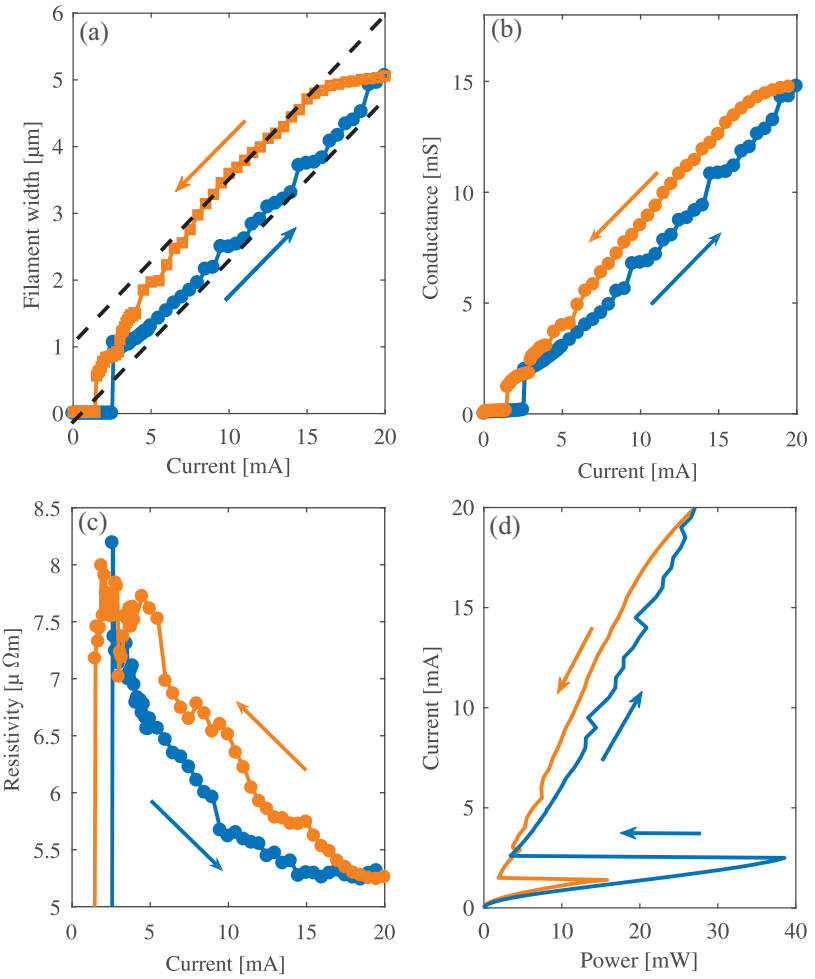

Figure 5.11: Electrical breakdown in V_2O_3 at 158 K. The up-sweep of the IV is shown in blue, the down-sweep of the IV in orange. (a) Mean filament width vs. current. The width shows a linear current dependency for most of the IV. The broken lines indicate the critical relation between current and filament width. (b) Device conductance vs. current bearing strong resemblance to filament width. (c) Resistivity of the filament vs. current, estimated from filament width. (d) Power dissipated in the device vs. current. The power is at maximum just before breakdown.

a given width (indicated by the broken line) and Joule heating allows for a wider filament. The steps in filament width are linked to the switching of large domains that are adjacent to the filament. In the down-sweep, the filament width remains nearly constant until the current has dropped to a value where Joule heating is insufficient to sustain the filament. Now, the filament width decreases linearly with current following a critical relation for the maximum width that can be sustained by Joule heating. The hysteresis in filament width can be attributed to the hysteresis between IMT and MIT in temperature. Interestingly, the decrease in filament width is much smoother compared to the growth. This can be explained by the smaller domain size for the metal-insulator transition that leads to a smoother response and the fact that the filament splits up into several filaments, which increases the area of the boundary at which a change of filament width can appear. The accelerated decrease for bias currents below 8 mA indicates a change in the balance between Joule heating and filament width. This can be attributed to the successive vanishing of filaments that starts at 8 mA and leads to a reduction of the boundary area between the filaments and the surrounding insulating phase and consequently modifies the dissipation of heat to the film and substrate.

The conductance $G = I/U$ of the device as a function of bias current is shown in Fig. 5.11 (b). Comparing this with Fig. 5.11 (a) reveals a strong correlation between conductance and filament width that confirms that the current is indeed confined to the filament, and furthermore implies that a significant modulation of filament thickness (spatial extent of the filament over the thickness of the V_2O_3-film) is absent. Assuming that the filament extends over the full thickness of the film, it is possible to calculate the resistivity of the filament, displayed in Fig. 5.11 (c). The resistivity shows a small current dependence that is likely to be due to an overestimation of the filament width at low bias currents, where the width is close to the resolution of the microscope. At 20 mA, the resistivity is $\approx 5\,\mu\Omega$m, which is close to the resistivity of the metallic phase of $4.618\,\mu\Omega$m that will be determined in Sec. 5.4.2. This result supports the idea of a constant filament width throughout the complete film thickness.

Figure 5.11 (d) shows the power $P = U\,I$ dissipated within the device as a function of bias current. At low bias currents ($I \lesssim 1$ mA), where self-heating is negligible, the power shows an parabolic increase with current. However, this soon changes to a more or less linear dependence which continues up to the breakdown. The maximum power of almost 40 mW is reached

immediately before the breakdown. The fact that the voltage (and with it the electric field) decreases slightly before breakdown [cf. Fig. 5.10 (b)] while the power is at maximum at the breakdown hints towards a thermally driven breakdown rather than an electric-field induced effect. After breakdown, the power shows a nearly linear relationship to the bias current which is due to the voltage regulation discussed above.

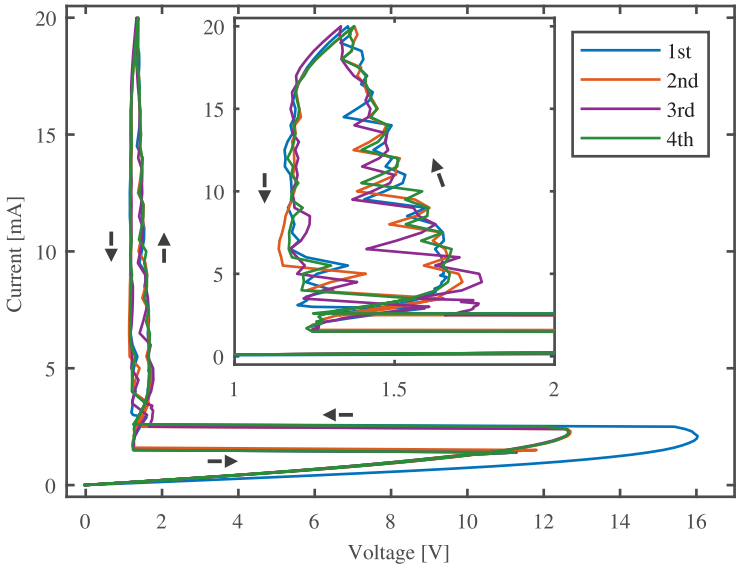

Figure 5.12: Consecutive IVs at 158 K. The starting resistance and maximum voltage are reduced after the first IV. The inset shows a zoom on the part after breakdown.

Figure 5.12 shows the four consecutively acquired IVs at 158 K. Overall, the IVs are very similar with the exception of the part before the breakdown in the first IV. The first IV starts at a higher resistance and reaches a higher maximum voltage compared to the subsequent IVs. The breakdown and recovery, however, occur at the same bias currents of 2.5 mA and 1.5 mA, respectively. The difference between the first and subsequent IVs can be explained by the history of the device. Before the measurement

of the first IV, the sample was cooled to 80 K. During the measurement of the first IV, parts of the device were heated to higher temperatures, some even above T_{IMT}, before returning to the bath temperature of 158 K. Although they are in the insulating state at 158 K, as can be verified from the corresponding images, they have a lower resistivity than before the first IV. This is consistent with the fact that the $R(T)$ curve shows hysteresis for temperatures at which the images indicate a homogeneous insulating state (see also Sec. 5.2). Note, that the up-sweep of the subsequent IV-curves follows the trace of the down-sweep of the first IV.

The evolution of filaments throughout the four IVs is shown in Fig. 5.13 for specific bias currents. Right after the breakdown, at 2.5 mA in the up-sweep, a narrow filament is observed. While the first IV shows a branched filament, the 2nd and 4th IV show a single filament and the 3rd IV shows two filaments. After increasing the current to 10 mA, the filaments have grown in width and only one filament is observed for all of the IVs (although it is branched for the 1st IV). At the maximum current of 20 mA, the filaments have grown to a width of approximately 5 μm. In the down-sweep, at a current of 10 mA, the filament has split into several narrower parts. These disappear one after another (down-sweep 5 mA) until only one filament remains at 1.5 mA. This filament vanishes when the current is further reduced, leading to the recovery of the insulating state. Overall the filament configuration is similar for all of the IVs. In particular, the filament configuration in the 2nd and 4th IV is nearly identical. Interestingly, a different filament configuration, as for example in the 2nd and 3rd IV, leads to very similar global current-voltage characteristics. This is due to the critical relation between current and filament width. Small differences between the IVs can be understood in terms of slight local variations of transition temperature and hysteresis. Although the current-voltage characteristic is changed after the breakdown in the first IV, the device properties are not permanently altered. After thermal cycling the device is restored to the initial state and both the current-voltage characteristics and the $R(T)$ curve, can be reproduced.

5.3.2 Electrical breakdown at variable temperature

After having studied the breakdown at a temperature of 158 K, in the following the behavior at higher temperatures throughout the insulator-metal transition will be discussed. The evolution of IVs for increasing

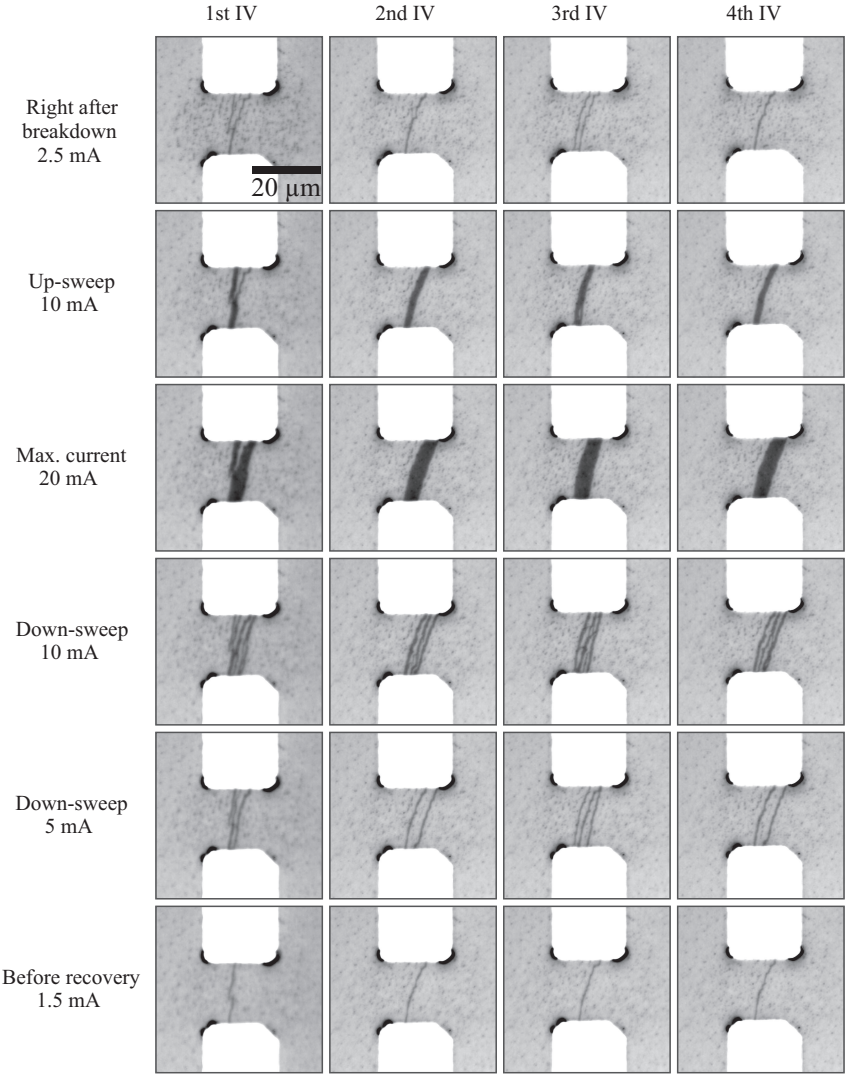

Figure 5.13: Evolution of filaments throughout the consecutive IVs for specific bias currents at a temperature of 158 K.

temperatures throughout the insulator-metal transition is shown in Fig. 5.14 for selected temperatures. Always the first IV at a given temperature is shown. The sample has been brought into a defined initial state by thermal cycling before the recording of each of these IVs. As can be seen in the

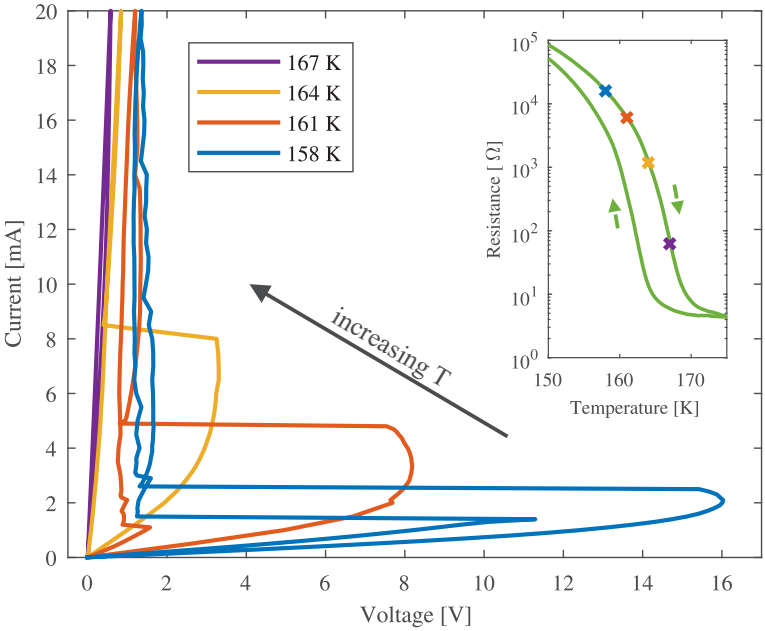

Figure 5.14: First IVs at different temperatures throughout the insulator-metal transition. The sample has been brought into a defined initial state by thermal cycling before the acquisition of each of these IVs. The inset shows the starting points for each of the IVs in the $R(T)$ characteristic. The starting points are highlighted by a cross with the same color as the respective IV.

inset, the starting resistance decreases as the sample progresses through the insulator-metal transition with increasing temperature. While the IVs at 158 K and 161 K show qualitatively similar behavior in terms of breakdown, voltage regulation, and (partial) recovery, the characteristic changes at higher temperatures. The IV at 164 K, for example, shows a breakdown but

no recovery. Also, the part after breakdown is smooth and shows a finite slope with little hysteresis rather than the voltage regulation observed at lower temperatures. The respective breakdown voltage decreases while the breakdown current increases for temperatures from 158 K to 164 K, whereas no breakdown is observed at 167 K.

Subsequently, the breakdown characteristic will be discussed in detail for the four temperatures selected for Fig. 5.14, which are exemplary for the evolution with temperature. However, it should be kept in mind that the changes in the breakdown characteristic evolve gradually between these examples.

Figure 5.15 (a) shows a series of images that have been acquired at selected bias points during the measurement of the first IV at 161 K. The IV and the respective bias points, labeled A to H are shown in Fig. 5.15 (b). At a temperature of 161 K the sample still is almost completely in the insulating state after thermal cycling. However, a few metallic spots are visible in (A). The IV shows a pronounced back bending when the current is increased and, just before breakdown (B), some of the metallic spots have grown slightly. Immediately after breakdown (C), a lot of metallic domains appear within a circular area of 50 μm diameter around the device. Although it is difficult to see, a continuous metallic path formed between the points highlighted by the red arrows. Subsequently, and similar to the 158 K measurement, the IV progresses at approximately constant voltage indicating the presence of electro-thermal domains. As can be seen in (D), at maximum current, several continuous metallic paths have been created within the domain pattern that appeared at breakdown. During the up-sweep from breakdown to maximum current these paths have been formed by switching the insulating regions, that separated the domains, to the metallic state. Furthermore, the paths grow with increasing current and consequently behave just like the filaments observed at 158 K. However, in contrast to lower temperatures, they are not formed in a homogeneous insulating background but exist within a mixed phase. Still, it is apparent from the voltage regulation that the current is confined to the filaments. Consequently, only the region containing the filaments is heated to elevated temperatures while the remaining parts of the sample are close to the bath temperature of 161 K. The metallic domains that have been formed at breakdown persist even when the temperature has dropped back to the bath temperature due to the hysteresis between IMT and MIT. This is consistent with the data presented in Fig. 5.4 where the sample was shown to be in a

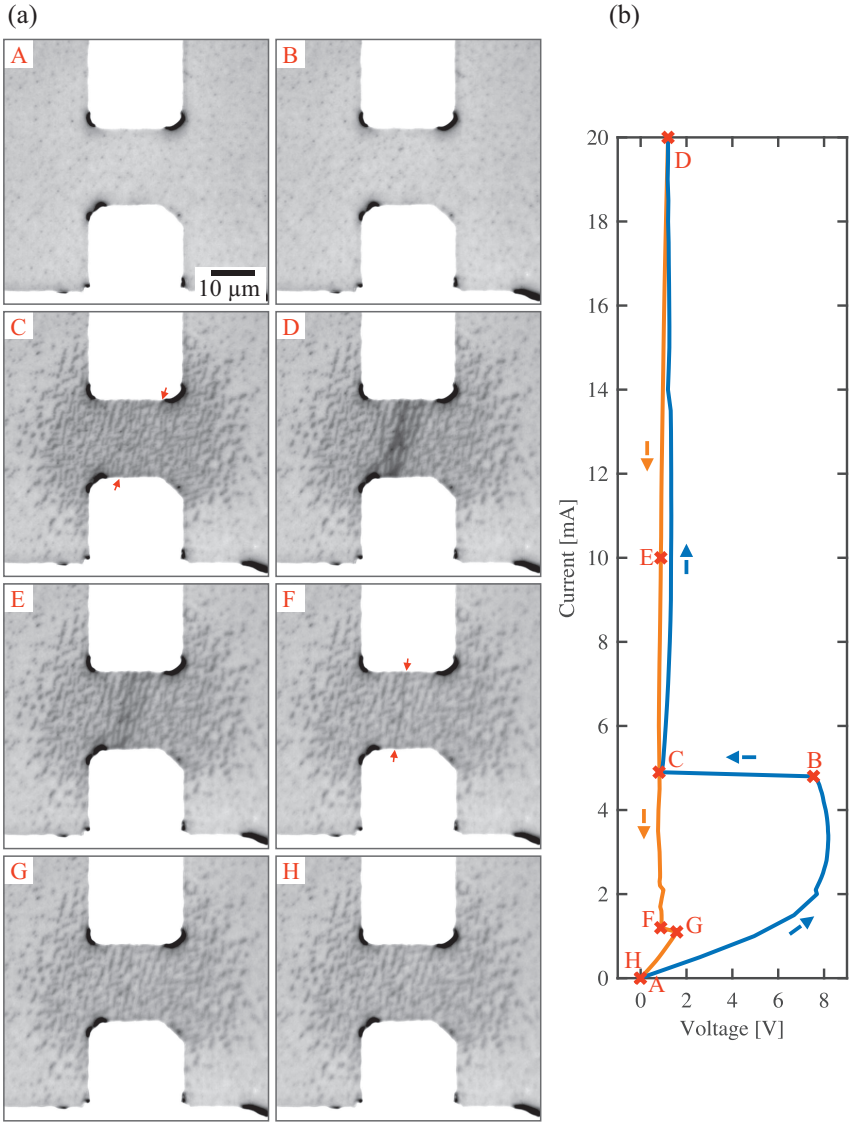

Figure 5.15: Breakdown during first IV at 161 K. (a) Images of the device at selected bias currents. The red arrows in C and F indicate the endpoints of a continuous metallic path. (b) Corresponding current-voltage characteristic. The highlighted points indicate the bias points corresponding to images A-H.

homogeneous insulating state for both the heating and cooling branch, at 158 K whereas it is in the insulating state for the heating branch and in a mixed state for the cooling branch at 161 K. Reducing the current leads to a decrease in the filaments width (E) and subsequently to a disconnection of the filaments by formation of insulating domains. Only one filament, which connects the points highlighted by the red arrows, remains intact at (F). A further reduction in current causes the filament to break, which is accompanied by a jump to higher voltages (G). The sample now shows a considerably lower resistance compared to the initial state due to the domains that have been created at breakdown and the fact that they persist even at zero bias (H).

Figure 5.16 shows the four consecutively acquired IVs at 161 K. Again, the device characteristic is changed after the first IV while the following IVs show similar behavior. The difference between the first IV and the following IVs can be attributed to the persisting domains that are formed during breakdown in the first IV (see Fig. 5.15). Both the current at which the breakdown occurs and the maximum voltage that is reached are reduced after the first IV. The former by a factor of ≈ 1.6, the latter by a factor of ≈ 2. Yet, after breakdown the IV-curves progress similarly in terms of voltage regulation, hysteresis between up- and down-sweep and recovery of the higher-resistive state. The down-sweep from maximum current is almost identical and, at recovery, all four IVs show a jump to higher voltage at the same bias current of 1.3 mA. In the up-sweep, IVs 2 to 4 show slightly different breakdown currents and voltages and a different evolution directly after breakdown which becomes more similar at high bias currents.

These differences can be understood by comparing the filament configuration for the IVs, which is shown in Fig. 5.17 for selected bias currents in the up-sweep of IVs 2 to 4. The domain pattern at zero bias (first row) is similar for the IVs. Immediately after breakdown (second row) a continuous metallic path has formed between the electrodes. The starting and endpoints of the respective paths are highlighted by the red arrows. At a current of 10 mA (third row), the electro-thermal domains connecting the electrodes are easily visible. In contrast to the measurement at 158 K where a single filament was preferred, the electro-thermal domains are composed of several branched filaments and an increase in current leads to both an increase in filament width and the formation of new filaments. Accordingly, at a bias current of 20 mA, the electro-thermal domain consist of a complex network of filaments. The differences in the IV-curves after breakdown

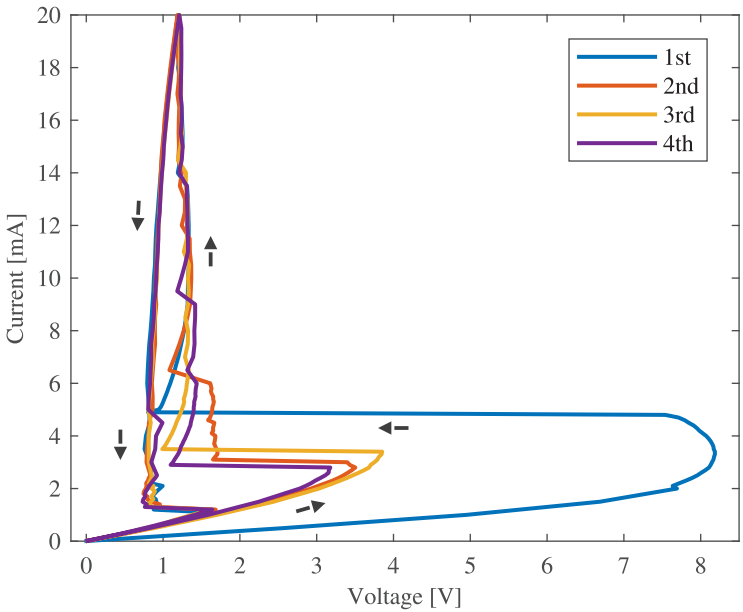

Figure 5.16: Comparison of the four consecutive IVs at 161 K.

can be attributed to the varying configuration of the electro-thermal domains. However, with the increase in domain size and number of filaments for increasing current, the global electrical behavior converges due to the fact that the differences between the individual filaments are averaged out when they connect to a complex network. A reduction in current leads to successive disconnection of the individual filaments until only a single filament is left. When this filament vanishes, the IV shows a jump to higher voltages and the device returns to a similar state as after the first IV.

In the following paragraph the electrical breakdown at a bath temperature of 164 K will be discussed. After thermal cycling to this temperature the sample is still mostly in the insulating state, as can be verified from image L in Fig. 5.4 (b), with only few metallic spots embedded into the insulating matrix. However, it is just before the onset of domain formation with increasing temperature. Looking at Fig. 5.4 (a) it is apparent that the

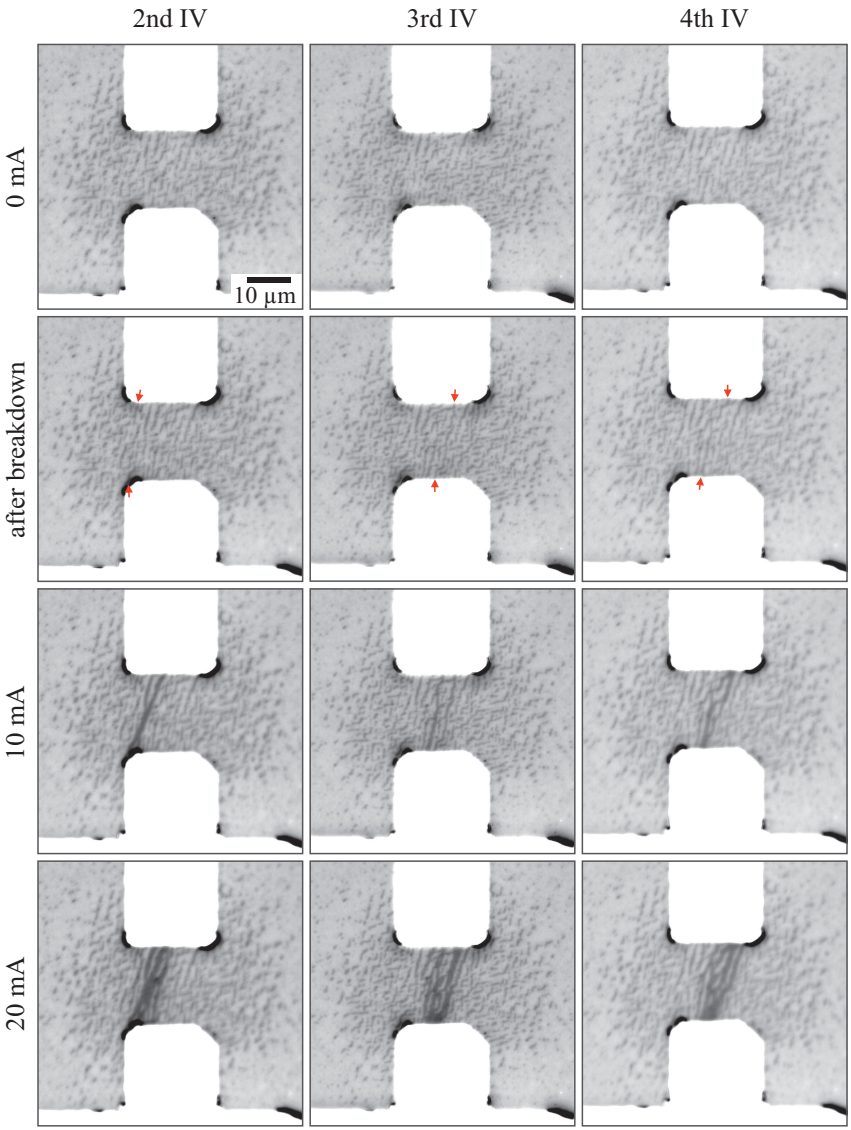

Figure 5.17: Evolution of electro-thermal domains in the up-sweep of the 2nd to 4th IV at a bath temperature of 161 K. The red arrows in the images of the second row (after breakdown) show the endpoints of the continuous metallic paths that formed at breakdown.

resistance ratio between the heating and cooling branch is at maximum at this temperature. Comparing the images at 164 K in the heating and cooling branch (L and E in Fig. 5.4 (b), respectively) shows that, in contrast to the heating branch, the sample is in a mixed state in the cooling branch with a resistance ($\approx 10\,\Omega$) that is close to the value of the metallic phase.

Figure 5.18 (a) shows the sample at selected bias currents throughout the first IV at 164 K. The IV is presented in Fig. 5.18 (b), where the bias points corresponding to the images are highlighted and labeled A to H. Starting from the initial state at zero bias after thermal cycling (A), the IV shows a nearly ohmic behavior up to a current of 2 mA after which it shows a reduction in resistance. A maximum voltage of 3.3 V is reached at (B) where the corresponding image shows that a number of metallic spots have been created in vicinity of the device. Further increase of current leads to a slight reduction in voltage up to point (C), immediately before breakdown, where additional metallic domains have formed between the electrodes. After breakdown (D), a dense network of domains connecting the electrodes has formed. Contrary to the measurements presented above, it is not possible to identify a single conducting path. When the current is increased (E and F) the domain network remains similar to the configuration after breakdown and shows only minor changes in domain width. This is different to the behavior at lower temperatures where either a single filament in an insulating background or multiple filaments in a mixed background have been observed and the filaments showed a modulation of width with current. Consequently, after breakdown, the current-voltage characteristic at 164 K shows a different evolution compared to the voltage regulation observed at lower temperatures. It progresses smoothly with a finite slope, an almost linear relation between current and voltage, and very little hysteresis between up- and down-sweep. The domain network remains nearly unchanged when the current is reduced (G), and the domain width only starts to decrease at small bias currents (< 6 mA), which is accompanied by a slight change of slope (towards higher resistance) in the IV-curve. Notice that there is no recovery to a higher resistive state and the IV-curve progresses smoothly to zero bias (H). This is an important difference compared to lower temperatures. Due to the high bath temperature, it is not possible to switch the metallic domains that have been created at breakdown back to the insulating state. Consequently, the bistability between the high-resistive and voltage-regulated states that has been observed at lower temperatures is lost and the sample is brought into a persisting lower-resistive state through breakdown.

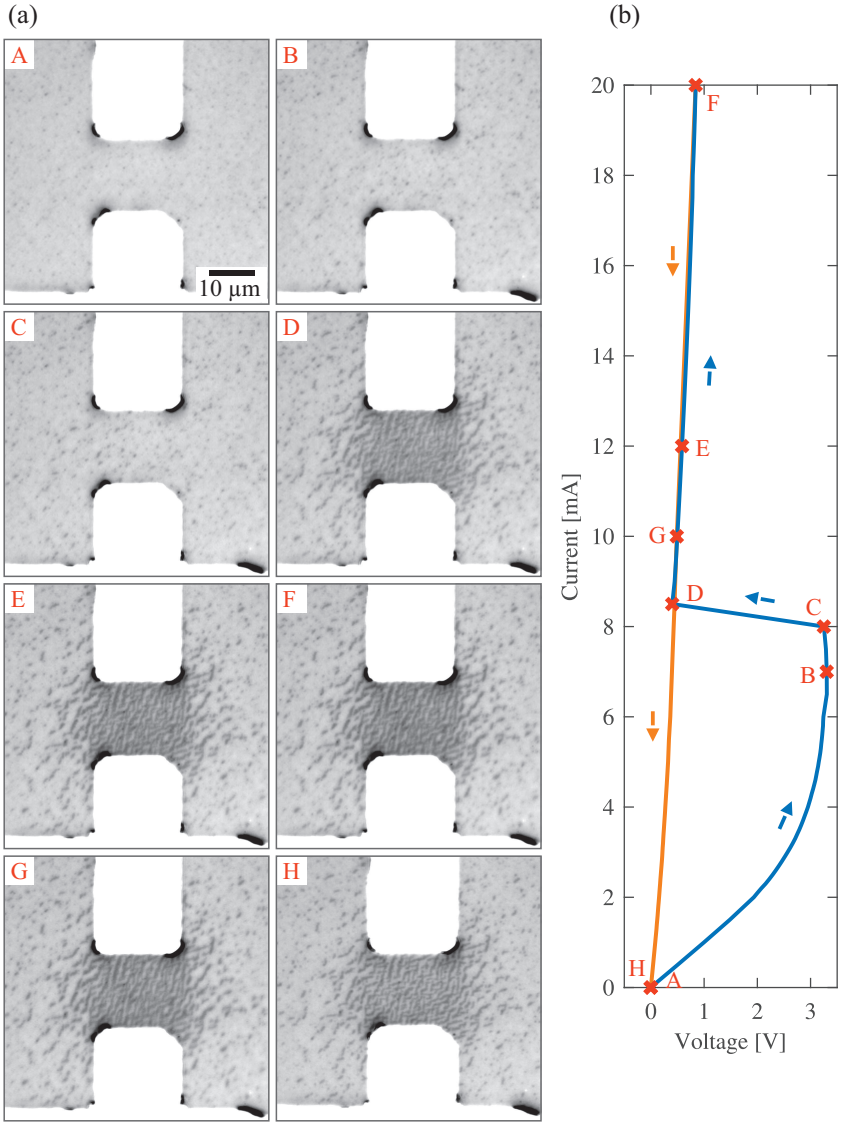

Figure 5.18: Breakdown during first IV at 164 K. (a) Images of the device at selected bias currents. (b) Corresponding current-voltage characteristic. The highlighted points indicate the bias points corresponding to images A-H.

As a consequence no breakdown occurs for the following IVs, as can be seen in Fig. 5.19 showing the four consecutive IVs at 164 K. The second to fourth IV show a very similar progression with a slightly higher resistance than in the down-sweep of the first IV and a more pronounced hysteresis between up-sweep and down-sweep.

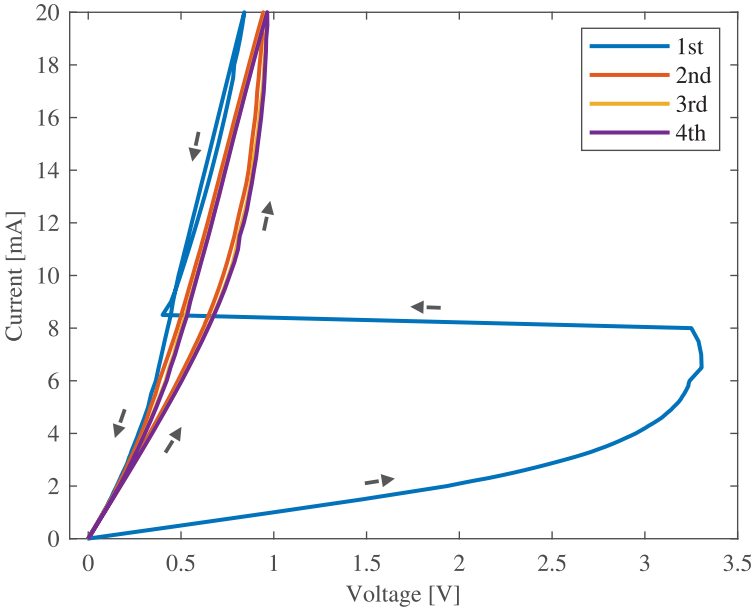

Figure 5.19: The four consecutive IVs at 164 K. The device switched to a lower-resistive state at breakdown during the first IV, from which it is not able to recover. The following IVs are very similar and show no breakdown.

Figure 5.20 shows the device at the beginning (a), at the maximum current (b), and the end (c) of the second IV. The domain configuration of (a) is only slightly changed in (b) and is completely recovered in (c). This becomes more readily visible, when looking at the differences between the images. Figure 5.20 (d) and (e) were obtained by subtracting (a) from (b) and (c), respectively. The dark spots in (d) indicate regions that have been switched to the metallic state after ramping the current to 20 mA. All of

these regions return to the insulating state when the current is swept back to 0 mA, as can be seen from the featureless image (e). The domain evolution

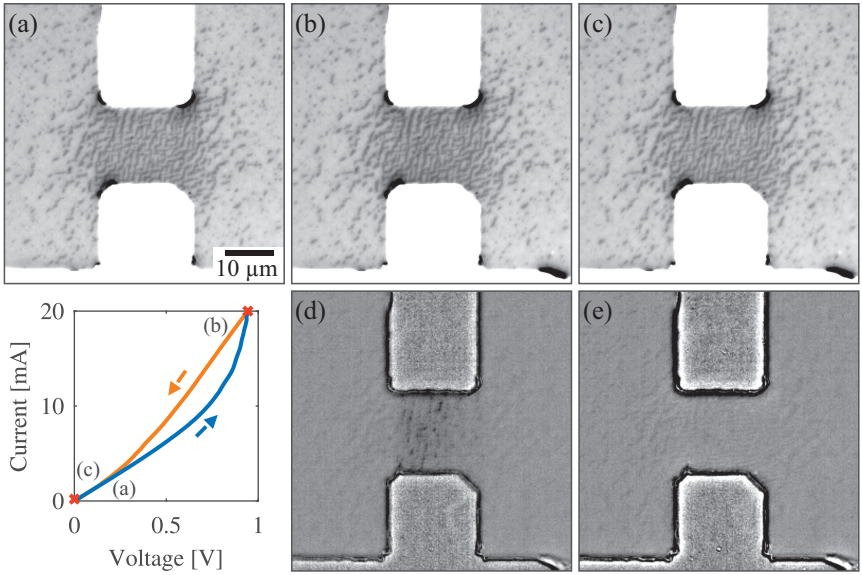

Figure 5.20: Images of the device at bias currents of (a) 0 mA at the beginning, (b) 20 mA and (c) 0 mA at the end of the second IV at 164 K. The difference images (d) and (e) have been obtained by subtracting (a) from (b) and (c), respectively. The graph in the lower left panel shows the corresponding IV.

throughout the 3rd and 4th IV will not be shown as it is similar to the behavior throughout the second IV. The breakdown characteristic at 164 K is different from lower temperatures in that the breakdown occurs through the formation of a dense network of domains rather than the formation of filaments. The sample is at a bath temperature where a recovery from the breakdown is not possible anymore and, accordingly, electric breakdown occurs only in the first IV.

Finally, the behavior at a bath temperature of 167 K will be discussed. At this temperature, the V_2O_3 film already shows elongated metallic domains after thermal cycling. Although the insulator-metal transition is already far advanced and the resistance has dropped to $\approx 46\,\Omega$, the domains

are still separated and no continuous metallic path exists between the electrodes. The evolution of the domain pattern during the first IV is shown in Fig. 5.21 (a). The pattern (A) remains nearly unchanged up to a current of 10 mA (B) after which metallic domains are created uniformly over the whole area shown here. The domain pattern is more dense and the individual domains have connected to longer tracks at the maximum current of 20 mA (C). These domains persist when the current is reduced (D). The

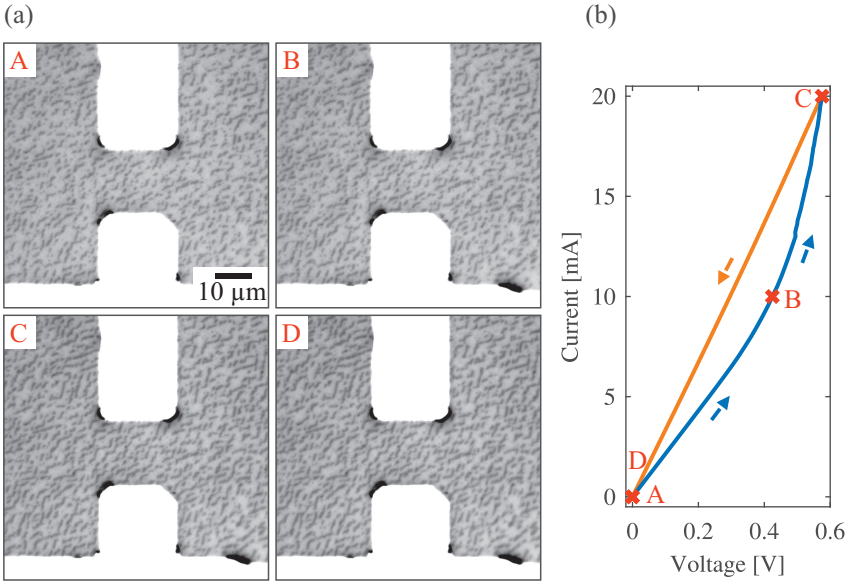

Figure 5.21: Images of the device (a) throughout the first IV (b) at 167 K.

corresponding IV-curve, shown in Fig. 5.21 (b), reveals that the resistance stays nearly constant up to 7 mA where the IV starts to deviate from linear behavior. At (C), the resistance has dropped to $\approx 28\,\Omega$. The down-sweep shows a linear relation of current and voltage which is consistent with the fact that the domain configuration remains unchanged.

While the behavior at 167 K seems unspectacular at first sight, the homogeneous domain creation during up-sweep becomes an interesting aspect when looking at a larger portion of the sample. Domains are created uniformly over the whole field of view of $500\,\mu\text{m} \times 500\,\mu\text{m}$ with

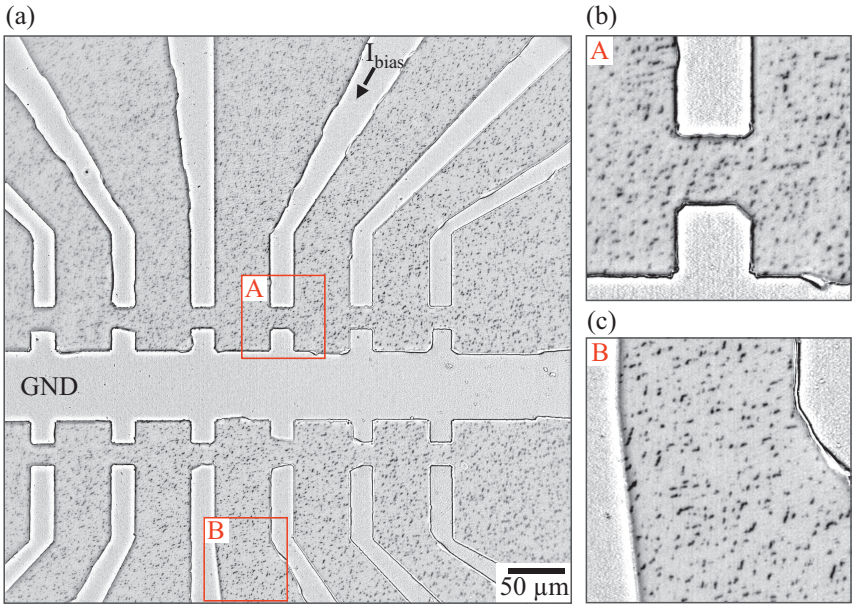

Figure 5.22: Changes in domain configuration (dark) after increasing the current to 20 mA at a temperature of 167 K. (a) Difference image obtained by subtracting the first image at zero bias from the image at $I = 20$ mA. (b) and (c) zoomed view on the rectangles A and B, respectively.

no apparent spatial dependence relative to the device. Figure 5.22 (a) shows the difference image at the maximum current of 20 mA, obtained by subtracting the first image at zero bias. Metallic domains that have been created during the up-sweep appear as dark spots. A zoomed view on the rectangles A and B is given in Fig. 5.22 (b) and (c), respectively. The film is driven further through the insulator-metal transition as the current is ramped up. This change in domain configuration is not localized to the device (A) but is similarly observed at great distances (B). Still, it is clearly correlated with the up-sweep of the IV and can be reproduced after thermal cycling. However, while caused by applying a current to the device, it is surprising that this effect can be observed at great distances to the device. In fact, it is present even beyond the ground plane (B) where the electric

field and current density have to be zero. This raises a question regarding the driving force of this effect. Since it is present in areas that are free of electric field and current (B), a direct electrical driving force can be ruled out. A possible explanation would be a uniform increase in temperature of the V_2O_3 film, which will be discussed hereafter.

First, it is important to notice that the bath temperature was stable within $\pm 2\,\mathrm{mK}$ during acquisition of the IV and the observed change in domain configuration cannot be attributed to a drift in bath temperature. Because of the uniform change in domain configuration it is possible to estimate the temperature of the V_2O_3 film by comparing the device resistance, as calculated from the IV [Fig. 5.21 (b)], to the heating branch of the $R(T)$ curve [see Fig. 5.4 (a)]. The $R(T)$ curve was measured at a small bias current of $5\,\mu\mathrm{A}$, so that Joule heating was negligible. Figure 5.23 shows the equivalent temperature obtained from the $R(T)$ curve as a function of bias current (a) and dissipated power (b). The change in resistance from $I = 0$ to maximum current is equivalent to an increase of about $0.5\,\mathrm{K}$ in temperature. The homogeneous domain pattern indicates that this temperature rise would be nearly constant over the imaged area. Assuming that the current is flowing close to the device this would mean that the thermal decay length [86], that is given by

$$\Lambda = \sqrt{\frac{k\,d}{\alpha}}\,, \tag{5.1}$$

with the thermal conductivity k and the thickness d of the V_2O_3 film and the heat transfer coefficient α between film and bath, had to be much larger than the field of view and would be on the order of at least several millimeters. The heat transfer to the bath can be estimated from the thermal conductivity of sapphire [204] and the substrate thickness of $5 \times 10^{-4}\,\mathrm{m}$ to $\alpha \approx 2 \times 10^5\,\mathrm{W}/\left(\mathrm{m}^2\,\mathrm{K}\right)$, while the thermal conductivity in the V_2O_3 film [205] is $k \approx 4\,\mathrm{W}/\left(\mathrm{m}\,\mathrm{K}\right)$ at $167\,\mathrm{K}$. Inserting these literature values into Eq. (5.1) results in a thermal decay length of about $\Lambda = 2.5\,\mu\mathrm{m}$ for a $300\,\mathrm{nm}$ thick film, which seems to be a reasonable value for lower temperatures where strong thermal gradients at the edges of the electro-thermal domains have been observed. A change in the ratio of thermal conductivity in the film and heat transfer to the substrate of several orders of magnitude with just a few Kelvin change in bath temperature that would be needed to explain a thermal decay length of several millimeters at $167\,\mathrm{K}$ seems unlikely and is not supported by the data in [205] and [204]. Therefore, a uniform

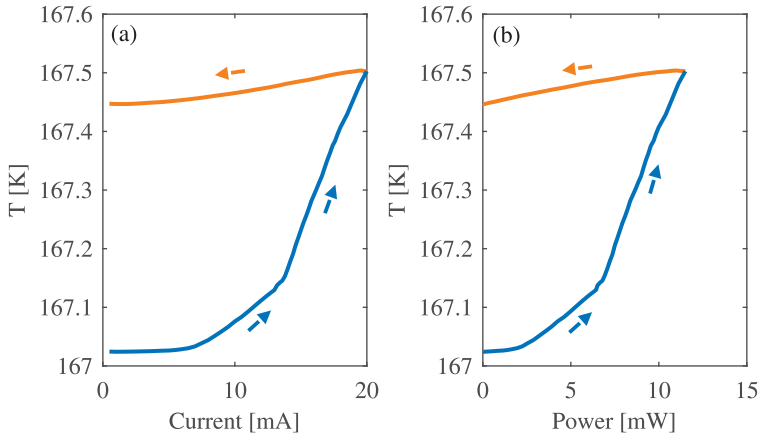

Figure 5.23: Equivalent temperature of the V_2O_3 film, obtained by comparing the resistance throughout the first IV at 167 K [Fig. 5.21 (b)] to the heating branch of the $R(T)$ curve from Fig. 5.4 (a), as a function of bias current (a) and dissipated power (b).

increase in temperature during the up-sweep in the IV can be excluded as the mechanism behind the change in domain configuration. While it has been shown that electrical and thermal effects are unlikely to drive this effect, it was not possible to identify a mechanism that causes the homogeneous creation of domains.

It could, however, be hypothesized that a possible explanation lies in the long-range elastic interaction [173] that, in competition with short-range electronic interactions, leads to the phase separation at the IMT. In analogy to ferromagnets, where the minimization of the demagnetizing field leads to formation of domains, the interplay between elastic energy, strain, and energy gain through electron localization may be influenced by the minimization of a non-local quantity. Such a non-local quantity could, for example, be given by the integral over the elastic energy in the presence of strain. This minimization could be the reason for the presence of elastic domains that are either metallic or insulating due to the strong electron lattice coupling in V_2O_3. As the sample gets closer to the insulator-metal transition in temperature, the energy balance governing the phase

transition becomes more susceptible to small perturbations. Now, if the domain structure is modified locally by sending a current through the device this could lead to a far-reaching effect as the system tries to minimize the integral elastic energy by accommodating the domain pattern.

5.3.3 Summary of electric breakdown behavior

To summarize the observations so far, V_2O_3 shows an electrically induced breakdown of the insulating phase at temperatures close to the insulator-metal transition. At lower temperatures (157 K and 158 K) this breakdown occurs through the formation of a single metallic filament that connects the electrodes of the device. After breakdown, the filament can be understood as an electro-thermal domain and the IV progresses at constant voltage. This voltage regulation is due to an accommodation of filament width with current. When the current is reduced to a value where Joule heating is insufficient to sustain the electro-thermal domain the insulating state is recovered. Just before breakdown occurs, the IV shows a back bending and the fact that the power is at maximum at breakdown while the electric field is reduced before breakdown hints towards a thermally induced breakdown of the insulating phase. At intermediate temperatures (159 K to 166 K), the breakdown characteristic gradually changes from nucleation of a single filament through the creation of multiple filaments and domains in the vicinity of the device to the occurrence of a dense network of domains between the electrodes with increasing temperature. For temperatures of 163 K and above a breakdown has only been observed in the first IV after thermal cycling. Instead of the filaments observed at lower temperatures, a dense network of domains is created, and consequently the IVs show a finite slope after breakdown instead of the voltage regulation. The higher resistive state is not recovered when the current is reduced and therefore no breakdown is observed in the subsequent IVs. At higher temperatures (167 K to 169 K), no breakdown is observed but increasing the current leads to the formation of domains over a large area of the film. This change in domain pattern cannot be explained by a direct influence of electric field, current or Joule heating, as none of these factors reach far enough to be able to cause the observed alteration of the domain pattern. Instead a long-range elastic coupling is suggested as the mechanism behind this effect. The breakdown characteristics are summarized in Fig. 5.24.

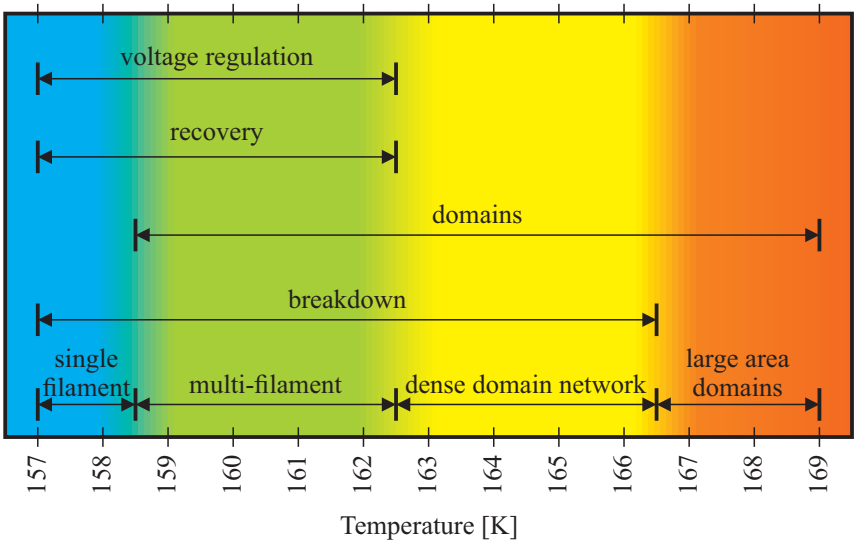

Figure 5.24: Summary of breakdown characteristics for different bath temperatures.

The evolution of electrical parameters associated with breakdown is shown in Fig. 5.25 (a) for different bath temperatures. The current, voltage and dissipated power is evaluated directly before breakdown, i.e. the jump to lower voltages in the IV. The breakdown current increases with temperature. This increase is very pronounced for the first IV and less prominent for the subsequent IVs. The breakdown voltage, on the other hand decreases steadily with temperature and is higher for the first IV compared to the following IVs. The dissipated power just before breakdown shows a differing temperature evolution for the first IV compared to the following IVs. It remains more or less constant up to a temperature of 161 K, where it starts to decrease in a nearly linear manner, whereas the data for the following IVs shows a strong decrease over the whole temperature range. While the behavior for the second to fourth IV is very similar, the breakdown in the first IV is different. This is due to the initialization by thermal cycling and can be understood as a non-reversible change in device characteristics that occurs before or at the breakdown in the first IV.

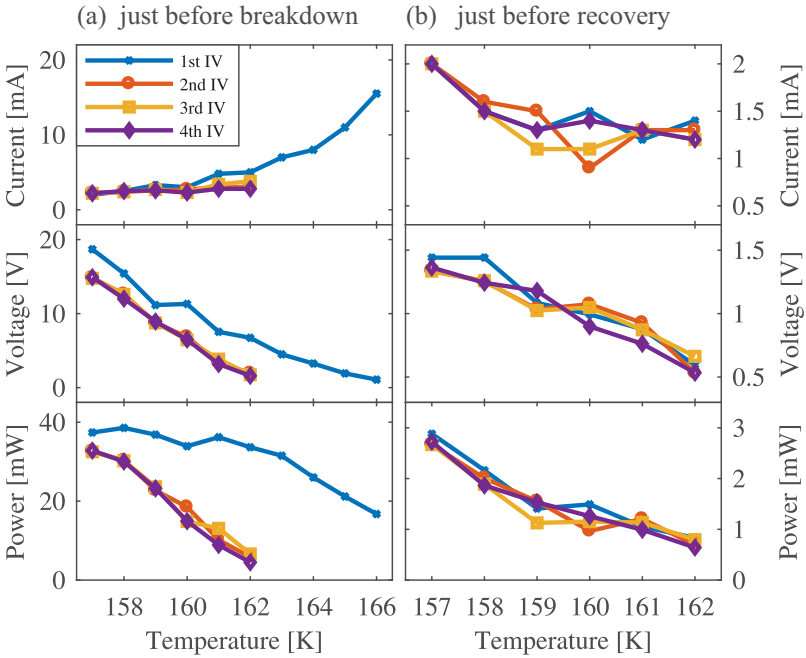

Figure 5.25: Summary of the characteristic parameters current, voltage, and power (from top to bottom) vs. bath temperature, (a) just before breakdown and (b) just before recovery. These were obtained from the four consecutive IVs at each temperature.

Figure 5.25 (b) shows the current, voltage, and dissipated power immediately before recovery of the higher resistive state as a function of temperature. All three parameters decrease with temperature and are similar for the four consecutive IVs that have been acquired at each temperature.

The device characteristics after breakdown can be quite well explained through the presence of electro-thermal domains. However, the question whether the breakdown is thermally induced or caused by electric field remains to be answered. Although the back bending in the IV hints towards a thermal effect, an electric field induced breakdown is still possible. If the

threshold field for a field-induced breakdown decreases with temperature, self-heating in the device would cause the threshold field to drop. Because the device temperature rises with increasing bias current, it would be possible that the threshold field is exceeded at a point in the IV where the back bending already led to a reduction in electric field.

5.4 Numerical model

In order to shed light on the question whether the electrically-driven insulator-metal transition in V_2O_3 is mediated by Joule heating or driven by electric field, a numerical model has been set up which is able to reproduce the most important characteristics observed in the experiment. The model, which is solved in two dimensions, takes into account the coupling between current density and temperature that is established through Joule heating and the strongly temperature-dependent resistivity of the V_2O_3 film. The temperature-dependent resistivity is modeled using the measured local transition temperatures (Fig. 5.8). Electrically, the sample is represented by a resistor network and solved through mesh current analysis. The thermal characteristics are modeled by solving a finite-differences approximation to the time-dependent heat equation.

5.4.1 Resistor network and mesh current analysis

As has been shown in Sec. 5.2 the metal-insulator transition in V_2O_3 goes along with a coexistence of insulating and metallic domains over a finite temperature interval, which leads to a highly spatially dependent resistivity. To calculate the current distribution in such a non-homogeneous material, the sample is approximated by a resistor network that is constructed from a square primitive cell with edge length $\Delta x = \Delta y$ that contains a node and 4 resistors. The resulting resistor network, obtained by assembling n primitive cells in x-direction and m primitive cells in y-direction, is shown in Fig. 5.26. The resistors within each primitive cell with index i, j with $i \in \{1, m\}$ and $j \in \{1, n\}$ are assigned the same resistance $R_{i,j}$. The resistors at the left and right edge of the resistor network are truncated, making the boundary insulating, and a perfectly conducting wire connects the bottom and top edge to the current source. The loops formed by four neighboring nodal points and the resistors between them are called essential meshes. The complete resistor network contains $a = (n-1)(m+1)$ essential meshes

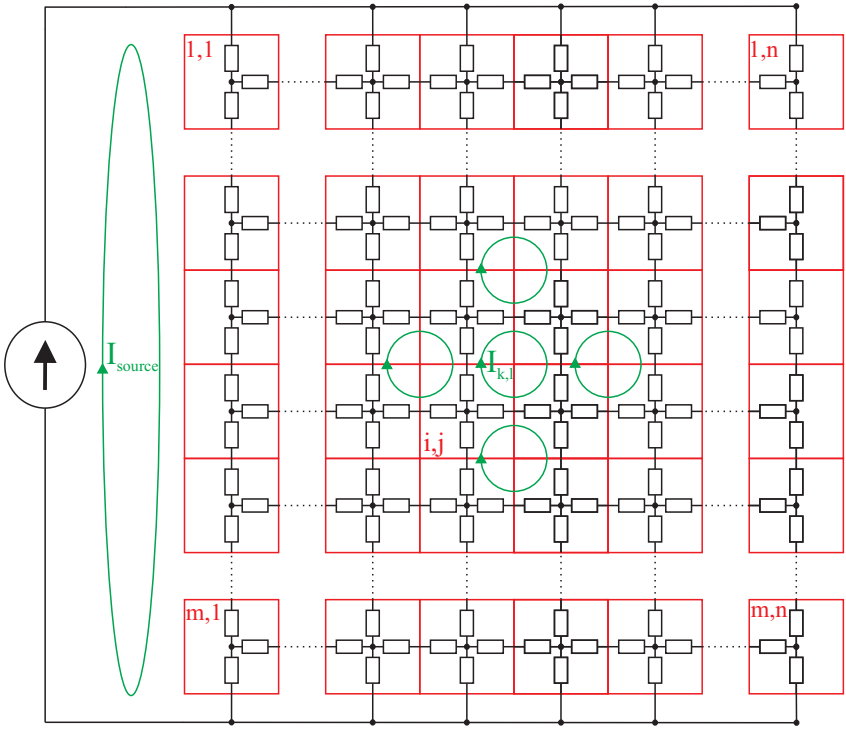

Figure 5.26: Resistor network of $m \times n$ primitive cells used to approximate the resistivity of the sample. Each primitive cell (red squares) contains a node and 4 resistors (except for the columns $j = 1$ and $j = n$ with only 3 resistors per primitive cell). A mesh current $I_{k,l}$ (green) flows in each of the essential meshes of the resistor network. An additional mesh containing the current source is connected to the left side of the resistor network.

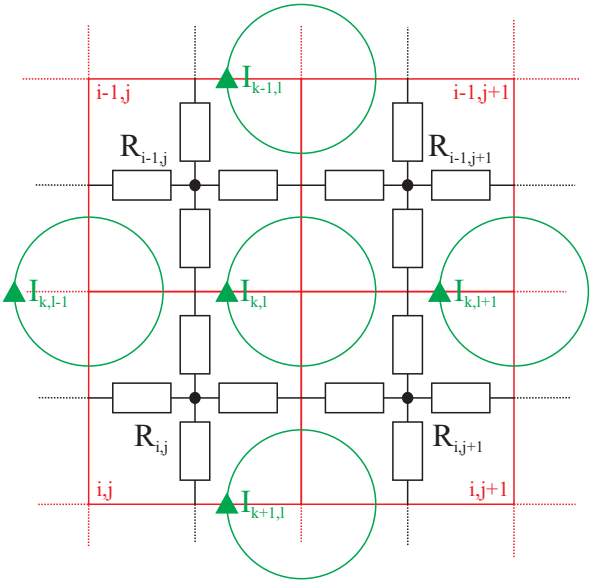

Figure 5.27: Close up of the essential mesh k, l. The current through the resistors in the mesh is given by the difference between the mesh current $I_{k,l}$ and the neighbouring mesh currents.

with index k, l with $k \in \{1, m+1\}$ and $l \in \{1, n-1\}$ plus an additional current source mesh that is connected to the left side of the resistor network. A clockwise circulating current $I_{k,l}$ flows in each of the essential meshes. Figure 5.27 shows a close up of the essential mesh k, l. Following Kirchhoff's second law, the sum of the voltages across the resistors in an essential mesh is equal to zero. The current through the resistors is given by the difference between the mesh current $I_{k,l}$ and the neighboring mesh currents, which have to satisfy the equation

$$\begin{aligned} &(R_{i-1,j} + R_{i-1,j+1})\,(I_{k,l} - I_{k-1,l}) \\ &+ (R_{i,j} + R_{i-1,j})\,(I_{k,l} - I_{k,l-1}) \\ &+ (R_{i-1,j+1} + R_{i,j+1})\,(I_{k,l} - I_{k,l+1}) \\ &+ (R_{i,j} + R_{i,j+1})\,(I_{k,l} - I_{k+1,l}) = 0\ , \end{aligned} \tag{5.2}$$

which can also be written as

$$\begin{aligned} &- (R_{i-1,j} + R_{i-1,j+1})\, I_{k-1,l} - (R_{i,j} + R_{i-1,j})\, I_{k,l-1} \\ &+ 2\,(R_{i-1,j} + R_{i-1,j+1} + R_{i,j} + R_{i,j+1})\, I_{k,l} \\ &- (R_{i-1,j+1} + R_{i,j+1})\, I_{k,l+1} - (R_{i,j} + R_{i,j+1})\, I_{k+1,l} = 0 \ . \end{aligned} \tag{5.3}$$

For the complete resistor network this gives a set of $a = (n-1)(m+1)$ equations plus the equation $I_{\text{source}} = I_{\text{bias}}$ for the current source mesh, which serves as boundary condition. This set of equations is assembled into a $(a+1) \times (a+1)$ matrix **EC** so that the equation system can be written in matrix form as

$$\mathbf{EC} \cdot \begin{pmatrix} I_{11} \\ \vdots \\ I_{1,n-1} \\ \vdots \\ I_{m+1,n-1} \\ I_{\text{source}} \end{pmatrix} = \begin{pmatrix} 0 \\ \vdots \\ 0 \\ \vdots \\ 0 \\ I_{\text{bias}} \end{pmatrix} \ . \tag{5.4}$$

Solving this equation system returns the mesh currents, from which the current through each of the 4 resistors (Fig. 5.28) in the primitive cell i, j can be calculated according to

$$I_{i,j,1} = I_{k,l} - I_{k,l-1} \tag{5.5}$$

$$I_{i,j,2} = I_{k+1,l} - I_{k,l} \tag{5.6}$$

$$I_{i,j,3} = I_{k+1,l} - I_{k+1,l-1} \tag{5.7}$$

$$I_{i,j,4} = I_{k+1,l-1} - I_{k,l-1} \ , \tag{5.8}$$

where, by convention, currents flowing in positive x- and y-direction have positive sign. These describe the current flow between adjacent primitive cells and are defined on the boundary between them. Although it is not properly defined it is desirable to evaluate the current density at the nodes. It is calculated by interpolating the current densities at the boundaries of

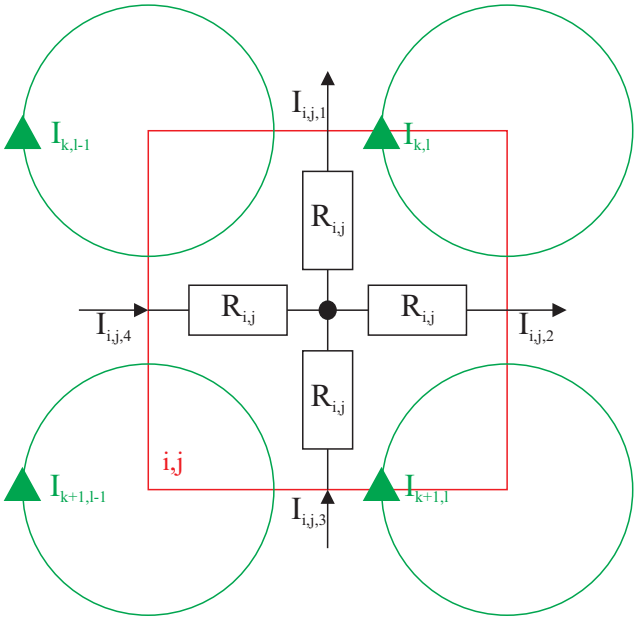

Figure 5.28: The currents $I_{i,j,1}$ to $I_{i,j,4}$ flowing through the resistors in the primitive cell i, j are calculated from the adjacent mesh currents.

the primitive cell, which delivers the current densities $J^x_{i,j}$ in x-direction and $J^y_{i,j}$ in y-direction, as well as the magnitude of the current density $J^{\mathrm{norm}}_{i,j}$

$$J^x_{i,j} = \frac{I_{i,j,2} + I_{i,j,4}}{2\,\Delta y\, d_\mathrm{f}} \tag{5.9}$$

$$J^y_{i,j} = \frac{I_{i,j,1} + I_{i,j,3}}{2\,\Delta x\, d_\mathrm{f}} \tag{5.10}$$

$$J^{\mathrm{norm}}_{i,j} = \sqrt{\left(J^x_{i,j}\right)^2 + \left(J^y_{i,j}\right)^2}\,, \tag{5.11}$$

with the edge lengths of the primitive cell Δx and Δy and the film thickness d_f. Note that these quantities approach the correct value only for Δx, $\Delta y \to 0$ and might deviate from the correct solution for finite dimensions of the

primitive cell. Therefore, they are only used for displaying the results and not as input for further calculations. The power density $p_{i,j}$ generated through Joule heating in the primitive cell of volume $V_{i,j}$ is a quantity that will be used for modeling the thermal characteristics of the sample and is given by

$$p_{i,j} = \frac{P_{i,j}}{V_{i,j}} = \frac{R_{ij}}{\Delta x \, \Delta y \, d_\mathrm{f}} \left(I_{i,j,1}^2 + I_{i,j,2}^2 + I_{i,j,3}^2 + I_{i,j,4}^2 \right) \ . \tag{5.12}$$

For the reasons mentioned above, the currents through the boundaries are used to calculate the power dissipated in the resistors within the primitive cell instead of approximating it by $p_{i,j} = \rho \left(J_{i,j}^\mathrm{norm} \right)^2$.

5.4.2 Definition of temperature-dependent resistivity

After setting up the equations for calculating the electric transport through the sample, it is necessary to define the resistor matrix $R_{i,j}$ that will be used as input for the mesh current analysis. Since the primitive cell is square, the value of $R_{i,j}\,(T)$ is given by

$$R_{i,j}\,(T) = \rho\,(x,y,T)\,\frac{\Delta x}{2\,\Delta y\,d_\mathrm{f}} = \rho\,(x,y,T)\,\frac{\Delta y}{2\,\Delta x\,d_\mathrm{f}} = \frac{\rho\,(x,y,T)}{2\,d_\mathrm{f}} \ , \tag{5.13}$$

and depends only on the film thickness d_f and the resistivity $\rho\,(x,y,T)$ evaluated at the central node of the primitive cell i,j. To approximate the temperature dependence of the samples resistivity, the following assumptions are made: First, the resistivity ρ_met in the metallic phase is constant with respect to temperature and lateral position. Second, the resistivity ρ_ins deep into the insulating phase (at temperatures far from the transition) is homogeneous over the V_2O_3 film and has the same temperature dependence as the globally measured $R(T)$. Third, for cool-down of the sample, the increase in resistivity from ρ_met to ρ_ins in the transition region between these regimes is described by a function $\mathrm{k}\,(T_\mathrm{MIT}\,(x,y) - T)$ that increases from 0 above the metal-insulator transition temperature T_MIT to 1 at low temperatures. So that the resistivity for cool-down of the sample is described by the function

$$\rho\,(x,y,T) = \rho_\mathrm{ins}\,(T)\ \mathrm{k}\,(T_\mathrm{MIT}\,(x,y) - T) + \rho_\mathrm{met} \ . \tag{5.14}$$

Similarly, for warm-up of the sample, the decrease in resistivity in the transition region is described by the same function $\mathrm{k}\,(T_\mathrm{IMT}\,(x,y) - T)$, that

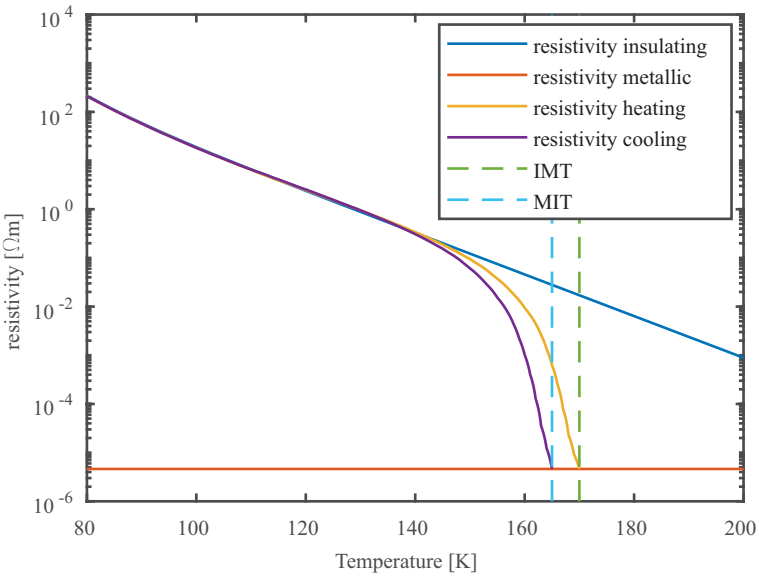

Figure 5.29: Temperature dependence of the V_2O_3 resistivity. The resistivity in the insulating phase ρ_{ins} is shown in blue, the resistivity ρ_{met} in the metallic phase in red, the resistivity in the cooling branch in purple, and the resistivity in the heating branch in yellow. For the cooling branch the resistivity increases from ρ_{met} to ρ_{ins} for temperatures below the metal-insulator transition temperature T_{MIT} (vertical blue dashed line). The resistivity in the heating branch decreases towards the insulator-metal transition temperature T_{IMT} (vertical green dashed line).

now has the difference between the insulator-metal transition temperature T_{IMT} and the temperature as argument

$$\rho\left(x,y,T\right)=\rho_{\mathrm{ins}}\left(T\right)\,\mathrm{k}\left(T_{\mathrm{IMT}}\left(x,y\right)-T\right)+\rho_{\mathrm{met}}\ . \tag{5.15}$$

Since the transition temperatures vary spatially, this leads to a inhomogeneous resistivity in the transition region, while the resistivity is homogeneous outside of the transition region. Note that the transition temperatures $T_{\mathrm{MIT}}\left(x,y\right)$ and $T_{\mathrm{IMT}}\left(x,y\right)$ that are used here to define the temperature

dependence of the resistivity have been measured (cf. Fig. 5.8), which should allow for a good spatial representation of the resistivity.

The resistivity in the metallic phase has been determined by adjusting its value until it agrees with the measurement. A value of $\rho_{\mathrm{met}} = 4.618 \times 10^{-6}\,\Omega\mathrm{m}$ was obtained. The resistivity at low temperatures was obtained by fitting the measured $R(T)$ in the temperature range from 80 K to 130 K with the function

$$\rho_{\mathrm{ins}}(T) = a\mathrm{e}^{bT} + c\mathrm{e}^{dT} \ , \tag{5.16}$$

which returned the parameters $a = 4.66 \times 10^8\,\Omega\mathrm{m}$, $b = -0.1926\,1/\mathrm{K}$, $c = 3.19 \times 10^5\,\Omega\mathrm{m}$, and $d = -0.09849\,1/\mathrm{K}$. The function k that describes the transition between the metallic and insulating phase is obtained by running the mesh current analysis with the matrix $R_{i,j}(T)$ as input for temperatures throughout the transition region and adjusting k until the measured resistance is reproduced. The resulting temperature-dependent resistivity is shown in Fig. 5.29.

5.4.3 Finite-difference approximation to heat equation

Heat transfer in solids is described by the parabolic partial differential equation, known as the heat equation,

$$\rho\, c_P \frac{\partial T}{\partial t} - \nabla \cdot (k \nabla T) = \dot{q}_V \ , \tag{5.17}$$

with the density ρ, the heat capacity at constant pressure c_P, thermal conductivity k, and the volumetric heat source $\dot{q}_V$. In two dimensions and for a film thickness d_{f} this can be written as

$$\rho\, c_P \frac{\partial T}{\partial t} - \frac{\partial}{\partial x}\left(k_x \frac{\partial T}{\partial x}\right) - \frac{\partial}{\partial y}\left(k_y \frac{\partial T}{\partial y}\right) = \dot{q}_V \ , \tag{5.18}$$

or, if the thermal conductivity $k = k_x = k_y$ is isotropic, as

$$\frac{\partial T}{\partial t} - \kappa\left(\frac{\partial^2 T}{\partial x^2} + \frac{\partial^2 T}{\partial y^2}\right) = \frac{\dot{q}_V}{\rho c_P} \ , \tag{5.19}$$

with the thermal diffusivity $\kappa = k/(\rho c_P)$. The partial derivatives in the heat equation can be approximated by finite differences. The same discretization in space as for the mesh current analysis will be used and the variables are

evaluated on the central node of the primitive cell with index i, j. The time is discretized into time steps Δt and an index τ is introduced describing the point in time. The heat equation can be approximated in space and time using a number of finite-difference methods. Here, the backward Euler method is used which, in contrast to the forward Euler or Crank-Nicolson method, is unconditionally stable and immune to oscillations. For a node spacing of Δx and Δy and a time step Δt the implicit discrete form of Eq. (5.19) is given by

$$\frac{T_{i,j}^{\tau+1} - T_{i,j}^{\tau}}{\Delta t} - \kappa \left(\frac{T_{i,j+1}^{\tau+1} - 2T_{i,j}^{\tau+1} + T_{i,j-1}^{\tau+1}}{(\Delta x)^2} + \frac{T_{i+1,j}^{\tau+1} - 2T_{i,j}^{\tau+1} + T_{i-1,j}^{\tau+1}}{(\Delta y)^2} \right) = \frac{\dot{q}_{i,j}^{\tau}}{\rho\, c_P} \ . \tag{5.20}$$

At this point, an additional temperature coupling to the bath with temperature T_b is introduced which is a consequence of the heat flow to the coldfinger through the substrate of thickness d_s. This can be modeled as a heat source $\dot{Q}_\mathrm{b} = k_\mathrm{b} \left(T_\mathrm{b} - T_{i,j}^{\tau+1}\right) \Delta x \Delta y / d_\mathrm{s}$ that is given by the power that is transfered to the bath through a cuboid with cross section $\Delta x\, \Delta y$, length d_s, and thermal conductivity k_b. So that the volumetric heat source in Eq. (5.20) is represented by the sum of Joule heating $p_{i,j}$ and a contribution of $\dot{Q}_\mathrm{b}$ lumped to the volume $V_{i,j}$

$$\dot{q}_{i,j}^{\tau} = p_{i,j}^{\tau} + \frac{\dot{Q}_\mathrm{b}}{V_{i,j}} = p_{i,j}^{\tau} + \frac{k_\mathrm{b}}{d_\mathrm{f} d_\mathrm{s}} \left(T_\mathrm{b} - T_{i,j}^{\tau+1}\right) \ . \tag{5.21}$$

It is further assumed, that the node spacing in x- and y-direction is equal ($\Delta x = \Delta y$). With the thermal diffusivity to the bath $\kappa_\mathrm{b} = k_\mathrm{b} / (\rho\, c_p)$, Eq. (5.20) becomes

$$T_{i,j}^{\tau+1} - T_{i,j}^{\tau} - \frac{\kappa\, \Delta t}{(\Delta x)^2} \left(T_{i-1,j}^{\tau+1} + T_{i,j-1}^{\tau+1} - 4T_{i,j}^{\tau+1} + T_{i,j+1}^{\tau+1} + T_{i+1,j}^{\tau+1}\right) = \frac{p_{i,j}^{\tau}\, \Delta t}{\rho\, c_P} + \frac{\kappa_\mathrm{b}\, \Delta t}{d_\mathrm{f}\, d_\mathrm{s}} \left(T_\mathrm{b} - T_{i,j}^{\tau+1}\right) \ . \tag{5.22}$$

Rearranging this equation so that terms at time $\tau+1$ are on the left hand side and terms at time τ are on the right hand side results in

$$T_{i,j}^{\tau+1} - \frac{\kappa\,\Delta t}{(\Delta x)^2}\left(T_{i-1,j}^{\tau+1} + T_{i,j-1}^{\tau+1} - 4T_{i,j}^{\tau+1} + T_{i,j+1}^{\tau+1} + T_{i+1,j}^{\tau+1}\right) - \frac{\kappa_\mathrm{b}\,\Delta t}{d_\mathrm{f}\,d_\mathrm{s}}\left(T_\mathrm{b} - T_{i,j}^{\tau+1}\right) = T_{i,j}^{\tau} + \frac{p_{i,j}^{\tau}\,\Delta t}{\rho\,c_P}\ , \tag{5.23}$$

which is further simplified to

$$-A_\mathrm{f}\,T_{i-1,j}^{\tau+1} - A_\mathrm{f}\,T_{i,j-1}^{\tau+1} + (1+4A_\mathrm{f}+A_\mathrm{b})\,T_{i,j}^{\tau+1} - A_\mathrm{f}\,T_{i,j+1}^{\tau+1} - A_\mathrm{f}\,T_{i+1,j}^{\tau+1} - A_\mathrm{b}T_\mathrm{b} = T_{i,j}^{\tau} + A_\mathrm{q}\,p_{i,j}^{\tau}\ , \tag{5.24}$$

by introducing the coefficients $A_\mathrm{f} = \kappa\,\Delta t/\left(\Delta x\right)^2$, $A_\mathrm{b} = \kappa_\mathrm{b}\,\Delta t/\left(d_\mathrm{f}\,d_\mathrm{s}\right)$, and $A_\mathrm{q} = \Delta t/\left(\rho\,c_P\right)$. These equations are assembled into a $(m\cdot n+1)\times(m\cdot n+1)$ heat transfer matrix $\mathbf{HT}$ so that the equation system is given by

$$\mathbf{HT}\cdot\begin{pmatrix} T_{11}^{\tau+1} \\ \vdots \\ T_{1n}^{\tau+1} \\ \vdots \\ T_{mn}^{\tau+1} \\ T_\mathrm{b} \end{pmatrix} = \begin{pmatrix} T_{11}^{\tau} + A_\mathrm{q}\,p_{1,1}^{\tau} \\ \vdots \\ T_{1n}^{\tau} + A_\mathrm{q}\,p_{1,n}^{\tau} \\ \vdots \\ T_{mn}^{\tau} + A_\mathrm{q}\,p_{m,n}^{\tau} \\ T_\mathrm{bath} \end{pmatrix}\ , \tag{5.25}$$

where the last row contains the equation $T_\mathrm{b} = T_\mathrm{bath}$ which is used to set the bath temperature as boundary condition.

The metal-insulator phase transition in V_2O_3 is connected to the occurrence of a latent heat of approximately $\Delta H = 2\,\mathrm{kJ/mol} \approx 13.3\,\mathrm{kJ/kg}$ that has to be supplied to the system to change from one phase to the other [206]. The latent heat, which is represented by a jump in enthalpy H, leads to a diverging heat capacity $c_P = \mathrm{d}H/\mathrm{d}T$ at the phase transition [207]. The latent heat is represented in the numerical model by introducing a temperature dependent heat capacity

$$c_P\left(T\right) = c_{P0} + \frac{\Delta H}{\sqrt{\pi}\Delta T}e^{\frac{(T-T_\mathrm{c})^2}{\Delta T^2}}\ , \tag{5.26}$$

where a constant heat capacity $c_{P0} = 450\,\mathrm{J/\left(kg\,K\right)}$ and a finite width $\Delta T = 0.1\,\mathrm{K}$ of the phase transition around the transition temperature T_c is assumed. The heat capacity according to Eq. (5.26) is shown in Fig. 5.30.

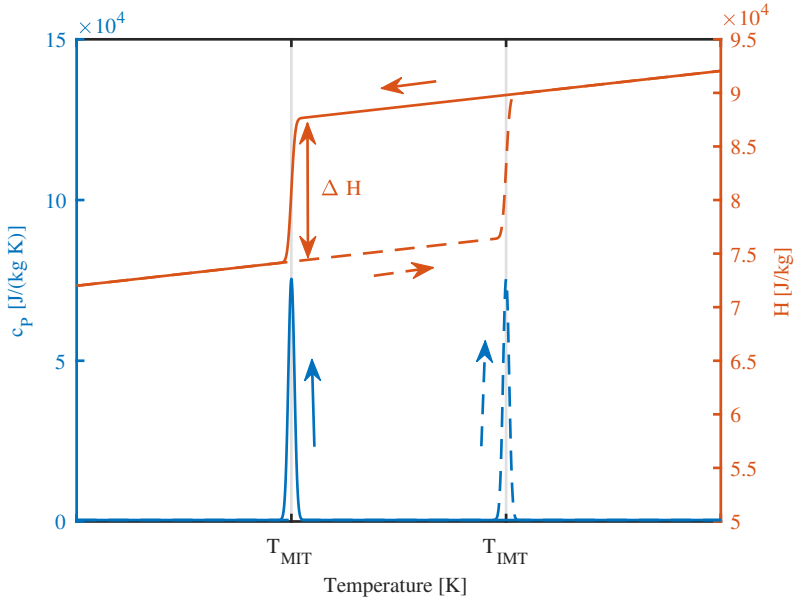

Figure 5.30: Temperature dependent heat capacity c_P (blue curve) and enthalpy H (red curve). The latent heat ΔH at the phase transition leads to a jump in enthalpy and a peak in heat capacity. Broken lines show the insulator-metal transition at T_{IMT}, solid lines the metal-insulator transition at T_{MIT}.

5.4.4 Simulation of electric breakdown in V_2O_3

To simulate the electric breakdown in V_2O_3 the equations for the current distribution and heat transfer [Eq. (5.4) and Eq. (5.25)] are implemented and solved in MATLAB [208]. This is done by initializing the system at zero bias current ($I_{\mathrm{bias}} = 0$) and the bath temperature ($T_{i,j} = T_{\mathrm{bath}}$) for $t = 0$ and slowly ramping the current to $I_{\mathrm{bias}}^{\mathrm{max}} = 20\,\mathrm{mA}$ and back to $I_{\mathrm{bias}}^{\mathrm{end}} = 0\,\mathrm{mA}$ over time with a rate that is much slower than the thermal dynamics of the sample, so that the system is modeled in quasi-static approximation. Figure 5.31 shows the programs flow chart. First, the system is initialized at the bath temperature, zero bias current and completely in the insulating phase. Then, the resistivity $R_{i,j}$ for the initial temperature and phase is calculated. The bias current is increased to the value at the next time step $t + \Delta t$. The mesh

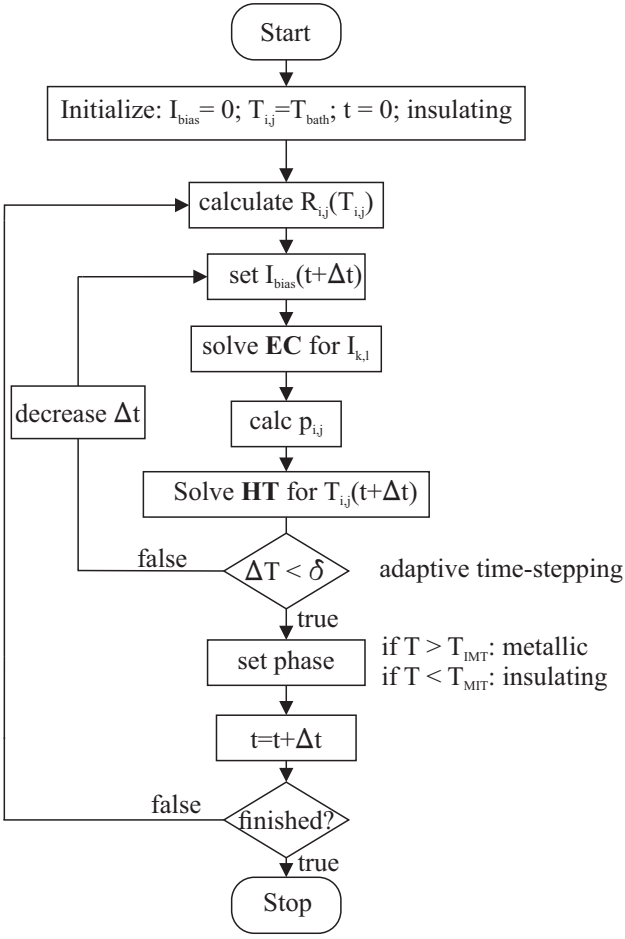

Figure 5.31: Flow chart for the simulation

current analysis is solved and the current distribution is calculated. The Joule heating is calculated from $R_{i,j}$ and the current distribution and input into the heat equation which is solved for the temperatures $T_{i,j}\,(t+\Delta t)$. Note that, due to the strong temperature dependence of resistivity and heat capacity, the system is highly nonlinear as it approaches the metal-insulator or insulator-metal transition. To accurately capture the nonlinearities a sufficiently small time step Δt needs to be used. This is accomplished by using an adaptive time step. If the maximum change in temperature

$$\Delta T = \max_{\forall i,j} \left(\left| T_{i,j}\,(t+\Delta t) - T_{i,j}\,(t) \right| \right) \tag{5.27}$$

is larger than the convergence criterion δ, the time step is reduced and the temperature distribution is recalculated using the smaller time step. If ΔT is far below the convergence criterion, the time step is increased. When the convergence criterion is satisfied, the phase transition is evaluated: the material is set to the metallic phase, where the insulator-metal transition temperature T_{IMT} is exceeded and to the insulating phase, where the temperature has fallen below the metal-insulator transition temperature T_{MIT}. Subsequently, the time is incremented and the calculated temperature and phase distribution are used as inputs to calculate the new resistivity $R_{i,j}$. The program runs in a loop, progressing through time, until the bias current has reached its final value.

5.4.5 Simulation results

The results of this simulation in comparison with the experiment are shown in Fig. 5.32 for a bath temperature of 158 K. The first column shows the experiment, i.e. images of the device throughout the IV, while the 2nd to 4th column shows the simulation results: the current density J^{norm}, the temperature T and the phase (metallic or insulating), respectively. The measured and simulated IV are shown in Fig. 5.32 (b). Both show a similar progression: Starting at zero bias the IVs show a high resistance, followed by a back bending and a breakdown of the insulating phase. The voltage stays nearly constant after breakdown. The inset in Fig. 5.32 (b) shows a zoom on the voltage regulated part of the IVs. Although the simulated IV is shifted to higher voltages compared to the measurement, both have a remarkably similar shape. They possess a comparable hysteresis between up- and down-sweep and show a number of small jumps that can be attributed

to changes in filament width. At low bias currents in the down-sweep, the IVs show a jump to higher voltage and subsequently coincide with the up-sweep, which means that the initial state is recovered. In the simulation, however, this jump is not as abrupt as in the measurement.

The first row (A) in Fig. 5.32 (a) shows the sample and simulation immediately before breakdown. While the experiment and simulated phase reveal that both are completely in the insulating state, the current density and temperature are not homogeneous. This is due to the temperature-dependent resistivity in the insulating phase that favors current flow along the domains with a lower insulator-metal transition temperature T_{IMT}. An increase in bias current leads to breakdown of the insulating phase (B) and a filament is observed in both the simulation and the experiment. The simulated current density shows that the current is confined to the metallic filament which is heated to above T_{IMT} by Joule heating, while the temperature rapidly decays to the bath temperature outside of the filament. A pertinent observation is that the simulation reproduces the orientation of the filament very well. A further increase in bias current (C), leads the filament to grow in width. This growth appears exclusively towards the right-hand side of the device. In contrast to the experiment, the simulation shows a slight branching of the filament. At the maximum current of 20 mA (D), the filament has grown to a width of about 5 μm in both the experiment and simulation. In the down-sweep, the filament starts to split up into several narrower filaments (E). While this behavior is reproduced in the simulation, the filament configuration is slightly different. The experiment shows three separate filaments (F) with parallel orientation, whereas the filaments are connected at several points along their length in the simulation. Still, the integral width of the filaments is comparable. When the bias current is further reduced, the filaments vanish successively. Two filaments remain at a current of 5 mA (G) and an increase in voltage due to the vanishing of the third filament, is seen in the IVs. Only one filament survives at current of 3 mA (H). The insulating state is recovered when this filament disappears. In the simulation, the recovery of the insulating state is not as abrupt, and at a lower bias current, compared to the experiment. Instead of an instantaneous switching from metallic to insulating, the filament first breaks into shorter parts that subsequently return to the insulating state.

Altogether, the simulation reproduces the shape of the IV, the filament formation and evolution, as well as its orientation and size. The good agreement between the purely electro-thermal simulation and the experiment

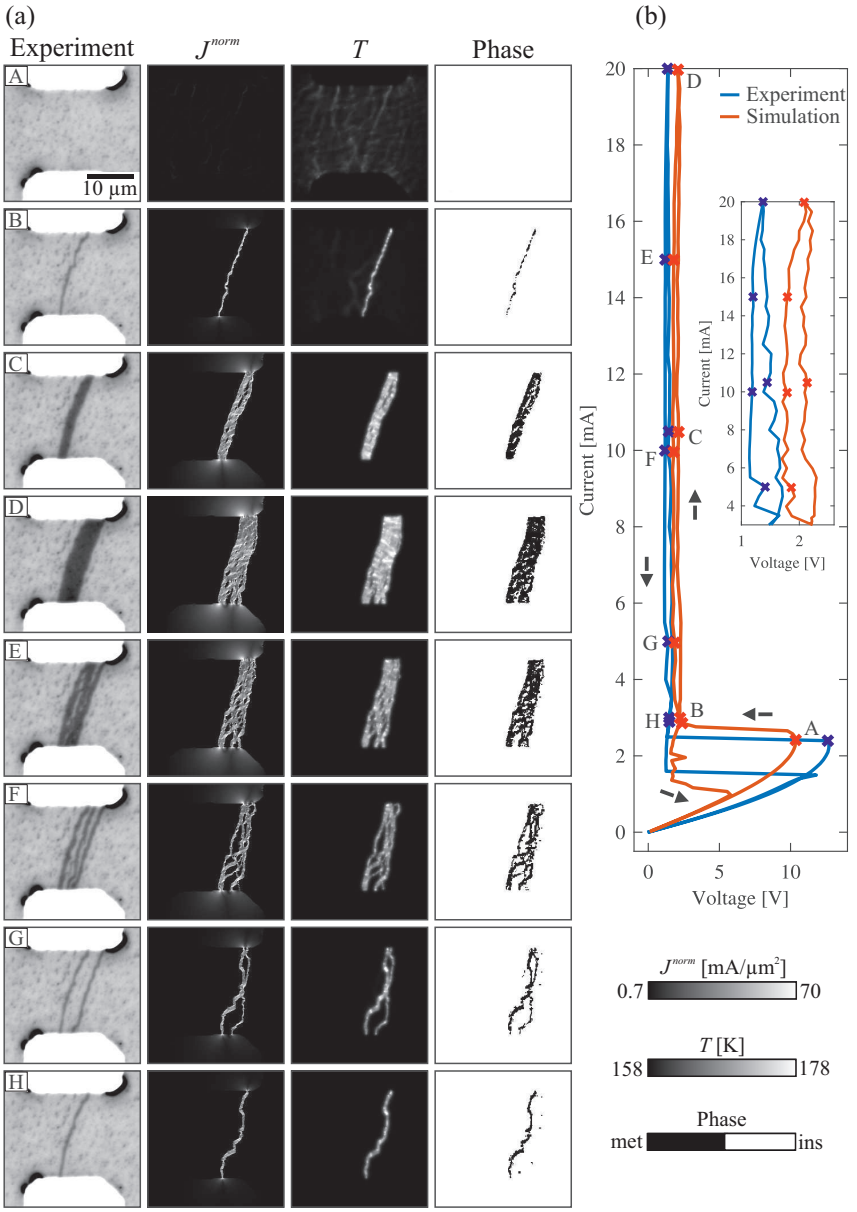

Figure 5.32: Simulation results for a bath temperature of 158 K.

confirms that the electrically driven insulator-metal transition in V_2O_3 is caused by Joule heating and self-reinforced current focusing due to the negative temperature coefficient of the materials resistivity within the insulator-metal transition.

5.5 Conclusions

In conclusion, low-temperature widefield microscopy has been applied to study the phase transition of V_2O_3 from a paramagnetic metal to an antiferromagnetic insulator. This phase transition, that is commonly regarded as a prototypical Mott-Hubbard transition, is observed in bulk stoichiometric V_2O_3 when cooling below a temperature of $\approx 150\,\mathrm{K}$. Due to the strong electron-lattice coupling, the transition temperature is shifted slightly in strained thin films. Moreover, a phase separation [173] into metallic and insulating domains occurs at the metal-insulator transition. Here, imaging of this phase separation by low-temperature widefield microscopy has been demonstrated for the first time and it was possible to confirm the results obtained by McLeod *et al.* [173].

At temperatures close to the insulator-metal transition V_2O_3 can be driven from the insulating to the metallic state by applying a large enough bias current. Whether this electric breakdown of the insulating phase is driven by electric field or Joule heating is in the focus of recent research. This work is also the first to realize optical imaging of the electric breakdown at the insulator-metal transition of V_2O_3. The results of this study show that the electric breakdown is influenced by the underlying domain structure. At the lowest investigated temperatures (157 K and 158 K) the breakdown occurs through the formation of a metallic filament that follows the directionality of the domains, observed at the MIT. This filament grows in width when the current is increased. This accommodation of filament width causes the current-voltage characteristic to progress at constant voltage (voltage regulation). The growth is not continuous but evolves by switching domains, adjacent to the filament, to the metallic state. Reducing the current causes the filament to split into several narrower parts that vanish successively. The insulating state is recovered when the last filament disappears.

The breakdown characteristic changes with increasing bath temperature and the influence of the underlying domain structure becomes more promi-

nent. The metallic phase pattern created at breakdown changes from single filament to multiple filaments (159 K to 162 K) and ultimately to a dense network of domains (163 K to 166 K). The voltage regulation and recovery of the insulating state have only been observed for temperatures up to 162 K, where the breakdown goes along with the formation of filaments between the electrodes. It is inferred that the occurrence of current filamentation, voltage regulation and recovery of the insulating state are closely intertwined.

No breakdown is observed at higher temperatures ($T > 166\,\mathrm{K}$) and applying bias currents of up to 20 mA leads to the creation of metallic domains over a large area of the V_2O_3 film. The mechanism for this long-range modification of the domain pattern remains unidentified. However, it was shown that a direct electric or thermal influence is unlikely to be able to drive this effect. Instead, a long-range elastic coupling of domains that might explain the non-local switching is suggested. Yet, further work needs to be done to establish whether such a long-range elastic interaction exists and is sufficiently strong to generate the observed changes in the domain pattern.

Complementary numerical calculations reveal that, at least at a temperature of 158 K where the breakdown is characterized by the formation of a single filament, the electrically driven metal-insulator transition in these V_2O_3 devices can be explained by the self-reinforced current focusing caused by Joule heating coupled to the negative temperature coefficient of the resistivity. Future work will explore the presented model for other bath temperatures throughout the insulator-metal transition.

While the results of this study indicate that the breakdown of the insulating phase is thermally driven, it should be noticed that the electric fields reached throughout the study have been moderate ($< 1\,\mathrm{V}/\mu\mathrm{m}$) and an electric-field induced insulator-metal transition may still be possible. It might become observable at temperatures far from the insulator-metal transition where a thermal breakdown is not possible or in nano-scale devices where it might be possible to reach higher field strengths.

6 | Summary and Outlook

This thesis describes the development of a high-resolution combined scanning laser- and widefield polarizing microscope for imaging at temperatures from 4 K to 300 K and the application of this instrument to studies on the properties of two material systems that are in the focus of recent research: the two-dimensional electron gas at the interface of $LaAlO_3$ and $SrTiO_3$ and the metal-insulator transition in the correlated oxide V_2O_3.

The microscope provides two imaging modes: the low-temperature scanning polarizing microscope (LTSPM) and the low-temperature widefield polarizing microscope (LTWPM). Both imaging modes achieve an excellent spatial resolution of ~ 240 nm for the LTSPM and ~ 480 nm for the LTWPM and provide a high sensitivity to the orientation of the plane of polarization of $5.0 \times 10^{-6}\,\mathrm{rad}/\sqrt{\mathrm{Hz}}$ for the LTSPM and $1.0 \times 10^{-4}\,\mathrm{rad}/\sqrt{\mathrm{Hz}}$ for the LTWPM. The sample is mounted on a ^{4}He continuous flow cryostat that allows imaging at sample temperatures from 4 K to 300 K, and magnetic fields with variable orientation and a magnitude of up to 800 mT can be applied to the sample. In addition to the acquisition of the intensity reflected from a sample, the polarization sensitive detectors allow for the observation of ferromagnetic domains via the magneto-optical Kerr effect and ferroelastic or ferroelectric domains via birefringence and bireflectance. The magnetic stray field of a sample, as for example a superconductor, can be measured by employing the Faraday effect in a magneto-optical indicator film that is placed on top of the sample. Additionally, the LTSPM provides an imaging mode, low-temperature scanning laser microscopy (LTSLM), that gives access to the local electric transport properties of a sample. This is accomplished by locally perturbing the sample using the laser beam and measuring the beam-induced voltage change across the current-biased sample.

The microscope provides a versatile tool for the investigation of spatial correlations of magnetic, structural, and electric order and has the potential to deliver significant findings that enhance knowledge in the research on spintronic, spin-caloritronic, superconducting, magnetic and many other material systems.

An example of structural order that has been imaged using the microscope are twin walls between ferroelastic domains in tetragonal $SrTiO_3$ and their influence on the two-dimensional electron gas at the interface between a $LaAlO_3$ layer and a $SrTiO_3$ substrate. Due to their polarity, twin walls modulate the electric transport characteristics of the two-dimensional electron gas. The influence of twin walls on the electric transport has been imaged using low-temperature scanning electron microscopy (LTSEM) and LTSLM. The twin walls show as stripe-like features in the LTSEM and LTSLM images that appear at angles with respect to the crystallographic axes that perfectly match the orientations that can be deduced from the tiling rules of tetragonal domains. The appearance of twin walls with the predicted orientation has been confirmed by optical imaging with the LTWPM. It has been found that ferroelectric order within the twin walls can be induced by an electric field that exceeds a threshold value of 1.5 kV/cm.

$SrTiO_3$ is widely used as a substrate material and is usually assumed to be a perfect single crystal in this regard. The present findings are of broad relevance as they show that this assumption does not hold true for the tetragonal phase of $SrTiO_3$ and suggest that the presence of polar or ferroelectric twin walls is likely going to influence the low-temperature (< 105 K) properties of thin films and heterostructures that have been grown on $SrTiO_3$ substrates.

The second study that has been conducted using the LTWPM addressed the metal-insulator transition in the correlated oxide V_2O_3. This investigation confirmed the phase separation at the metal-insulator transition that was first observed by McLeod *et al.* [173] in V_2O_3 films that have been grown on r-cut sapphire.

Furthermore, the LTWPM has been used to investigate the breakdown of the insulating phase of V_2O_3 under the application of a large enough bias current. This electrically driven breakdown of the insulating phase was studied in a temperature interval from 157 K to 169 K. It has been shown that the breakdown of the insulating phase occurs through the formation of a single metallic filament at low temperatures (< 158 K), multiple filaments and metallic domains at intermediate temperatures (159 K to 162 K), and a

dense network of metallic domains at higher temperatures (163 K to 166 K). No breakdown was observed for temperatures above 166 K, but applying currents of up to 20 mA led to a long-range switching of domains from the insulating to the metallic state. The mechanism driving this non-local switching remains to be identified. However, a long-range elastic interaction is suggested as a possible cause for the non-local switching of domains. Yet, further work needs to be performed to determine if such a long-range elastic interaction indeed is the mechanism behind this effect.

Complementary numerical simulations confirmed that the electrically driven insulator-metal transition in these devices can be explained by self-reinforced current focusing due to Joule heating and the negative temperature coefficient of the resistivity. Still, an electric-field driven breakdown, as has been predicted from theory, could be possible at higher electric-field strengths. Future work might explore the breakdown in devices of smaller size, where higher electric fields may be possible or at lower temperatures, far from the insulator-metal transition, where a thermal breakdown is less likely.

Future work will explore the phase separation and domain configuration in V_2O_3 films that have been grown on sapphire substrates with different crystallographic orientations.

List of acronyms

2DEG	two-dimensional electron gas
ac	alternating current
AFI	antiferromagnetic insulator
AFR	afocal relay
AOI	angle of incidence
AP	aperture plane
AU	airy unit
BFP	back focal plane
DAC	digital to analog converter
dc	direct current
DLC	diamond-like carbon
ESF	edge-spread function
FFT	fast Fourier transform
FSM	fast-steering mirror
IMT	insulator-metal transition
IP	image plane
IR	infrared
IV	current-voltage characteristic
LAO	lanthanum aluminate, $LaAlO_3$
LED	light-emitting diode
LTSEM	low-temperature scanning electron microscopy
LTSLM	low-temperature scanning laser microscopy
LTSPM	low-temperature scanning polarizing microscope
LTWPM	low-temperature widefield polarizing microscope
MIT	metal-insulator transition
MO	microscope objective
MOIF	magneto-optical indicator film
MOKE	magneto-optical Kerr effect

NA	numerical aperture
PEEK	polyether ether ketone
PGA	programmable gain amplifier
PI	paramagnetic insulator
PM	paramagnetic metal
PMBS	polarization maintaining beam splitter
PSF	point spread function
QPD	quadrant photodiodes
SC	superconductor
SEM	scanning electron microscopy
SEMPA	scanning electron microscopy with polarization analysis
SQUID	superconducting quantum interference device
STO	strontium titanate, $SrTiO_3$
USB	universal serial bus
WP	Wollaston prism

Bibliography

[1] H. Schmid, "Polarized Light Microscopy (PLM) of Ferroelectric and Ferroelastic Domains in Transmitted and Reflected Light", in *Ferroelectric Ceramics: Tutorial reviews, theory, processing, and applications*, edited by N. Setter and E. L. Colla (Birkhäuser Basel, Basel, 1993), pp. 107–126.

[2] H. R. Hulme, "The Faraday Effect in Ferromagnetics", Proc. Royal Soc. A **135**, 237–257 (1932).

[3] P. N. Argyres, "Theory of the Faraday and Kerr Effects in Ferromagnetics", Phys. Rev. **97**, 334–345 (1955).

[4] P. Bruno, Y. Suzuki, and C. Chappert, "Magneto-optical Kerr effect in a paramagnetic overlayer on a ferromagnetic substrate: A spin-polarized quantum size effect", Phys. Rev. B **53**, 9214–9220 (1996).

[5] P. S. Pershan, "Magneto-Optical Effects", J. Appl. Phys. **38**, 1482–1490 (1967).

[6] M. Freiser, "A Survey of Magnetooptic Effects", IEEE Trans. Magn. **4**, 152–161 (1968).

[7] J. Kerr, "On Rotation of the Plane of Polarization by Reflection from the Pole of a Magnet", Philos. Mag. **3**, 321–343 (1877).

[8] P. Weinberger, "John Kerr and his effects found in 1877 and 1878", Philos. Mag. Lett. **88**, 897–907 (2008).

[9] M. Faraday, "Experimental Researches in Electricity. Nineteenth Series", Philos. Trans. Roy. Soc. London **136**, 1–20 (1846).

[10] A. Cotton and H. Mouton, "Sur la biréfringence magnétique des liquides purs. Comparaison avec le phénomène électro-optique de Kerr", Journal de Physique Théorique et Appliquée **1**, 5–52 (1911).

[11] J. M. D. Coey, *Magnetism and Magnetic Materials* (Cambridge University Press, 2009).

[12] A. Hubert and G. Traeger, "Magneto-optical sensitivity functions of thin-film systems", J. Magn. Magn. Mater. **124**, 185–202 (1993).

[13] A. Hubert and R. Schäfer, *Magnetic Domains: The Analysis of Magnetic Microstructures* (Springer, 1998).

[14] L. Landau, J. Bell, M. Kearsley, L. Pitaevskii, E. Lifshitz, and J. Sykes, *Electrodynamics of Continuous Media*, Course of Theoretical Physics (Elsevier Science, 2013).

[15] P. Görnert, A. Lorenz, M. Lindner, and H. Richert, "Magneto-Optic Garnet Sensor Films: Preparation, Characterization, Application", in *Crystal Growth Technology* (Wiley-VCH Verlag GmbH & Co. KGaA, 2010), pp. 249–266.

[16] R. C. Jones, "A New Calculus for the Treatment of Optical Systems I. Description and Discussion of the Calculus", J. Opt. Soc. Am. **31**, 488–493 (1941).

[17] H. Hurwitz and R. C. Jones, "A New Calculus for the Treatment of Optical Systems II. Proof of Three General Equivalence Theorems", J. Opt. Soc. Am. **31**, 493–499 (1941).

[18] R. C. Jones, "A New Calculus for the Treatment of Optical Systems III. The Sohncke Theory of Optical Activity", J. Opt. Soc. Am. **31**, 500 (1941).

[19] R. C. Jones, "A New Calculus for the Treatment of Optical Systems. IV.", J. Opt. Soc. Am. **32**, 486 (1942).

[20] S. G. Moiseev, "Thin-film polarizer made of heterogeneous medium with uniformly oriented silver nanoparticles", Appl. Phys. A **103**, 775–777 (2011).

[21] J. McCord, "Progress in magnetic domain observation by advanced magneto-optical microscopy", J. Phys. D: Appl. Phys. **48**, 333001 (2015).

[22] Z. J. Yang and M. R. Scheinfein, "Combined three-axis surface magneto-optical Kerr effects in the study of surface and ultrathin-film magnetism", J. Appl. Phys. **74**, 6810–6823 (1993).

[23] C.-Y. You and S.-C. Shin, "Simplified analytic formulae for magneto-optical Kerr effects in ultrathin magnetic films", J. Magn. Magn. Mater. **198-199**, 573–577 (1999).

[24] M. Lange, S. Guénon, F. Lever, R. Kleiner, and D. Koelle, "A high-resolution combined scanning laser and widefield polarizing microscope for imaging at temperatures from 4 K to 300 K", Rev. Sci. Instrum. **88**, 123705 (2017).

[25] S. Guénon, "Cryogenic Scanning Laser Microscopy: Investigation of large BSCCO mesas and development of a polarizing microscope", PhD thesis (Universität Tübingen, 2011).

[26] Z. Erlich, Y. Frenkel, J. Drori, Y. Shperber, C. Bell, H. K. Sato, M. Hosoda, Y. Xie, Y. Hikita, H. Y. Hwang, and B. Kalisky, "Optical Study of Tetragonal Domains in $LaAlO_3/SrTiO_3$", J. Supercond. Novel Magn. **28**, 1017–1020 (2015).

[27] Z.-G. Ye and M. Dong, "Morphotropic domain structures and phase transitions in relaxor-based piezo-/ferroelectric $(1-x)Pb(Mg_{1/3}Nb_{2/3})O_3-xPbTiO_3$ single crystals", J. Appl. Phys. **87**, 2312–2319 (2000).

[28] C.-S. Tu, C.-L. Tsai, V. H. Schmidt, H. Luo, and Z. Yin, "Dielectric, hypersonic, and domain anomalies of $(PbMg_{1/3}Nb_{2/3}O_3)_{1-x}(PbTiO_3)_x$ single crystals", J. Appl. Phys. **89**, 7908–7916 (2001).

[29] F. Bitter, "Experiments on the Nature of Ferromagnetism", Phys. Rev. **41**, 507–515 (1932).

[30] J. Jakubovics et al., "Lorentz microscopy", Handbook of Microscopy **1**, 505–514 (1997).

[31] A. Tonomura, "Observation of magnetic domain structure in thin ferromagnetic films by electron holography", J. Magn. Magn. Mater. **31**, 963 –969 (1983).

[32] U. Hartmann, "Magnetic Force Microscopy", Annu. Rev. Mater. Sci. **29**, 53–87 (1999).

[33] J. R. Kirtley and J. P. Wikswo, Jr., "Scanning SQUID Microscopy", Annu. Rev. Mater. Sci. **29**, 117–148 (1999).

[34] A. M. Chang, H. D. Hallen, L. Harriott, H. F. Hess, H. L. Kao, J. Kwo, R. E. Miller, R. Wolfe, J. van der Ziel, and T. Y. Chang, "Scanning Hall probe microscopy", Appl. Phys. Lett. **61**, 1974–1976 (1992).

[35] B. J. Maertz, A. P. Wijnheijmer, G. D. Fuchs, M. E. Nowakowski, and D. D. Awschalom, "Vector magnetic field microscopy using nitrogen vacancy centers in diamond", Appl. Phys. Lett. **96**, 092504 (2010).

[36] C. Schneider, "Soft X-ray photoemission electron microscopy as an element-specific probe of magnetic microstructures", J. Magn. Magn. Mater. **175**, 160 –176 (1997).

[37] H. Akamine, S. Okumura, S. Farjami, Y. Murakami, and M. Nishida, "Imaging of surface spin textures on bulk crystals by scanning electron microscopy", Sci. Rep. **6**, 37265 (2016).

[38] M. R. Scheinfein, J. Unguris, M. H. Kelley, D. T. Pierce, and R. J. Celotta, "Scanning electron microscopy with polarization analysis (SEMPA)", Rev. Sci. Instrum. **61**, 2501–2527 (1990).

[39] J. A. Hooton and W. J. Merz, "Etch Patterns and Ferroelectric Domains in $BaTiO_3$ Single Crystals", Phys. Rev. **98**, 409–413 (1955).

[40] C. Ke, X. Wang, X. P. Hu, S. N. Zhu, and M. Qi, "Nanoparticle decoration of ferroelectric domain patterns in $LiNbO_3$ crystal", J. Appl. Phys. **101**, 064107 (2007).

[41] V. V. Aristov, L. S. Kokhanchik, and Y. I. Voronovskii, "Voltage Contrast of Ferroelectric Domains of Lithium Niobate in SEM", Phys. Status Solidi A **86**, 133–141 (1984).

[42] P. Güthner and K. Dransfeld, "Local poling of ferroelectric polymers by scanning force microscopy", Appl. Phys. Lett. **61**, 1137–1139 (1992).

[43] G. Fogarty, B. Steiner, M. Cronin-Golomb, U. Laor, M. H. Garrett, J. Martin, and R. Uhrin, "Antiparallel ferroelectric domains in photorefractive barium titanate and strontium barium niobate observed by high-resolution x-ray diffraction imaging", J. Opt. Soc. Am. B **13**, 2636–2643 (1996).

[44] P. R. Potnis, N.-T. Tsou, and J. E. Huber, "A Review of Domain Modelling and Domain Imaging Techniques in Ferroelectric Crystals", Materials **4**, 417 (2011).

[45] E. Soergel, "Visualization of ferroelectric domains in bulk single crystals", Appl. Phys. B **81**, 729–751 (2005).

[46] R. M. Grechishkin, O. V. Malyshkina, and S. S. Soshin, "Ferroic domain structure observation in polarized light using image processing techniques", Ferroelectrics **222**, 215–220 (1999).

[47] R. H. Webb, "Confocal optical microscopy", Rep. Prog. Phys. **59**, 427–471 (1996).

[48] S. Inoué and R. Oldenbourg, *Optical Instruments: Microscopes*, edited by M. Bass, Vol. 2 (McGraw-Hill, New York, 1994) Chap. 17.

[49] A. Kittel, P. Stagge, and J. Parisi, "Scanning-laser microscope for cryogenic applications", Rev. Sci. Instrum. **68**, 1286–1290 (1997).

[50] P. Li, D. Abraimov, A. Polyanskii, F. Kametani, and D. Larbalestier, "Study of grain boundary transparency in $(Yb_{1-x}Ca_x)Ba_2Cu_3O$ bicrystal thin films over a wide temperature, field, and field orientation range", Phys. Rev. B **91**, 104504 (2015).

[51] T. M. Benseman, A. E. Koshelev, V. Vlasko-Vlasov, Y. Hao, W.-K. Kwok, U. Welp, C. Keiser, B. Gross, M. Lange, D. Kölle, R. Kleiner, H. Minami, C. Watanabe, and K. Kadowaki, "Current Filamentation in Large $Bi_2Sr_2CaCu_2O_{8+\delta}$ Mesa Devices Observed via Luminescent and Scanning Laser Thermal Microscopy", Phys. Rev. Applied **3**, 044017 (2015).

[52] A. G. Sivakov, A. V. Lukashenko, D. Abraimov, P. Müller, A. V. Ustinov, and M. Leghissa, "Low-temperature scanning laser microscopy of individual filaments extracted from $(Bi,Pb)_2Sr_2Ca_2Cu_3O_{10+x}$ tapes", Appl. Phys. Lett. **76**, 2597–2599 (2000).

[53] H. B. Wang, S. Guénon, J. Yuan, A. Iishi, S. Arisawa, T. Hatano, T. Yamashita, D. Koelle, and R. Kleiner, "Hot Spots and Waves in $Bi_2Sr_2CaCu_2O_8$ Intrinsic Josephson Junction Stacks: A Study by Low Temperature Scanning Laser Microscopy", Phys. Rev. Lett. **102**, 017006 (2009).

[54] H. Kirchner, "High-Resolution Polarizing Microscope for the Observation of Magnetic Structures at Low Temperatures", Rev. Sci. Instrum. **44**, 379–382 (1973).

[55] P. E. Goa, H. Hauglin, Å. A. F. Olsen, M. Baziljevich, and T. H. Johansen, "Magneto-optical imaging setup for single vortex observation", Rev. Sci. Instrum. **74**, 141–146 (2003).

[56] D. Golubchik, E. Polturak, G. Koren, and S. G. Lipson, "A high resolution magneto-optical system for imaging of individual magnetic flux quanta", Opt. Express **17**, 16160–16165 (2009).

[57] T. Henn, T. Kiessling, W. Ossau, L. W. Molenkamp, K. Biermann, and P. V. Santos, "Ultrafast supercontinuum fiber-laser based pump-probe scanning magneto-optical Kerr effect microscope for the investigation of electron spin dynamics in semiconductors at cryogenic temperatures with picosecond time and micrometer spatial resolution", Rev. Sci. Instrum. **84**, 123903 (2013).

[58] H. Murakami and M. Tonouchi, "High-sensitive scanning laser magneto-optical imaging system", Rev. Sci. Instrum. **81**, 013701 (2010).

[59] S. Matsuzaka, Y. Ohno, and H. Ohno, "Scanning Kerr Microscopy of the Spin Hall Effect in n-Doped GaAs with Various Doping Concentration", J. Supercond. Novel Magn. **23**, 37 (2010).

[60] F. Lever, "Untersuchung von Bismuth-substituierten Yttrium-Eisengranatfilmen zur magnetooptischen Abbildung von Flussstrukturen in Supraleitern", Zulassungsarbeit (Eberhard Karls Universität Tübingen, 2016).

[61] A. Köhler, "Ein neues Beleuchtungsverfahren für mikrophotographische Zwecke", Z. Wiss. Mikrosk. Mikroskopisc. Tech **10**, 433–440 (1893).

[62] I. V. Soldatov and R. Schäfer, "Advances in quantitative Kerr microscopy", Phys. Rev. B **95**, 014426 (2017).

[63] I. V. Soldatov and R. Schäfer, "Selective sensitivity in Kerr microscopy", Rev. Sci. Instrum. **88**, 073701 (2017).

[64] A. Stupakiewicz, A. Chizhik, M. Tekielak, A. Zhukov, J. Gonzalez, and A. Maziewski, "Direct imaging of the magnetization reversal in microwires using all-MOKE microscopy", Rev. Sci. Instrum. **85**, 103702 (2014).

[65] M. I. Shribak, S. Inoué, and R. Oldenbourg, "Polarization aberrations caused by differential transmission and phase shift in high-numerical-aperture lenses: theory, measurement, and rectification", Opt. Eng. **41**, 943–954 (2002).

[66] J. Montagu, "Galvanometric and Resonant Scanners", in *Handbook of Optical and Laser-Scanning, Second Edition* (CRC Press, 2011), pp. 393–448.

[67] X. Lv, C. Zhan, S. Zeng, W. R. Chen, and Q. Luo, "Construction of multiphoton laser scanning microscope based on dual-axis acousto-optic deflector", Rev. Sci. Instrum. **77**, 046101 (2006).

[68] G. L. Ping, C. W. See, M. G. Somekh, M. B. Suddendorf, J. H. Vincent, and P. K. Footner, "A Fast-Scanning Optical Microscope for Imaging Magnetic Domain Structures", Scanning **18**, 8–12 (1995).

[69] G. Anzolin, A. Gardelein, M. Jofre, G. Molina-Terriza, and M. W. Mitchell, "Polarization change induced by a galvanometric optical scanner", J. Opt. Soc. Am. A **27**, 1946 (2010).

[70] A. C. Ribes, S. Damaskinos, and A. E. Dixon, "Inexpensive, High-Quality Optical Relay for Use in Confocal Scanning Beam Imaging", Scanning **22**, 282–287 (2000).

[71] A. Negrean and H. D. Mansvelder, "Optimal lens design and use in laser-scanning microscopy", Biomed. Opt. Express **5**, 1588–1609 (2014).

[72] M. Laikin, *Lens Design, Fourth Edition* (CRC Press, 2006).

[73] *Zemax OpticStudio*, Zemax, LLC, Kirkland, Washington, United States.

[74] P. Vavassori, "Polarization modulation technique for magneto-optical quantitative vector magnetometry", Appl. Phys. Lett. **77**, 1605–1607 (2000).

[75] H. Hornauer, T. M. Atmono, and K. Röll, "A Kerr Magnetometer using Faraday Modulation Technique", J. Magn. Magn. Mater. **83**, 551 –552 (1990).

[76] M. Cormier, J. Ferré, A. Mougin, J.-P. Cromières, and V. Klein, "High resolution polar Kerr magnetometer for nanomagnetism and nanospintronics", Rev. Sci. Instrum. **79**, 033706 (2008).

[77] P. Kasiraj, R. M. Shelby, J. S. Best, and D. E. Horne, "Magnetic domain imaging with a scanning Kerr effect microscope", IEEE Trans. Magn. **22**, 837–839 (1986).

[78] L. Flajšman, M. Urbánek, V. Křižáková, M. Vaňatka, I. Turčan, and T. Šikola, "High-resolution fully vectorial scanning Kerr magnetometer", Rev. Sci. Instrum. **87**, 053704 (2016).

[79] S. Spielman, K. Fesler, C. B. Eom, T. H. Geballe, M. M. Fejer, and A. Kapitulnik, "Test for Nonreciprocal Circular Birefringence in $YBa_2Cu_3O_7$ Thin Films as Evidence for Broken Time-Reversal Symmetry", Phys. Rev. Lett. **65**, 123–126 (1990).

[80] J. Xia, P. T. Beyersdorf, M. M. Fejer, and A. Kapitulnik, "Modified Sagnac interferometer for high-sensitivity magneto-optic measurements at cryogenic temperatures", Appl. Phys. Lett. **89**, 062508 (2006).

[81] W. W. Clegg, N. A. E. Heyes, E. W. Hill, and C. D. Wright, "Development of a scanning laser microscope for magneto-optic studies of thin magnetic films", J. Magn. Magn. Mater. **95**, 49 –57 (1991).

[82] H. Ding, S. Pütter, H. Oepen, and J. Kirschner, "Experimental method for separating longitudinal and polar Kerr signals", J. Magn. Magn. Mater. **212**, 5 –11 (2000).

[83] P. L. Stöhr and R. P. Huebener, "Two-Dimensional Imaging of the Resistive Voltage Changes in a Superconductor Caused by Irradiation with an Electron Beam", J. Low Temp. Phys. **37**, 277–287 (1979).

[84] J. R. Clem and R. P. Huebener, "Application of low-temperature scanning electron microscopy to superconductors", J. Appl. Phys. **51**, 2764–2773 (1980).

[85] R. P. Huebener, "Scanning Electron Microscopy at Very Low Temperatures", Advances in Electronics and Electron Physics **70**, 1 –78 (1988).

[86] R. Gross and D. Koelle, "Low temperature scanning electron microscopy of superconducting thin films and Josephson junctions", Rep. Prog. Phys. **57**, 651 (1994).

[87] Y. Y. Divin, F. Y. Nad', V. Y. Pokrovski, and P. M. Shadrin, "Laser probing of high-T_c superconducting thin films", IEEE Trans. Magn. **27**, 1101–1104 (1991).

[88] Y. Y. Divin and P. M. Shadrin, "Imaging of electrical inhomogeneities in $YBa_2Cu_3O_{7-x}$ thin-film structures by room-temperature laser scanning microscopy", Physica C **232**, 257 –262 (1994).

[89] N. Dieckmann, S. Friemel, A. Bock, U. Merkt, R. Gerber, and R. P. Huebener, "Equivalence of LTSLM and LTSEM analyses: study of a $YBa_2Cu_3O_7$ multi-layer device", Physica C **292**, 133 –139 (1997).

[90] A. G. Sivakov, A. P. Zhuravel', O. G. Turutanov, and I. M. Dmitrenko, "Spatially resolved characterization of superconducting films and cryoelectronic devices by means of low temperature scanning laser microscope", Appl. Surf. Sci. **106**, 390 –395 (1996).

[91] R. Werner, A. Y. Aladyshkin, I. M. Nefedov, A. V. Putilov, M. Kemmler, D. Bothner, A. Loerincz, K. Ilin, M. Siegel, R. Kleiner, and D. Koelle, "Edge superconductivity in Nb thin film microbridges revealed by electric transport measurements and visualized by scanning laser microscopy", Supercond. Sci. Technol. **26**, 095011 (2013).

[92] A. A. Shashkin, A. J. Kent, J. R. Owers-Bradley, A. J. Cross, P. Hawker, and M. Henini, "Hall Photovoltage Imaging of the Edge of a Quantum Hall Device", Phys. Rev. Lett. **79**, 5114–5117 (1997).

[93] M. Wagenknecht, H. Eitel, T. Nachtrab, J. B. Philipp, R. Gross, R. Kleiner, and D. Koelle, "Laser Microscopy of Tunneling Magnetoresistance in Manganite Grain-Boundary Junctions", Phys. Rev. Lett. **96**, 047203 (2006).

[94] R. Werner, M. Weiler, A. Y. Petrov, B. A. Davidson, R. Gross, R. Kleiner, S. T. B. Goennenwein, and D. Koelle, "Local tunneling magnetoresistance probed by low-temperature scanning laser microscopy", Appl. Phys. Lett. **99**, 182513 (2011).

[95] M. Weiler, M. Althammer, F. D. Czeschka, H. Huebl, M. S. Wagner, M. Opel, I.-M. Imort, G. Reiss, A. Thomas, R. Gross, and S. T. B. Goennenwein, "Local Charge and Spin Currents in Magnetothermal Landscapes", Phys. Rev. Lett. **108**, 106602 (2012).

[96] A. P. Zhuravel, A. G. Sivakov, O. G. Turutanov, A. N. Omelyanchouk, S. M. Anlage, A. Lukashenko, A. V. Ustinov, and D. Abraimov, "Laser scanning microscopy of HTS films and devices (Review Article)", Low Temp. Phys. **32**, 592–607 (2006).

[97] A. P. Zhuravel, A. V. Ustinov, D. Abraimov, and S. M. Anlage, "Imaging Local Sources of Intermodulation in Superconducting Microwave Devices", IEEE Trans. Appl. Supercond. **13**, 340–343 (2003).

[98] J. Schindelin, I. Arganda-Carreras, E. Frise, V. Kaynig, M. Longair, T. Pietzsch, S. Preibisch, C. Rueden, S. Saalfeld, B. Schmid, J.-Y. Tinevez, D. J. White, V. Hartenstein, K. Eliceiri, P. Tomancak, and A. Cardona, "Fiji: an open-source platform for biological-image analysis", Nat. Methods **9**, 676–682 (2012).

[99] P. Thévenaz, U. Ruttimann, and M. Unser, "A pyramid approach to subpixel registration based on intensity", IEEE Trans. Image Process. **7**, 27–41 (1998).

[100] Z. Yang, M. Lange, A. Volodin, R. Szymczak, and V. V. Moshchalkov, "Domain-wall superconductivity in superconductor-ferromagnet hybrids", Nat. Mater. **3**, 793–798 (2004).

[101] Z. Yang, K. Vervaeke, V. V. Moshchalkov, and R. Szymczak, "Modulation of superconductivity by a magnetic template in Nb/$BaFe_{12}O_{19}$ hybrids", Phys. Rev. B **73**, 224509 (2006).

[102] Z. Yang, J. Fritzsche, and V. V. Moshchalkov, "Guided nucleation of superconductivity in Nb/$BaFe_{12}O_{19}$ hybrids with different domain patterns", Appl. Phys. Lett. **98**, 012505 (2011).

[103] J. Fritzsche, V. V. Moshchalkov, H. Eitel, D. Koelle, R. Kleiner, and R. Szymczak, "Local Observation of Reverse-Domain Superconductivity in a Superconductor-Ferromagnet Hybrid", Phys. Rev. Lett. **96**, 247003 (2006).

[104] R. Werner, A. Y. Aladyshkin, S. Guénon, J. Fritzsche, I. M. Nefedov, V. V. Moshchalkov, R. Kleiner, and D. Koelle, "Domain-wall and reverse-domain superconducting states of a Pb thin-film bridge on a ferromagnetic $BaFe_{12}O_{19}$ single crystal", Phys. Rev. B **84**, 020505 (2011).

[105] A. Abrikosov, "The magnetic properties of superconducting alloys", J. Phys. Chem. Solids **2**, 199–208 (1957).

[106] C. P. Bean, "Magnetization of High-Field Superconductors", Rev. Mod. Phys. **36**, 31–39 (1964).

[107] W. T. Norris, "Calculation of hysteresis losses in hard superconductors carrying ac: isolated conductors and edges of thin sheets", J. Phys. D: Appl. Phys. **3**, 489–507 (1970).

[108] E. H. Brandt and M. Indenbom, "Type-II-superconductor strip with current in a perpendicular magnetic field", Phys. Rev. B **48**, 12893–12906 (1993).

[109] T. H. Johansen and D. V. Shantsev, *Magneto-Optical Imaging*, Nato Science Series II: Mathematics, Physics and Chemistry - Vol. 142 (Springer Netherlands, 2004).

[110] I. S. Veshchunov, W. Magrini, S. V. Mironov, A. G. Godin, J.-B. Trebbia, A. I. Buzdin, P. Tamarat, and B. Lounis, "Optical manipulation of single flux quanta", Nat. Commun. **7**, 12801 (2016).

[111] G. Carneiro and E. H. Brandt, "Vortex lines in films: Fields and interactions", Phys. Rev. B **61**, 6370–6376 (2000).

[112] T. Luibrand, "Abbildung von magnetischen Flussstrukturen mittels magneto-optischem Faraday-Effekt, Zulassungsarbeit" (Eberhard Karls Universität Tübingen, 2018).

[113] E. C. Stoner and E. P. Wohlfarth, "A Mechanism of Magnetic Hysteresis in Heterogeneous Alloys", Philos. Trans. Royal Soc. A **240**, 599–642 (1948).

[114] P. Hansen, K. Witter, and W. Tolksdorf, "Magnetic and magneto-optic properties of lead- and bismuth-substituted yttrium iron garnet films", Phys. Rev. B **27**, 6608–6625 (1983).

[115] D. Bothner, T. Gaber, M. Kemmler, D. Koelle, and R. Kleiner, "Improving the performance of superconducting microwave resonators in magnetic fields", Appl. Phys. Lett. **98**, 102504 (2011).

[116] D. Bothner, C. Clauss, E. Koroknay, M. Kemmler, T. Gaber, M. Jetter, M. Scheffler, P. Michler, M. Dressel, D. Koelle, and R. Kleiner, "The phase boundary of superconducting niobium thin films with antidot arrays fabricated with microsphere photolithography", Supercond. Sci. Technol. **25**, 065020 (2012).

[117] D. Bothner, T. Gaber, M. Kemmler, D. Koelle, R. Kleiner, S. Wünsch, and M. Siegel, "Magnetic hysteresis effects in superconducting coplanar microwave resonators", Phys. Rev. B **86**, 014517 (2012).

[118] J. Brisbois, O.-A. Adami, J. I. Avila, M. Motta, W. A. Ortiz, N. D. Nguyen, P. Vanderbemden, B. Vanderheyden, R. B. G. Kramer, and A. V. Silhanek, "Magnetic flux penetration in Nb superconducting films with lithographically defined microindentations", Phys. Rev. B **93**, 054521 (2016).

[119] H. J. H. Ma, S. Scharinger, S. W. Zeng, D. Kohlberger, M. Lange, A. Stöhr, X. R. Wang, T. Venkatesan, R. Kleiner, J. F. Scott, J. M. D. Coey, D. Koelle, and Ariando, "Local Electrical Imaging of Tetragonal Domains and Field-Induced Ferroelectric Twin Walls in Conducting $SrTiO_3$", Phys. Rev. Lett. **116**, 257601 (2016).

[120] E. K. H. Salje, "Domain boundary engineering – recent progress and many open questions", Phase Transitions **86**, 1–13 (2013).

[121] P. A. Fleury, J. F. Scott, and J. M. Worlock, "Soft Phonon Modes and the 110°K Phase Transition in $SrTiO_3$", Phys. Rev. Lett. **21**, 16–19 (1968).

[122] R. A. Cowley, "Lattice Dynamics and Phase Transitions of Strontium Titanate", Phys. Rev. **134**, A981–A997 (1964).

[123] J. F. Scott, E. K. H. Salje, and M. A. Carpenter, "Domain Wall Damping and Elastic Softening in $SrTiO_3$: Evidence for Polar Twin Walls", Phys. Rev. Lett. **109**, 187601 (2012).

[124] E. K. H. Salje, O. Aktas, M. A. Carpenter, V. V. Laguta, and J. F. Scott, "Domains within Domains and Walls within Walls: Evidence for Polar Domains in Cryogenic $SrTiO_3$", Phys. Rev. Lett. **111**, 247603 (2013).

[125] Y. Frenkel, N. Haham, Y. Shperber, C. Bell, Y. Xie, Z. Chen, Y. Hikita, H. Y. Hwang, E. K. H. Salje, and B. Kalisky, "Imaging and tuning polarity at $SrTiO_3$ domain walls", Nat. Mater. **16**, 1203–1208 (2017).

[126] J. Hemberger, M. Nicklas, R. Viana, P. Lunkenheimer, A. Loidl, and R. Böhmer, "Quantum paraelectric and induced ferroelectric states in $SrTiO_3$", J. Phys.: Condens. Matter **8**, 4673–4690 (1996).

[127] K. A. Müller and H. Burkard, "$SrTiO_3$: An intrinsic quantum paraelectric below 4 K", Phys. Rev. B **19**, 3593–3602 (1979).

[128] S. E. Rowley, L. J. Spalek, R. P. Smith, M. P. M. Dean, M. Itoh, J. F. Scott, G. G. Lonzarich, and S. S. Saxena, "Ferroelectric quantum criticality", Nat. Phys. **10**, 367–372 (2014).

[129] J. Sidoruk, J. Leist, H. Gibhardt, M. Meven, K. Hradil, and G. Eckold, "Quantitative determination of domain distribution in $SrTiO_3$—competing effects of applied electric field and mechanical stress", J. Phys.: Condens. Matter **22**, 235903 (2010).

[130] E. Hegenbarth, "Die Feldstärkeabhängigkeit der Dielektrizitätskonstanten von $SrTiO_3$-Einkristallen im Temperaturbereich von 15 bis 80 °K", Phys. Status Solidi B **6**, 333–337 (1964).

[131] T. Zykova-Timan and E. K. H. Salje, "Highly mobile vortex structures inside polar twin boundaries in $SrTiO_3$", Appl. Phys. Lett. **104**, 082907 (2014).

[132] A. Ohtomo and H. Y. Hwang, "A high-mobility electron gas at the $LaAlO_3/SrTiO_3$ heterointerface", Nature **427**, 423–426 (2004).

[133] N. Nakagawa, H. Y. Hwang, and D. A. Muller, "Why some interfaces cannot be sharp", Nat. Mater. **5**, 204–209 (2006).

[134] Z. S. Popović, S. Satpathy, and R. M. Martin, "Origin of the Two-Dimensional Electron Gas Carrier Density at the $LaAlO_3$ on $SrTiO_3$ Interface", Phys. Rev. Lett. **101**, 256801 (2008).

[135] R. Pentcheva and W. E. Pickett, "Avoiding the Polarization Catastrophe in $LaAlO_3$ Overlayers on $SrTiO_3$(001) through Polar Distortion", Phys. Rev. Lett. **102**, 107602 (2009).

[136] A. Kalabukhov, R. Gunnarsson, J. Börjesson, E. Olsson, T. Claeson, and D. Winkler, "Effect of oxygen vacancies in the $SrTiO_3$ substrate on the electrical properties of the $LaAlO_3/SrTiO_3$ interface", Phys. Rev. B **75**, 121404 (2007).

[137] W. Siemons, G. Koster, H. Yamamoto, W. A. Harrison, G. Lucovsky, T. H. Geballe, D. H. A. Blank, and M. R. Beasley, "Origin of Charge Density at $LaAlO_3$ on $SrTiO_3$ Heterointerfaces: Possibility of Intrinsic Doping", Phys. Rev. Lett. **98**, 196802 (2007).

[138] G. Herranz, M. Basletić, M. Bibes, C. Carrétéro, E. Tafra, E. Jacquet, K. Bouzehouane, C. Deranlot, A. Hamzić, J.-M. Broto, A. Barthélémy, and A. Fert, "High Mobility in $LaAlO_3/SrTiO_3$ Heterostructures: Origin, Dimensionality, and Perspectives", Phys. Rev. Lett. **98**, 216803 (2007).

[139] P. R. Willmott, S. A. Pauli, R. Herger, C. M. Schlepütz, D. Martoccia, B. D. Patterson, B. Delley, R. Clarke, D. Kumah, C. Cionca, and Y. Yacoby, "Structural Basis for the Conducting Interface between $LaAlO_3$ and $SrTiO_3$", Phys. Rev. Lett. **99**, 155502 (2007).

[140] N. Reyren, S. Thiel, A. D. Caviglia, L. F. Kourkoutis, G. Hammerl, C. Richter, C. W. Schneider, T. Kopp, A.-S. Ruetschi, D. Jaccard, M. Gabay, D. A. Muller, J.-M. Triscone, and J. Mannhart, "Superconducting Interfaces Between Insulating Oxides", Science **317**, 1196–1199 (2007).

[141] S. Gariglio, N. Reyren, A. D. Caviglia, and J.-M. Triscone, "Superconductivity at the $LaAlO_3/SrTiO_3$ interface", J. Phys.: Condens. Matter **21**, 164213 (2009).

[142] A. Brinkman, M. Huijben, M. van Zalk, J. Huijben, U. Zeitler, J. C. Maan, W. G. van der Wiel, G. Rijnders, D. H. A. Blank, and H. Hilgenkamp, "Magnetic effects at the interface between non-magnetic oxides", Nat. Mater. **6**, 493–496 (2007).

[143] J. A. Bert, B. Kalisky, C. Bell, M. Kim, Y. Hikita, H. Y. Hwang, and K. A. Moler, "Direct imaging of the coexistence of ferromagnetism and superconductivity at the $LaAlO_3/SrTiO_3$ interface", Nat. Phys. **7**, 767–771 (2011).

[144] B. Kalisky, J. A. Bert, B. B. Klopfer, C. Bell, H. K. Sato, M. Hosoda, Y. Hikita, H. Y. Hwang, and K. A. Moler, "Critical thickness for ferromagnetism in $LaAlO_3/SrTiO_3$ heterostructures", Nat. Commun. **3**, 922 (2012).

[145] B. Kalisky, E. M. Spanton, H. Noad, J. R. Kirtley, K. C. Nowack, C. Bell, H. K. Sato, M. Hosoda, Y. Xie, Y. Hikita, C. Woltmann, G. Pfanzelt, R. Jany, C. Richter, H. Y. Hwang, J. Mannhart, and K. A. Moler, "Locally enhanced conductivity due to the tetragonal domain structure in $LaAlO_3/SrTiO_3$ heterointerfaces", Nat. Mater. **12**, 1091–1095 (2013).

[146] M. Honig, J. A. Sulpizio, J. Drori, A. Joshua, E. Zeldov, and S. Ilani, "Local electrostatic imaging of striped domain order in $LaAlO_3/SrTiO_3$", Nat. Mater. **12**, 1112–1118 (2013).

[147] Ariando, X. Wang, G. Baskaran, Z. Q. Liu, J. Huijben, J. B. Yi, A. Annadi, A. R. Barman, A. Rusydi, S. Dhar, Y. P. Feng, J. Ding, H. Hilgenkamp, and T. Venkatesan, "Electronic phase separation at the $LaAlO_3/SrTiO_3$ interface", Nat. Commun. **2**, 188 (2011).

[148] H. J. H. Ma, Z. Huang, W. M. Lü, A. Annadi, S. W. Zeng, L. M. Wong, S. J. Wang, T. Venkatesan, and Ariando, "Tunable bilayer two-dimensional electron gas in $LaAlO_3/SrTiO_3$ superlattices", Appl. Phys. Lett. **105**, 011603 (2014).

[149] M. A. Geday and A. M. Glazer, "Birefringence of $SrTiO_3$ at the ferroelastic phase transition", J. Phys.: Condens. Matter **16**, 3303 (2004).

[150] D. Schwebius, "Untersuchung des Metall-Isolator-Übergangs in V_2O_3 mit einem kombinierten Weitfeld-Polarisations- und konfokalen Laserraster-Mikroskop", MA thesis (Eberhard-Karls-Universität Tübingen, 2018).

[151] M. Imada, A. Fujimori, and Y. Tokura, "Metal-insulator transitions", Rev. Mod. Phys. **70**, 1039–1263 (1998).

[152] P. Hansmann, A. Toschi, G. Sangiovanni, T. Saha-Dasgupta, S. Lupi, M. Marsi, and K. Held, "Mott-Hubbard transition in V_2O_3 revisited", Phys. Status Solidi B **250**, 1251–1264 (2013).

[153] M. J. Rozenberg, G. Kotliar, H. Kajueter, G. A. Thomas, D. H. Rapkine, J. M. Honig, and P. Metcalf, "Optical Conductivity in Mott-Hubbard Systems", Phys. Rev. Lett. **75**, 105–108 (1995).

[154] P. Limelette, A. Georges, D. Jérome, P. Wzietek, P. Metcalf, and J. M. Honig, "Universality and Critical Behavior at the Mott Transition", Science **302**, 89–92 (2003).

[155] D. B. McWhan and J. P. Remeika, "Metal-Insulator Transition in $(V_{1-x}Cr_x)_2O_3$", Phys. Rev. B **2**, 3734–3750 (1970).

[156] F. Rodolakis, P. Hansmann, J.-P. Rueff, A. Toschi, M. W. Haverkort, G. Sangiovanni, A. Tanaka, T. Saha-Dasgupta, O. K. Andersen, K. Held, M. Sikora, I. Alliot, J.-P. Itié, F. Baudelet, P. Wzietek, P. Metcalf, and M. Marsi, "Inequivalent Routes across the Mott Transition in V_2O_3 Explored by X-Ray Absorption", Phys. Rev. Lett. **104**, 047401 (2010).

[157] S. Lupi, L. Baldassarre, B. Mansart, A. Perucchi, A. Barinov, P. Dudin, E. Papalazarou, F. Rodolakis, J.-P. Rueff, J.-P. Itié, S. Ravy, D. Nicoletti, P. Postorino, P. Hansmann, N. Parragh, A. Toschi, T. Saha-Dasgupta, O. K. Andersen, G. Sangiovanni, K. Held, and M. Marsi, "A microscopic view on the Mott transition in chromium-doped V_2O_3", Nat. Commun. **1**, 105 (2010).

[158] P. Hansmann, M. W. Haverkort, A. Toschi, G. Sangiovanni, F. Rodolakis, J.-P. Rueff, M. Marsi, and K. Held, "Atomic and itinerant effects at the transition-metal x-ray absorption K pre-edge exemplified in the case of V_2O_3", Phys. Rev. B **85**, 115136 (2012).

[159] J.-H. Park, L. H. Tjeng, A. Tanaka, J. W. Allen, C. T. Chen, P. Metcalf, J. M. Honig, F. M. F. de Groot, and G. A. Sawatzky, "Spin and orbital occupation and phase transitions in V_2O_3", Phys. Rev. B **61**, 11506–11509 (2000).

[160] A. I. Poteryaev, J. M. Tomczak, S. Biermann, A. Georges, A. I. Lichtenstein, A. N. Rubtsov, T. Saha-Dasgupta, and O. K. Andersen, "Enhanced crystal-field splitting and orbital-selective coherence induced by strong correlations in V_2O_3", Phys. Rev. B **76**, 085127 (2007).

[161] M. K. Stewart, D. Brownstead, S. Wang, K. G. West, J. G. Ramirez, M. M. Qazilbash, N. B. Perkins, I. K. Schuller, and D. N. Basov, "Insulator-to-metal transition and correlated metallic state of V_2O_3 investigated by optical spectroscopy", Phys. Rev. B **85**, 205113 (2012).

[162] S. Y. Ezhov, V. I. Anisimov, D. I. Khomskii, and G. A. Sawatzky, "Orbital Occupation, Local Spin, and Exchange Interactions in V_2O_3", Phys. Rev. Lett. **83**, 4136–4139 (1999).

[163] Y. Guo, S. J. Clark, and J. Robertson, "Calculation of metallic and insulating phases of V_2O_3 by hybrid density functionals", J. Chem. Phys. **140**, 054702 (2014).

[164] M. M. Qazilbash, A. A. Schafgans, K. S. Burch, S. J. Yun, B. G. Chae, B. J. Kim, H. T. Kim, and D. N. Basov, "Electrodynamics of the vanadium oxides VO_2 and V_2O_3", Phys. Rev. B **77**, 115121 (2008).

[165] J. Sakai, P. Limelette, and H. Funakubo, "Transport properties and c/a ratio of V_2O_3 thin films grown on C- and R-plane sapphire substrates by pulsed laser deposition", Appl. Phys. Lett. **107**, 241901 (2015).

[166] S. Autier-Laurent, B. Mercey, D. Chippaux, P. Limelette, and C. Simon, "Strain-induced pressure effect in pulsed laser deposited thin films of the strongly correlated oxide V_2O_3", Phys. Rev. B **74**, 195109 (2006).

[167] J. Brockman, M. G. Samant, K. P. Roche, and S. S. P. Parkin, "Substrate-induced disorder in V_2O_3 thin films grown on annealed c-plane sapphire substrates", Appl. Phys. Lett. **101**, 051606 (2012).

[168] S. Yonezawa, Y. Muraoka, Y. Ueda, and Z. Hiroi, "Epitaxial strain effects on the metal–insulator transition in V_2O_3 thin films", Solid State Commun. **129**, 245–248 (2004).

[169] H. Schuler, S. Klimm, G. Weissmann, C. Renner, and S. Horn, "Influence of strain on the electronic properties of epitaxial V_2O_3 thin films", Thin Solid Films **299**, 119–124 (1997).

[170] C. B. Muratov, "Theory of domain patterns in systems with long-range interactions of Coulomb type", Phys. Rev. E **66**, 066108 (2002).

[171] A. Macridin, M. Jarrell, and T. Maier, "Phase separation in the Hubbard model using the dynamical cluster approximation", Phys. Rev. B **74**, 085104 (2006).

[172] C.-H. Yee and L. Balents, "Phase Separation in Doped Mott Insulators", Phys. Rev. X **5**, 021007 (2015).

[173] A. S. McLeod, E. van Heumen, J. G. Ramirez, S. Wang, T. Saerbeck, S. Guénon, M. Goldflam, L. Anderegg, P. Kelly, A. Mueller, M. K. Liu, I. K. Schuller, and D. N. Basov, "Nanotextured phase coexistence in the correlated insulator V_2O_3", Nat. Phys. **13**, 80–86 (2016).

[174] M. Seul and D. Andelman, "Domain Shapes and Patterns: The Phenomenology of Modulated Phases", Science **267**, 476–483 (1995).

[175] A. M. Bratkovsky, S. C. Marais, V Heine, and E. K. H. Salje, "The theory of fluctuations and texture embryos in structural phase transitions mediated by strain", J. Phys.: Condens. Matter **6**, 3679–3696 (1994).

[176] Y. F. Gao, W. Lu, and Z. Suo, "A mesophase transition in a binary monolayer on a solid surface", Acta Mater. **50**, 2297–2308 (2002).

[177] M. K. Liu, M. Wagner, E. Abreu, S. Kittiwatanakul, A. McLeod, Z. Fei, M. Goldflam, S. Dai, M. M. Fogler, J. Lu, S. A. Wolf, R. D. Averitt, and D. N. Basov, "Anisotropic Electronic State via Spontaneous Phase Separation in Strained Vanadium Dioxide Films", Phys. Rev. Lett. **111**, 096602 (2013).

[178] B. Spivak and S. A. Kivelson, "Transport in two dimensional electronic micro-emulsions", Ann. Phys. **321**, 2071–2115 (2006).

[179] L. Baldassarre, A. Perucchi, D. Nicoletti, A. Toschi, G. Sangiovanni, K. Held, M. Capone, M. Ortolani, L. Malavasi, M. Marsi, P. Metcalf, P. Postorino, and S. Lupi, "Quasiparticle evolution and pseudogap formation in V_2O_3: An infrared spectroscopy study", Phys. Rev. B **77**, 113107 (2008).

[180] Z. Yang, C. Ko, and S. Ramanathan, "Oxide Electronics Utilizing Ultrafast Metal-Insulator Transitions", Annu. Rev. Mater. Res. **41**, 337–367 (2011).

[181] J. del Valle, Y. Kalcheim, J. Trastoy, A. Charnukha, D. N. Basov, and I. K. Schuller, "Electrically Induced Multiple Metal-Insulator Transitions in Oxide Nanodevices", Phys. Rev. Appl **8**, 054041 (2017).

[182] E. Janod, J. Tranchant, B. Corraze, M. Querré, P. Stoliar, M. Rozenberg, T. Cren, D. Roditchev, V. T. Phuoc, M.-P. Besland, and L. Cario, "Resistive Switching in Mott Insulators and Correlated Systems", Adv. Funct. Mater. **25**, 6287–6305 (2015).

[183] P. Markov, R. E. Marvel, H. J. Conley, K. J. Miller, R. F. Haglund, and S. M. Weiss, "Optically Monitored Electrical Switching in VO_2", ACS Photonics **2**, 1175–1182 (2015).

[184] I. K. Schuller and R. Stevens, "Neuromorphic computing: From materials to systems architecture", U.S. Department of Energy (2015).

[185] P. Stoliar, J. Tranchant, B. Corraze, E. Janod, M.-P. Besland, F. Tesler, M. Rozenberg, and L. Cario, "A Leaky-Integrate-and-Fire Neuron Analog Realized with a Mott Insulator", Adv. Funct. Mater. **27**, 1604740 (2017).

[186] M. D. Pickett, G. Medeiros-Ribeiro, and R. S. Williams, "A scalable neuristor built with Mott memristors", Nat. Mater. **12**, 114–117 (2013).

[187] M. Eckstein, T. Oka, and P. Werner, "Dielectric Breakdown of Mott Insulators in Dynamical Mean-Field Theory", Phys. Rev. Lett. **105**, 146404 (2010).

[188] F. Heidrich-Meisner, I. González, K. A. Al-Hassanieh, A. E. Feiguin, M. J. Rozenberg, and E. Dagotto, "Nonequilibrium electronic transport in a one-dimensional Mott insulator", Phys. Rev. B **82**, 205110 (2010).

[189] W.-R. Lee and K. Park, "Dielectric breakdown via emergent nonequilibrium steady states of the electric-field-driven Mott insulator", Phys. Rev. B **89**, 205126 (2014).

[190] N. Sugimoto, S. Onoda, and N. Nagaosa, "Field-induced metal-insulator transition and switching phenomenon in correlated insulators", Phys. Rev. B **78**, 155104 (2008).

[191] G. Mazza, A. Amaricci, M. Capone, and M. Fabrizio, "Field-Driven Mott Gap Collapse and Resistive Switch in Correlated Insulators", Phys. Rev. Lett. **117**, 176401 (2016).

[192] E. Spenke, "Eine anschauliche Deutung der Abzweigtemperatur scheibenförmiger Heißleiter", Archiv f. Elektrotechnik **30**, 728 (1936).

[193] E. Spenke, "Zur technischen Beherrschung des Wärmedurchschlages von Heißleitern", Wissenschaftliche Veröffentlichungen aus den Siemens-Werken, 92 (1936).

[194] S. Guénon, S. Scharinger, S. Wang, J. G. Ramírez, D. Koelle, R. Kleiner, and I. K. Schuller, "Electrical breakdown in a V_2O_3 device at the insulator-to-metal transition", EPL **101**, 57003 (2013).

[195] J. S. Brockman, L. Gao, B. Hughes, C. T. Rettner, M. G. Samant, K. P. Roche, and S. S. P. Parkin, "Subnanosecond incubation times for electric-field-induced metallization of a correlated electron oxide", Nat. Nanotechnol. **9**, 453–458 (2014).

[196] C. Berglund, "Thermal Filaments in Vanadium Dioxide", IEEE Trans. Electron Devices **16**, 432–437 (1969).

[197] J. Duchene, M. Terraillon, P. Pailly, and G. Adam, "Filamentary Conduction in VO_2 Coplanar Thin-Film Devices", Appl. Phys. Lett. **19**, 115–117 (1971).

[198] A. Zimmers, L. Aigouy, M. Mortier, A. Sharoni, S. Wang, K. G. West, J. G. Ramirez, and I. K. Schuller, "Role of Thermal Heating on the Voltage Induced Insulator-Metal Transition in VO_2", Phys. Rev. Lett. **110**, 056601 (2013).

[199] K. Okimura, N. Ezreena, Y. Sasakawa, and J. Sakai, "Electric-Field-Induced Multistep Resistance Switching in Planar VO_2/*c*-Al_2O_3 Structure", Jpn. J. Appl. Phys. **48**, 065003 (2009).

[200] S. N. G. Corder, J. Jiang, X. Chen, S. Kittiwatanakul, I.-C. Tung, Y. Zhu, J. Zhang, H. A. Bechtel, M. C. Martin, G. L. Carr, J. Lu, S. A. Wolf, H. Wen, T. H. Tao, and M. Liu, "Controlling phase separation in vanadium dioxide thin films via substrate engineering", Phys. Rev. B **96**, 161110 (2017).

[201] J. Wu, Q. Gu, B. S. Guiton, N. P. de Leon, L. Ouyang, and H. Park, "Strain-Induced Self Organization of Metal-Insulator Domains in Single-Crystalline VO_2 Nanobeams", Nano Lett. **6**, 2313–2317 (2006).

[202] H. Garcke and U. Weikard, "Numerical approximation of the Cahn-Larché equation", Numer. Math. **100**, 639–662 (2005).

[203] S.-K. Mo, J. D. Denlinger, H.-D. Kim, J.-H. Park, J. W. Allen, A. Sekiyama, A. Yamasaki, K. Kadono, S. Suga, Y. Saitoh, T. Muro, P. Metcalf, G. Keller, K. Held, V. Eyert, V. I. Anisimov, and D. Vollhardt, "Prominent Quasiparticle Peak in the Photoemission Spectrum of the Metallic Phase of V_2O_3", Phys. Rev. Lett. **90**, 186403 (2003).

[204] E. R. Dobrovinskaya, L. A. Lytvynov, and V. Pishchik, *Sapphire: Material, Manufacturing, Applications (Micro- and Opto-Electronic Materials, Structures, and Systems)* (Springer, 2010).

[205] V. N. Andreev, F. A. Chudnovskii, A. V. Petrov, and E. I. Terukov, "Thermal conductivity of VO_2, V_3O_5, and V_2O_3", Phys. Status Solidi A **48**, K153–K156 (1978).

[206] H. V. Keer, D. L. Dickerson, H. Kuwamoto, H. L. C. Barros, and J. M. Honig, "Heat Capacity of Pure and Doped V_2O_3 Single Crystals", J. Solid State Chem. **19**, 95–102 (1976).

[207] O. V. Lyakh, V. I. Surikov, V. I. Surikov, and N. A. Prokudina, "Magnetic susceptibility and heat capacity of V_2O_3 and $V_{1.973}Me_{0.020}O_3$ (Me = Fe, Cr, and Al)", Russ. Phys. J. **55**, 116–119 (2012).

[208] *MATLAB Release 2017a*, The MathWorks, Inc., Natick, Massachusetts, United States, 2017.